


Fall 12-20-2017

Three-dimensional Nanomaterials for Supercapacitor Applications: From Metal Oxides to Metal Phosphides

Zhi Zheng
University of New Orleans, zheng352@gmail.com

Follow this and additional works at: <https://scholarworks.uno.edu/td>

 Part of the [Materials Chemistry Commons](#), and the [Nanoscience and Nanotechnology Commons](#)

Recommended Citation

Zheng, Zhi, "Three-dimensional Nanomaterials for Supercapacitor Applications: From Metal Oxides to Metal Phosphides" (2017). *University of New Orleans Theses and Dissertations*. 2441.
<https://scholarworks.uno.edu/td/2441>

This Dissertation is protected by copyright and/or related rights. It has been brought to you by ScholarWorks@UNO with permission from the rights-holder(s). You are free to use this Dissertation in any way that is permitted by the copyright and related rights legislation that applies to your use. For other uses you need to obtain permission from the rights-holder(s) directly, unless additional rights are indicated by a Creative Commons license in the record and/or on the work itself.

This Dissertation has been accepted for inclusion in University of New Orleans Theses and Dissertations by an authorized administrator of ScholarWorks@UNO. For more information, please contact scholarworks@uno.edu.

Three-dimensional Nanomaterials for Supercapacitor Applications:
From Metal Oxides to Metal Phosphides

A Dissertation

Submitted to the Graduate Faculty of the
University of New Orleans
in partial fulfillment of the
requirements for the degree of

Doctor of Philosophy
in
Engineering and Applied Science
Physics

by

Zhi Zheng

M.S. University of Electronic Science and Technology of China, 2011
B.S. University of Electronic Science and Technology of China, 2008

December, 2017

Copyright 2017, Zhi Zheng

To my family.

Acknowledgments

I would first express my sincere gratitude to my advisor, Prof. Weilie Zhou, for his constant support, kind guidance, patient discussion and valuable suggestions in my research over the past 6 years.

I gratefully thank the academic committee members: Prof. Leszek Malkinski, Prof. Damon Smith, Prof. Ashok Puri, and Prof. John Wiley for their helpful suggestions on this dissertation.

I greatly appreciate the generous help from Prof. Tarr for allowing me to access his lab freely and use the electrochemical workstation. I gratefully thank Dr. Yumi H. Ikuhara and her group for their collaboration in TEM characterizations and valuable discussion. I would also thank Dr. Jiechao Jiang for the help of XPS measurements.

I thank Prof. C. Gregory Seab and Prof. Kevin Stokes for their kind help and valuable suggestions during my TA. I would like to thank AMRI and Physics office staff Poncho De Leon, Jennifer Tickle, and Denise Bauer Banks for their kind help.

I would like to extend my appreciation to all the members in Prof. Zhou's group: Dr. Jianjun Chen, Dr. Kai Wang, Dr. Haiqiao Su, Dr. Satish Rai, Dr. Sarah Wozny, Shuke Yan, Nooralldin Alkurd, Michael Retana, Ramona Luna, and Jingjin Luo. It's been quite a journey working with you. I also like to thank all my friends in AMRI, chemistry and physics, Dr. Rahmatollah Eskandari, Dr. Taha Rostamzadeh, Dr. Richie Prevost, Dr. Shankar Khanal, and Daniel Adams. I remember all those great memories and your help throughout these years.

I cannot thank my parents enough. You always support every decision I made, except my hair. To my wife, you are my best friend.

List of Figures

- Figure 1.1. Ragone plot comparison of various electrochemical energy storage systems. (© 2011 Materials Research Society, reprinted with permission.)¹³ 3
- Figure 1.2. The charge mechanisms of (a) carbon particles, (b) porous carbon, (c) redox pseudocapacitance, and (d) intercalation pseudocapacitance in capacitive energy storage. Cyclic voltammograms of (e) supercapacitor and (f) battery. Galvanostatic discharge behavior of (g) supercapacitor and (h) battery. (© 2014 American Association for the Advancement of Science, reprinted with permission.)¹⁹ 5
- Figure 1.3. The electrical double layer models and potential distributions at a positively charged surface: (a) the Helmholtz model, (b) the Gouy–Chapman model, and (c) the Stern model. (© 2009 Royal Society of Chemistry, reprinted with permission.)²⁷ 8
- Figure 1.4. Schematic of an EDLC consisting of Stern and diffuse layers between two planar electrodes. (© 2015 Laurent Pilon et al., reprinted under the terms of the Creative Commons Attribution Non-Commercial No Derivatives 4.0 License, CC BY-NC-ND.)²³ 10
- Figure 1.5. Schematic diagrams of (a) EWCC, (b) EDCC and (c) EDLC models, respectively. (© 2008 WILEY-VCH Verlag GmbH & Co. KGaA, Weinheim, reprinted with permission.)²⁹ 11
- Figure 1.6. Schematic illustrating (a) the concept of filled and empty carbon pores at 0 V, and (b) counter-ion adsorption, ion exchange, and co-ion desorption charging mechanisms. (© 2016 American Chemical Society, reprinted under the terms of the Creative Commons Attribution Non-Commercial No Derivatives 4.0 License, CC BY-NC-ND;³² © 2014 The Royal Society of Chemistry, reprinted with permission.³¹)..... 12
- Figure 1.7. Schematics of pseudocapacitance mechanisms: (a) underpotential deposition, (b) redox pseudocapacitance, and (c) intercalation pseudocapacitance. (© 2014 Royal Society of Chemistry, reprinted with permission.)³⁴ 14
- Figure 1.8. A typical CV curve of (a) an electroplated Co_3O_4 thin film, using different upper potential limits, in 1 M KOH electrolyte; (b) a MnO_2 electrode in 0.1 M K_2SO_4 , showing the successive multiple surface redox reactions leading to the pseudocapacitive behavior. (© 2015 Thierry Brousse et al., reprinted under the terms of the Creative Commons Attribution Non-Commercial No Derivatives 4.0 License, CC BY-NC-ND;⁴⁰ © 2008 Macmillan Publishers Limited, reprinted with permission.¹⁸)..... 16
- Figure 1.9. Schematic illustrations of the band model for chemical bonding (a) between metal atoms and (b) the corresponding energy levels of the valence electrons as a function of the degree

of delocalization of valence electrons in the cluster of metal atoms. (© 2016 George Z. Chen, reprinted under the terms of the Creative Commons Attribution Non-Commercial No Derivatives 4.0 License, CC BY-NC-ND.) ⁴⁵	18
Figure 1.10. The basic configuration of an ideal supercapacitor.	19
Figure 1.11. Comparison of the charge-discharge curves between supercapacitor and battery. (© 2008 American Institute of Physics, reprinted with permission.) ⁴⁶	20
Figure 1.12. Typical working potential windows of various pseudocapacitance electrode materials in aqueous electrolytes. (© 2017 Royal Society of Chemistry, reprinted with permission.) ⁵²	22
Figure 1.13. Schematic illustration of supercapacitor maximum charging voltage (MCV), potential of zero voltage (PZV), and electrode capacitive potential range (CPR). (© 2015 Nature Publishing Group, reprinted under the terms of the Creative Commons Attribution Non-Commercial No Derivatives 4.0 License, CC BY-NC-ND.) ⁵⁵	24
Figure 1.14. Typical voltage profiles and schematic device configurations of symmetric and hybrid supercapacitors. (© 2012 American Chemical Society, reprinted with permission.) ⁵⁸	26
Figure 1.15. (a) The concept, (b) charge mechanism, and (c) system architecture of the flow capacitor. (© 2012 WILEY-VCH Verlag GmbH & Co. KGaA, Weinheim, reprinted with permission.) ⁶⁰	27
Figure 1.16. Potential diagrams of fully charged and discharged states of (a) Type I, (b) Type II, (c) Type III and (d) Type IV CP-based supercapacitor. (© 2016 American Chemical Society, reprinted with permission.) ¹⁶⁰	38
Figure 2.1. (a) Top view and (b) cross-sectional FESEM images of TiO ₂ nanorod arrays on Ti foil. The inset in (a) is enlarged images of TiO ₂ nanorod tip. (c) XRD pattern, (d) XPS survey spectra and (e) Ti 2p XPS spectra of TiO ₂ nanorod arrays.	46
Figure 2.2. FESEM images of TiO ₂ nanorod arrays on Ti wire. (a) low-magnification, (b, c) high magnification from squares b and c in panel a.	47
Figure 2.3. (a) TEM image of an individual TiO ₂ nanorod. (b) and (c) are SADPs taken from [110] and [111] zone axis, respectively. (d) EDS spectra of an individual TiO ₂ nanorod. The Cu peak originates from the copper grid for TEM observation. (e) and (f) HRTEM image of a single TiO ₂ nanorod.	49
Figure 2.4. (a) STEM dark field image of Ti/TiO ₂ interface. (b) EDS spectra of each area in panel a. (c) and (d) are EDS elemental mappings corresponding to titanium (Ti) and oxygen (O), respectively.	50

Figure 2.5. (a) Cross-sectional TEM image of Ti/TiO ₂ interface. (b)–(d) Diffraction patterns taken from the circled areas b, c, and d in figure (a), respectively.....	51
Figure 2.6. The schematic formation process of TiO ₂ nanorod arrays on Ti foil.	52
Figure 2.7. (a) Cyclic voltammetry curves of the as-synthesized TiO ₂ nanorod arrays on Ti foil at different scan rates, (b) areal capacitance of the as-synthesized TiO ₂ nanorod arrays on Ti foil as a function of scan rate.....	54
Figure 2.8. CV curves of TiO ₂ nanorod arrays on Ti wire.	55
Figure 2.9. (a) Cyclic voltammetry curves of the TiO ₂ nanorod arrays at different scan rates. (b) Areal capacitance of TiO ₂ nanorod arrays as a function of scan rates. (c) Galvanostatic charge/discharge curves of TiO ₂ nanorod arrays at different current densities. (d) Cycle performance of TiO ₂ nanorod arrays measured by galvanostatic charge/discharge at a scan rate of 100 μA/cm ² for 1000 cycles. Insert is the typical charge-discharge curves within ten cycles.	56
Figure 2.10. (a) The Nyquist plot and (b) Mott–Schottky plot of TiO ₂ nanorod arrays. The inset in (a) shows the high-frequency part of the Nyquist plot.	57
Figure 2.11. (a) Optical micrograph of bended Ti foil with TiO ₂ nanorod arrays. (b) CV curves collected at 100 mV s ⁻¹ under different bending conditions. CV curves of the TiO ₂ nanorod arrays on Ti foil at different scan rates under (c) 45° and (d) 90° bending angles.....	58
Figure 3.1. (a) Schematics of the synthesis procedure of CoP nanowire arrays on carbon cloth, (b) photograph showing (from left to right) blank carbon cloth, Co(CO ₃) _{0.5} (OH)·0.11H ₂ O and CoP nanowire arrays on carbon cloth.	65
Figure 3.2. XRD patterns of Co(CO ₃) _{0.5} (OH)·0.11H ₂ O and CoP nanowire arrays.....	66
Figure 3.3. (a) Low- and (inset) high-magnification SEM images, (b) TEM image, (c) SAED pattern and (d) EDS spectrum of Co(CO ₃) _{0.5} (OH)·0.11H ₂ O nanowire.	67
Figure 3.4. (a) FESEM images of CoP nanowire arrays. (b) TEM image of a single CoP nanowire and the inset showing the HRTEM lattice image of the (111) plane. (c) Indexed SAED pattern of the CoP nanowire. (d) EDS spectrum of CoP nanowire. (e) HAADF-STEM and corresponding EDS elemental maps imaged by P, O, Co, and P + O. (f, g) HAADF-STEM image and corresponding EELS maps using the energy range of 6.0-7.0 eV for CoP nanowire, respectively. (h) EELS spectra from the CoP nanowire.....	69
Figure 3.5. (a) SEM image and (b) XRD patterns of cobalt oxide (Co ₃ O ₄) nanowire arrays.....	70

Figure 3.6. (a) CV curves of CoP, cobalt oxide, and blank carbon cloth after phosphidation at a scan rate of 100 mV/s. (b) CV curves of the CoP nanowire array electrode at different scan rates. (c) Galvanostatic charge/discharge curves of the CoP nanowire array electrode at different current densities. (d) Areal and specific capacitance of the CoP nanowire array electrode as a function of current density..... 72

Figure 3.7. (a) Cycle performance of the CoP nanowire array electrode in 1 M LiCl aqueous electrolyte at a scan rate of 5 mA/cm² for 5000 cycles. (b) Nyquist plots of the CoP electrode collected before and after the cycling test. The inset is the high-frequency part of the Nyquist plot. (c) The equivalent circuit of CoP nanowire arrays electrode. (d) Plots of the equivalent series resistance R_s and the charge transfer resistance R_{CT} as a function of cycle number..... 74

Figure 3.8. (a) SEM image of CoP nanowire arrays electrode after 5000 charge/discharge cycles at a scan rate of 5 mA/cm². Insert shows the tips of nanowires. (b) XPS survey of CoP nanowire arrays. High-resolution core level of (c) Co 2p and (d) P 2p XPS spectra of the CoP nanowire arrays before and after the cycling test. 76

Figure 3.9. (a) Schematics the designed symmetric and asymmetric supercapacitors. (b) CV curves of the SSC at different scan rates. (c) Galvanostatic charge/discharge curves of the SSC at different current densities. (d) Areal and volumetric capacitance of the SSC as a function of current density. (e) Cycle performance of the SSC at a scan rate of 5 mA/cm² for 5000 cycles. 78

Figure 3.10. (a) Low and (b) high magnification SEM image of MnO₂ nanowire arrays. (c) TEM image of MnO₂ nanowire. (d) High-resolution TEM image of MnO₂ nanowire. (e) EDS spectra of MnO₂ nanowire. (f) XRD spectrum of MnO₂ nanowire arrays. 80

Figure 3.11. (a) CV curves of the MnO₂ electrode at different scan rates. (b) Galvanostatic charge/discharge curves of MnO₂ electrode at different current densities. (c) Areal capacitance of CoP and MnO₂ electrode as a function of current density. (d) CV curves of CoP and MnO₂ electrodes at 100 mV/s..... 81

Figure 3.12. (a) CV curves of the ASC device collected in different scan voltage windows. (b) CV curves obtained at a scan rate of 100 mV/s under normal, bent, and twisted conditions. Insert are the photographs of the ASC device. (c) Galvanostatic charge/discharge curves of the ASC at different current densities. (d) Areal and volumetric capacitance of the ASC as a function of current density. (e) Cycle performance of the ASC at a scan rate of 5 mA/cm² for 5000 cycles. (f) Ragone plots of the ASC and SSC devices..... 83

Figure 3.13. (a) Photograph (from left to right) of blank carbon cloth, Co(OH)₂ and CoP nanosheet arrays on carbon cloth. (b) XRD patterns of Co(OH)₂ and CoP nanosheet arrays on carbon cloth. Low- and (inset) high-magnification SEM images of (c) Co(OH)₂ nanosheet arrays and (d) CoP nanosheet arrays on carbon cloth..... 87

Figure 3.14. (a) TEM images, (b) Selected area electron diffraction patterns and (c) EDS spectra of and Co(OH) ₂ nanosheet.	88
Figure 3.15. (a) TEM image, (b) selected area electron diffraction patterns, (c) EDS spectra, (d) HRTEM image, (e) HAADF-STEM and corresponding EDS elemental mapping images of P, O, Co and P+O, (f) dark field image and (g) EELS mapping on energy range 6.0-7.0 eV of CoP nanosheet.....	89
Figure 3.16. (a) CV curves of the CoP nanosheet arrays electrode at different scan rates. (b) Galvanostatic charge/discharge curves of CoP nanosheet arrays electrode at different current densities. (c) Areal capacitance of CoP nanosheet arrays electrodes as a function of current density. (f) Nyquist plots of CoP nanosheet arrays electrodes.	90
Figure 3.17. (a) CV curves of the CoPS and CoP electrodes at 100 mV/s. b) Areal capacitances of the CoPS and CoP electrodes as-as a function of scan rate.	91
Figure 3.18. CV curves of CoP nanosheet electrode under different sulfidation temperature. (a) 200°C, (b) 250°C, (c) 300°C, and (d) 350°C.....	92
Figure 4.1. (a) FESEM image and (b) XRD patterns of FeOOH nanorod arrays.....	98
Figure 4.2. FESEM images of (a) FeP and (b) FeP/PEDOT nanorod arrays. The insets are the high magnification FESEM images. (c) XRD patterns and (d) Raman spectra of FeP and FeP/PEDOT nanorod arrays.....	99
Figure 4.3. The chemical structures of (a) EDOT, and (b) PEDOT, respectively.....	100
Figure 4.4. (a) TEM image, (b) SAED, and (c) HRTEM of FeP nanorod, (d) HAADF-STEM and corresponding EDS elemental mapping images of P, Fe and O, respectively.....	101
Figure 4.5. (a) TEM image, (b) SAED, and (c) HRTEM of FeP/PEDOT nanorod, (d,e) EELS spectrum and (f) EDS spectrum of FeP/PEDOT nanorods, (g) HAADF-STEM and corresponding EDS elemental mapping images of P, Fe, O, C and S, respectively.....	102
Figure 4.6. (a) CV curves of FeP electrode collected at scan rates from 10 to 100 mV/s. (b) Galvanostatic charge/discharge curves of FeP electrode at current densities from 1 to 10 mA/cm ²	103
Figure 4.7. (a) CV curves of FeP and FeP/PEDOT electrodes at the scan rate of 100 mV/s. (b) CV curves of FeP/PEDOT electrode collected at scan rates from 10 to 100 mV/s. (c) Galvanostatic charge/discharge curves of FeP/PEDOT electrode at current densities from 1 to 10 mA/cm ² . (d) Comparison of the areal capacitance at different current densities of FeP and FeP/PEDOT	

electrodes. (e) Nyquist plots of FeP and FeP/PEDOT electrodes. The inset is the high-frequency part of the Nyquist plot. (f) Cycle stability of FeP and FeP/PEDOT electrodes. 105

Figure 4.8. FESEM images of (a) FeP and (b) FeP/PEDOT nanorod arrays after cycling test.. 106

Figure 4.9. (a) FESEM image and (b) XRD patterns of MnO₂ electrode..... 106

Figure 4.10. (a) CV curves of the MnO₂ electrode collected at scan rates from 10 to 100 mV/s. (b) Galvanostatic charge/discharge curves of the MnO₂ electrode at current densities from 1 to 10 mA/cm². 107

Figure 4.11. (a) CV curves of MnO₂ and FeP/PEDOT electrodes at the scan rate of 100 mV/s. (b) CV curves of the asymmetric device collected at scan rates from 10 to 100 mV/s. (c) Galvanostatic charge/discharge curves of the asymmetric device at current densities from 1 to 10 mA/cm². (d) Areal and volumetric capacitance of the asymmetric device at different current densities. (e) Cycle stability of the asymmetric device. (f) Ragone plots of the asymmetric device. 108

List of Table

Table 3.1. Comparison of capacitive performances of reported negative electrode materials and their corresponding ASCs.....	85
---	----

Table of Contents

List of Figures.....	v
List of Table.....	xi
Abstract.....	xiv
Chapter 1 Introduction.....	1
1.1. Energy Storage Systems.....	1
1.2. Working Mechanisms	3
1.2.1. Electrical Double Layer Capacitors	5
1.2.2. Pseudocapacitors.....	13
1.3. Supercapacitor Configuration	18
1.4. Electrode Materials	28
1.4.1. Carbon Materials.....	28
1.4.2. Transition Metal Oxides	30
1.4.3. Transition Metal Sulfides, Nitrides and Phosphides.....	34
1.4.4. Conducting Polymers.....	35
1.4.5. The Role of Nanomaterials in Supercapacitor Electrodes	39
1.5. Overview of this Dissertation.....	40
Chapter 2 TiO ₂ Nanorod Arrays on Ti Substrate for Supercapacitor Application.....	42
2.1. Introduction	42
2.2. Experiments.....	43
2.2.1. Synthesis of TiO ₂ nanorod arrays	43
2.2.2. Material Characterizations	43
2.2.3. Electrochemical Measurements	44
2.3. Results and Discussion.....	44
2.3.1. Growth Mechanism.....	44
2.3.2. Electrochemical Performance	53
2.4. Conclusion.....	59
Chapter 3 Nanostructured Cobalt Phosphide as Negative Electrode for Flexible Solid-State Asymmetric Supercapacitors	60
3.1. Introduction	60

3.2. CoP Nanowire Arrays	61
3.2.1. Experiments	61
3.2.2. Results and Discussion	64
3.3. CoP Nanosheet Arrays	85
3.3.1. Experiments	85
3.3.2. Results and Discussion	86
3.4. Conclusion.....	92
Chapter 4 PEDOT Coated Iron Phosphide Nanorod Arrays as High-Performance Supercapacitor Negative Electrodes	94
4.1. Introduction	94
4.2. Experiments.....	95
4.2.1. Synthesis of FeP nanorod arrays.....	95
4.2.2. Synthesis of FeP/PEDOT nanorod arrays.....	96
4.2.3. Preparation of MnO ₂ electrode	96
4.2.4. Fabrication of the ASC	96
4.2.5. Material Characterizations	96
4.2.6. Electrochemical Measurements	97
4.3. Results and Discussion.....	97
4.4. Conclusion.....	109
Chapter 5 Conclusion and Perspective	110
Reference	112
Appendix: Copyright Permissions	144
VITA.....	157

Abstract

Over the past few years, energy storage devices have received tremendous interest due to the increasing demand for sustainable and renewable energy in modern society. Supercapacitors are considered as one of the most promising energy storage devices because of their high power density and long cycle life. However, low energy density remains as the main shortcoming for supercapacitors. The overall performance of supercapacitors is predominantly determined by the characteristics of the electrodes. Specifically, constructing nanostructured electrode material has been proven as an efficient way to improve the performance by providing large surface area and short ionic and electronic diffusion paths. Another approach to improve the performance of supercapacitors is the rational design of the asymmetric supercapacitor (ASC), which can extend the operation voltage. In this regard, we have focused on the synthesis and utilization of several nanomaterials, in particular, pseudocapacitance materials such as metal oxides and metal phosphides, on both positive and negative electrodes, as well as the ASC design and fabrication. First, three-dimensional TiO₂ nanorod arrays have been synthesized on Ti substrate by a facile one-step hydrothermal method and demonstrated as an ideal supercapacitor positive electrode, which exhibited good areal capacitance and excellent cycling stability. Owing to the novel “dissolve and grow” mechanism, this method provides a simple and low-cost technique for flexible supercapacitor application. Second, using cobalt phosphide and iron phosphide as examples, we have demonstrated metal phosphides as high-performance supercapacitor negative electrodes for the first time. Cobalt phosphide nanowire arrays have been synthesized and presented a high capacitance of 571.3 mF/cm². To improve the cycling stability, gel electrolyte was used to suppress the irreversible electrochemical reaction. The flexible solid-state asymmetric MnO₂//CoP supercapacitor exhibited good electrochemical performance, such as a high energy density of 0.69

mWh/cm³ and a high power density of 114.2 mW/cm³. Furthermore, a PEDOT coating has been adapted to further enhance the cycling stability as well as capacitance performance of FeP nanorod arrays. The FeP/PEDOT electrode represents an outstanding capacitance of 790.59 mF/cm² and a good stability of 82.12% retention after 5000 cycles. In addition, a MnO₂//FeP/PEDOT ASC was fabricated with an excellent volumetric capacitance of 4.53 F/cm³ and an energy density of 1.61 mWh/cm³.

Keywords: Supercapacitors, Three-dimensional, Nanostructures, Metal Oxides, Metal Phosphides

Chapter 1 Introduction

1.1. Energy Storage Systems

The energy issue has become one of the most important problems facing the world. In 2015, 13147.3 million tonnes oil equivalent (Mtoe) of energy have been consumed in the entire world, which means approximately 17.45 terawatt (TW) power is needed to run the world and is predicted to double by the middle of the century and triple by the end of the century.^{1,2} The fossil fuels, such as oil, natural gas, and coal are and would remain the largest energy source in the foreseeable future.³ In consequence, production, transport, and combustion of fossil fuels lead to the emission of greenhouse gas, which is the primary reason for the global environmental change.⁴ According to NASA's Goddard Institute for Space Studies (GISS), the average global temperature has increased by about 0.8 °C since 1880, in which two-thirds of the warming was occurred after 1975.⁵ At the same time, as finite and rapidly depleting resources, fossil fuels were forecast to be depleted in the near future. Even the optimistic estimations predict the oil production decline will happen before 2030.^{6,7} Therefore, increasing concerns about climate change and the depletion of fossil fuels lead to the expanded use of renewable energy, such as solar, wind, and hydropower. However, a new challenge arises with the remarkable increase in renewable energy usage. Due to the intermittence and geographic distribution nature of renewable energy, more reliable energy storage systems are highly desired.⁸ In addition, the ever-increasing demand for energy storage in portable electronic devices and clean transportation also requires the progress of energy storage system.⁹

Energy exists in many different forms and, therefore, an enormous variety of energy storage systems is available. In general, energy storage systems can be divided into different classes by the form of storage: electrical (such as Superconducting Magnetic Energy Storage),

mechanical (Compressed Air Energy Storage, Pumped Hydroelectric Storage, and Flywheel Energy Storage), electrochemical (supercapacitor, battery, and fuel cell), and thermal (such as phase change materials).^{10,11} Electrochemical energy storage systems are considered as the most promising technology to meet the pressing need for energy storage because of their numerous advantages, such as pollution-free operation, high round-trip efficiency, flexible power and energy characteristics, long cycle life, and low maintenance.¹²⁻¹⁴

Electrochemical energy storage systems can be distinguished by the energy storage and conversion mechanisms. Batteries, fuel cells, and supercapacitors are the most studied electrochemical energy storage systems. Fuel cells are different from batteries and supercapacitors based on the locations of energy storage and conversion. In batteries and supercapacitors, the charge transfer occurs within the electrode, which makes it a closed system. Fuel cells are open systems which the active materials undergoing the redox reaction are delivered externally. Supercapacitors have the similar configuration, yet different energy storage mechanism to batteries. Supercapacitors store energy via a capacitive process arising from an electrochemical double layer or pseudocapacitance at the electrode-electrolyte interface.¹⁵

The terms specific energy (in Wh/kg) and energy density (Wh/L) are used to compare the energy contents of a system, whereas the capability is expressed as specific power (in W/kg) and power density (in W/L). A Ragone plot which contrasts the specific energy and specific power of various electrochemical energy storage systems is shown in Figure 1.1.¹³ Unlike batteries and fuel cells, which can store a large amount of energy but offer low power, supercapacitors give much higher power density. Owing to other characteristics besides high power, such as short charge/discharge time, and excellent cycle stability, supercapacitors have attracted great interest in the last decades and emerged as one of the prime important energy storage systems.¹⁶⁻¹⁸

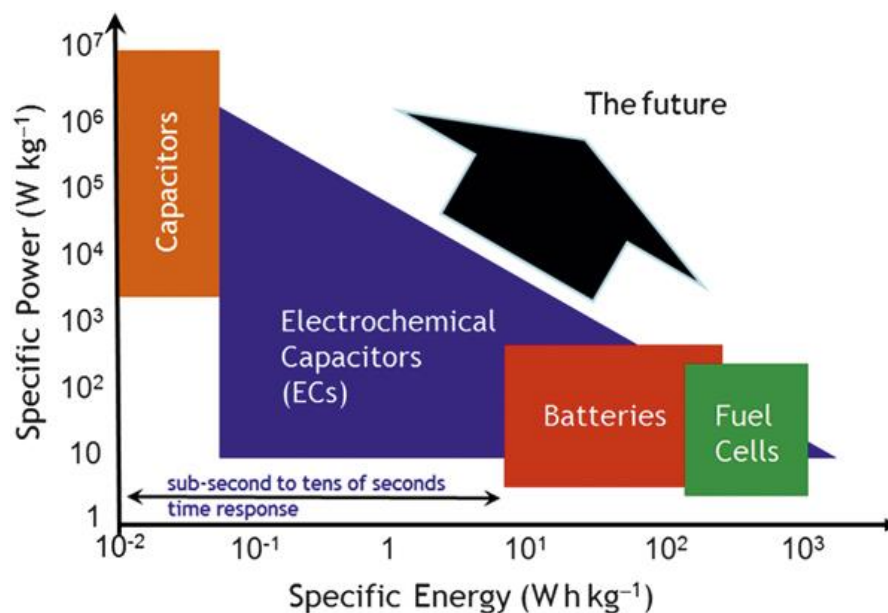


Figure 1.1. Ragone plot comparison of various electrochemical energy storage systems. (© 2011 Materials Research Society, reprinted with permission.)¹³

1.2. Working Mechanisms

The difference between batteries and supercapacitors in terms of the energy and power density relies on the different charging mechanism, even though they are both based on electrochemical process. Li-ion batteries are one of the most important batteries, in which the charge is stored by the slow diffusion-controlled insertion of Li^+ in the bulk electrode material. On the other hand, supercapacitors store charge by adsorption of electrolyte ions or fast redox reactions onto the surface of electrode materials (Figure 1.2a-d).¹⁹ Since the charging process is confined to the surface, supercapacitors can respond to changes faster than batteries, which leads to higher power and fast charge/discharge. However, the surface confinement of energy charge also results in a lower energy of supercapacitor.

The different charge mechanisms of supercapacitors and batteries can be well distinguished by the electrochemical measurements (Figure 1.2e-h).¹⁹ Supercapacitors exhibit classic rectangular cyclic voltammograms (Figure 1.2e) and a linear time-dependent discharge curve (Figure 1.2g). In contrast, redox peaks corresponding to oxidation and reduction indicative the phase transitions of batteries (Figure 1.2f). The presence of two phases in batteries is also indicated by the voltage plateau in the galvanostatic measurement (Figure 1.2h). Interestingly, some battery-type materials exhibit capacitor-like properties when reaching to the nanometer scale. For example, as shown in Figure 1.2h, bulk LiCoO_2 shows typical battery behavior with a voltage plateau. However, the discharge curve transfer into linear once it reaches smaller scale (6 nm).²⁰ This type of materials is nominated as extrinsic pseudocapacitance materials, in contrast to intrinsic pseudocapacitance materials, such as MnO_2 , which display the characteristics of capacitive charge storage despite the sizes and morphologies, as shown in Figure 1.2g.^{21,22}

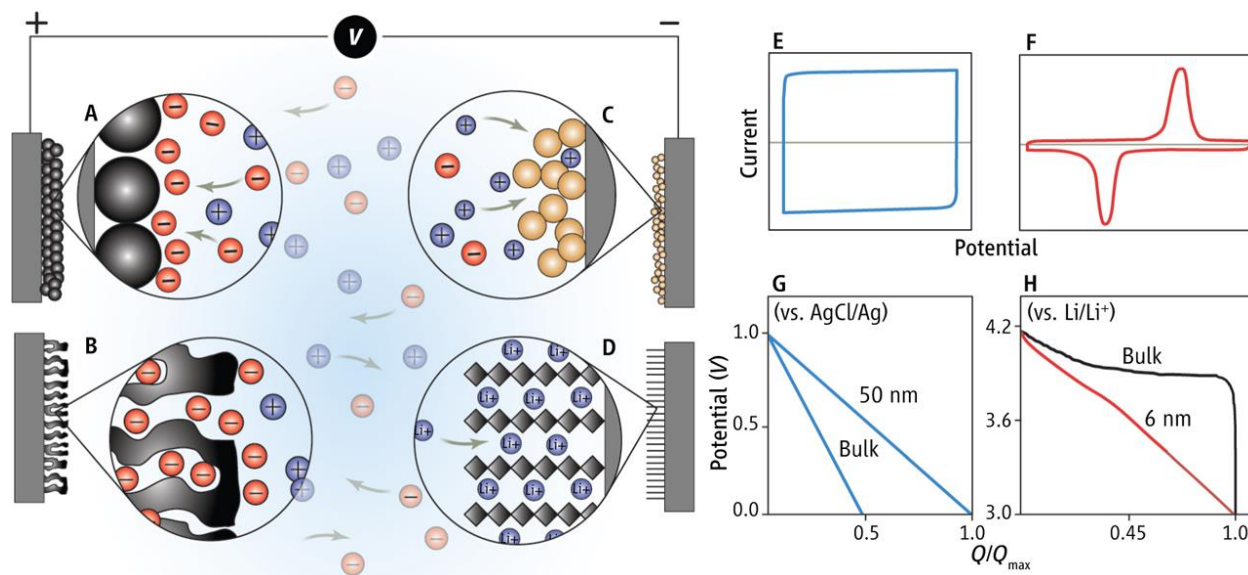


Figure 1.2. The charge mechanisms of (a) carbon particles, (b) porous carbon, (c) redox pseudocapacitance, and (d) intercalation pseudocapacitance in capacitive energy storage. Cyclic voltammograms of (e) supercapacitor and (f) battery. Galvanostatic discharge behavior of (g) supercapacitor and (h) battery. (© 2014 American Association for the Advancement of Science, reprinted with permission.)¹⁹

Based on the charging mechanism, supercapacitors can be classified into two categories in general: electrical double layer capacitors (EDLCs) and pseudocapacitors.

1.2.1. Electrical Double Layer Capacitors

EDLCs use carbon-based active materials as electrodes. As the name implies, for EDLCs, the charge is stored in the electric double layer at the electrode/electrolyte interfaces (Figure 1.3). As described in 1895 by Hermann von Helmholtz, the ions with electric charges in the electrolyte accumulate on the surface of the electrode with opposite charge.²³ The layers of the charged ions in the electrolyte and counter electronic charge at the electrode surface thus form the so-called

double layer (Figure 1.3a). The double layer structure is analogous to that of conventional dielectric planar capacitors separated by a small distance d , approximated as the radius of an ion. Thus, the capacitance of EDLC can be written as²⁴

$$C = \frac{\varepsilon_r \varepsilon_0 A}{d} \quad (1.1)$$

where ε_r is the electrolyte relative permittivity, ε_0 is the vacuum permittivity, A is the electrode surface area, d is the distance between the double layer. As a result, the EDLCs present much higher capacitance than conventional capacitors due to the extremely thin double layer distance (nanometer size) and large surface area.

The Helmholtz model was later modified by Gouy and Chapman²⁵ with the consideration of a continuous Boltzmann distribution of ions in the electrolyte solution. As shown in Figure 1.3b, a so-called “diffuse layer” form near the interface of electrode and electrolyte giving by the fact that the ions are mobile in the electrolyte solution under the combined effects of thermal diffusion and electromigration. However, the Gouy-Chapman model treats ions as point-charges which results in an impractical large ion concentration at the electrode surfaces, thus leads to an overestimation of the double layer capacitance. To solve this problem, Stern combined the Helmholtz model and the Gouy-Chapman model, which the finite size of ions was considered. Two regions of ion distribution were explicitly distinguished in Stern model: the inner Stern layer and the outer diffuse layer, as shown in Figure 1.3c. In the diffuse layer, ions are distributed as Gouy-Chapman model described. Inside the Stern layer, specifically (covalent) adsorbed ions and non-specifically adsorbed counterions accumulate at the different distance from the charged surface, thus forming the inner Helmholtz plane (IHP) and the outer Helmholtz plane (OHP), respectively.²⁶ Another important aspect in EDLC is the potential distribution in the

electrode/electrolyte interface. Because of the close packing of ions, for the positive electrode, the potential distributions decrease linearly in the Stern layer and reach a plateau in the diffuse layer. For ideal binary and symmetric electrolytes consist of two ion species, the electric potential is governed by the Bikerman's model,²³

$$\nabla \cdot (\varepsilon_0 \varepsilon_r \nabla \Psi) = \begin{cases} 0 & \text{in the Stern layer} \\ \frac{2zeN_A c_\infty \sinh\left(\frac{ze\Psi}{k_B T}\right)}{1 + 4N_A a^3 c_\infty \sinh^2\left(\frac{ze\Psi}{2k_B T}\right)} & \text{in the diffuse layer} \end{cases} \quad (1.2)$$

where ε_0 and ε_r are the free and relative permittivity, respectively, k_B is the Boltzmann constant, e is the elementary charge, N_A is the Avogadro number and T is the temperature. The local ion concentration is expressed as,

$$C(r) = \frac{C_\infty \exp\left(\frac{-ze\Psi(r)}{k_B T}\right)}{1 + 4B_A a^3 C_\infty \sinh^2\left(\frac{ze\Psi(r)}{2k_B T}\right)} \quad (1.3)$$

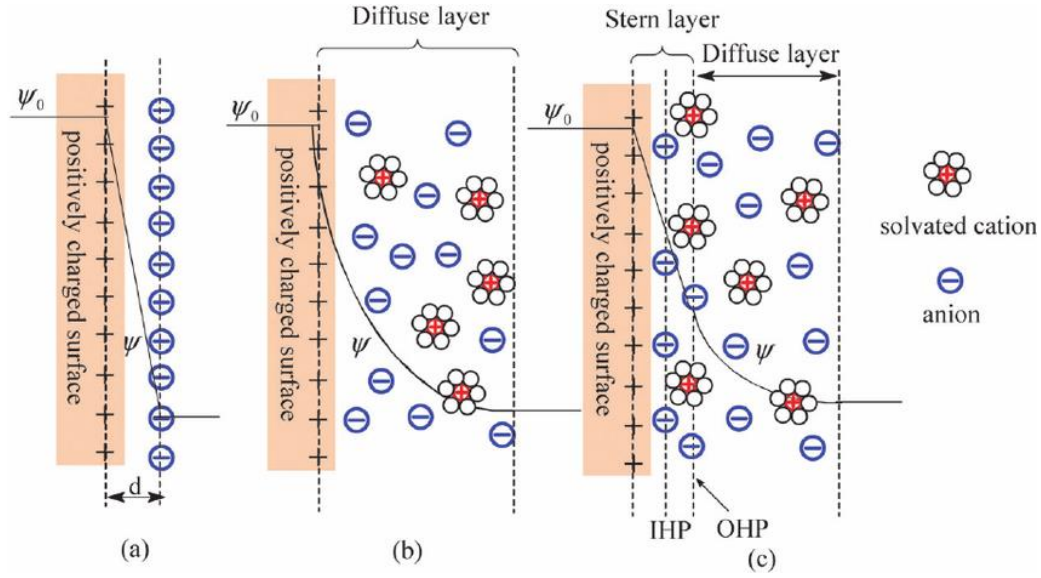


Figure 1.3. The electrical double layer models and potential distributions at a positively charged surface: (a) the Helmholtz model, (b) the Gouy–Chapman model, and (c) the Stern model. (© 2009 Royal Society of Chemistry, reprinted with permission.)²⁷

Based on the Stern model, in fact, there are two series double layers near the interface of electrode and electrolyte, one is formed in the Stern layer (C_{ST}) and the other is in the diffuse layer (C_D). Therefore, the overall double layer capacitance C_{DL} can be written as²³

$$\frac{1}{C_{DL}} = \frac{1}{C_{ST}} + \frac{1}{C_D} \quad (1.4)$$

which C_{ST} is given by Eqn. 1.1. and C_D can be calculated by²⁸

$$C_D = \frac{4zeN_A c_\infty \lambda_D}{\psi_D} \sinh\left(\frac{ze\psi_D}{2k_B T}\right) \quad (1.5)$$

where z is the valency of the electrolyte, e is the elemental charge, N_A is the Avogadro's number, c_∞ is the molar concentration of the electrolyte in the bulk, ψ_D is the electric potential, T is the absolute temperature, k_B is the Boltzmann constant, and λ_D is the Debye length,

$$\lambda_D = \frac{\sqrt{\varepsilon_r \varepsilon_0 k_B T}}{\sqrt{2z^2 e^2 N_A c_\infty}} \quad (1.6)$$

An EDLC device with electrodes A and B, as shown in Figure 1.4, can be treated as two capacitors in series with integral capacitances C_A and C_B . The total integral capacitance C_A of the device is given by²³

$$\frac{1}{C_T} = \frac{1}{C_A} + \frac{1}{C_B} \quad (1.7)$$

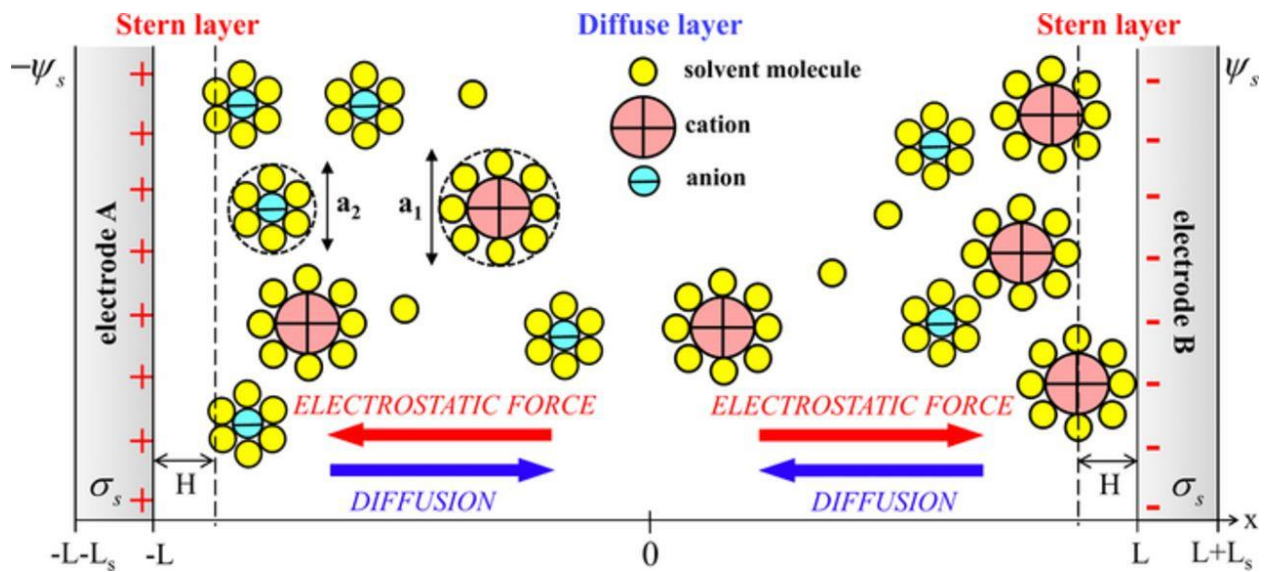


Figure 1.4. Schematic of an EDLC consisting of Stern and diffuse layers between two planar electrodes. (© 2015 Laurent Pilon et al., reprinted under the terms of the Creative Commons Attribution Non-Commercial No Derivatives 4.0 License, CC BY-NC-ND.)²³

However, those planar capacitor models are insufficient for justifying the electrochemical properties of porous materials, especially when the pore size reaches to micropore range (smaller than 2 nm), which was previously presumed that do not contribute to energy storage since its size are smaller than that of electrolyte ions. To solve this, Huang *et al.*²⁹ have established a general model which takes pore size into account. For mesopores (2-50 nm), counterions enter the pores and accumulate on the pore wall to form an electric double-cylinder capacitor (EDCC, Figure 1.5b) and the capacitance is given by²⁹

$$C = \frac{2\pi\epsilon_r\epsilon_0L}{\ln(b/a)} \quad (1.8)$$

$$C/A = \frac{\epsilon_r\epsilon_0}{b\ln(b/(b-d))} \quad (1.9)$$

where L , a , b and d are the pore length, inner radii, outer radii of cylinders, and the distance of approach of the ion to the pore wall, respectively. For micropores (<1 nm), the pore size is too small for a double cylinder model, thus an electric wire in cylinder model of a capacitor is formed (EWCC, Figure 1.5a), and Eqn. 1.5 becomes²⁹

$$C/A = \frac{\epsilon_r\epsilon_0}{b\ln(b/a_0)} \quad (1.10)$$

where a_0 is the effective size of the desolvated ion. In this case, the solvation shell was partial or

complete removed therefore the ions can enter the cylindrical pore. For macropores (>50 nm), the model is reduced to the traditional parallel-plate capacitor model in Eqn. 1.1 (Figure 1.5c).

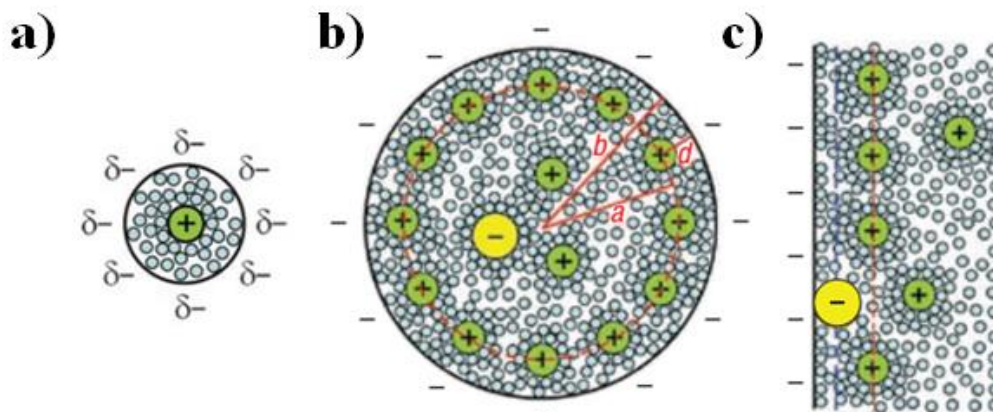


Figure 1.5. Schematic diagrams of (a) EWCC, (b) EDCC and (c) EDLC models, respectively. (© 2008 WILEY-VCH Verlag GmbH & Co. KGaA, Weinheim, reprinted with permission.)²⁹

Nevertheless, the “real” charge process is still more complicated than those classic models. Because nanoporous carbons generally consist of defective nanoscale graphitic units, they lack any long-range order. Such disordered natural leaves all the quantities ill-defined for the interface. Therefore, more works have been devoted to the fundamental understanding of the charge mechanism at the nano- and subnanoscale, both experimentally and theoretically. In order to fully understand the charging process, several aspects must be taken into account.³⁰ First, more accurate and realistic structure models of the porous electrode materials are the key to reveal the charge mechanism. Secondly, it is essential to disclose the electro-electrolyte interface in the absence of an applied potential. As shown in Figure 1.6a, it is long believed that the ions can only fill the pores under potential applied, however, recent researches show that the pores are filled with both ions and counter-ions even under zero potential. Upon applying potential, the overall excess of

counter-ions inside the pores can be described by several processes (Figure 1.6b): counter-ions adsorption, only the counter-ions are adsorbed into the pores; ion exchange, the adsorption of counter-ions and the desorption of co-ions happens simultaneously; co-ion desorption, only the co-ions originally in the pores are being desorbed.³¹

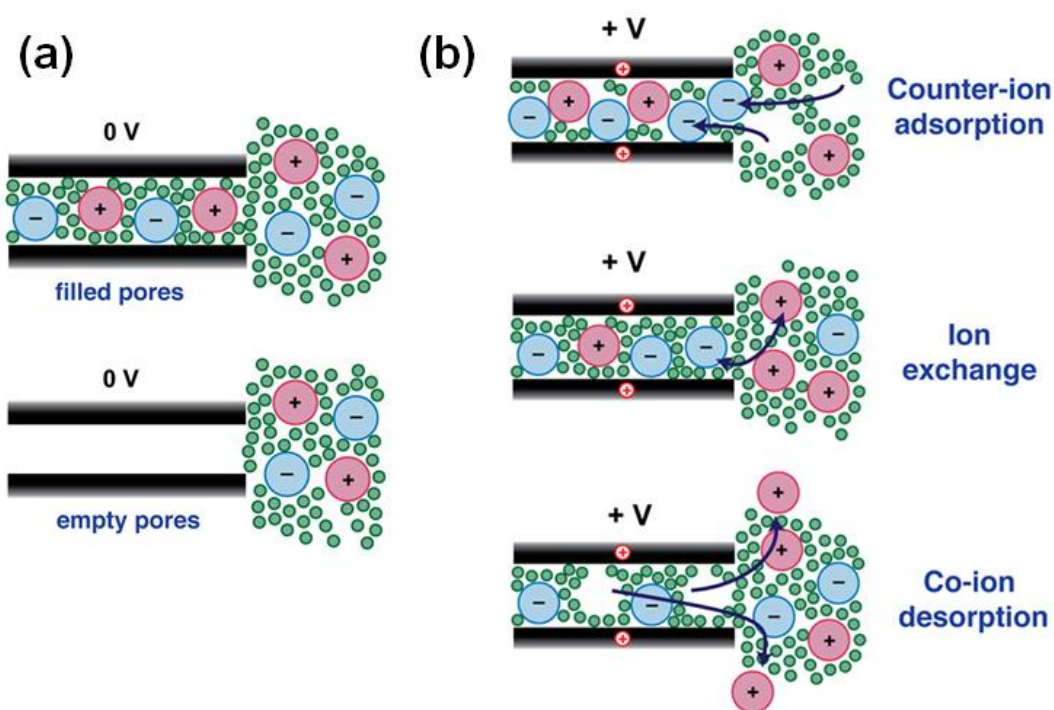


Figure 1.6. Schematic illustrating (a) the concept of filled and empty carbon pores at 0 V, and (b) counter-ion adsorption, ion exchange, and co-ion desorption charging mechanisms. (© 2016 American Chemical Society, reprinted under the terms of the Creative Commons Attribution Non-Commercial No Derivatives 4.0 License, CC BY-NC-ND;³² © 2014 The Royal Society of Chemistry, reprinted with permission.³¹)

1.2.2. Pseudocapacitors

In contrast with EDLCs, for pseudocapacitors, the charge is stored by the fast and reversible redox process at the surface of electrode material.³³ Therefore, they exhibit superior capacitance than EDLC. The most commonly used electrode materials for pseudocapacitors are transition metal oxides and conducting polymers. As shown in Figure 1.7,³⁴ the pseudocapacitance results from three different faradaic mechanisms: (1) underpotential deposition, (2) redox pseudocapacitance, and (3) intercalation pseudocapacitance. During underpotential deposition, metal cations in the electrolyte are reduced and deposited on a monolayer metal at the electrode surface (usually a noble metal) at a potential less negative than the equilibrium potential. The origin of underpotential deposition lies in the enhanced interaction of depositing metals (M) with foreign substrates (S)³⁵



The underpotential deposition process is highly reversible, however, the potential window is too small for applications. The redox pseudocapacitance realized by the faradaic charge-transfer between electrode and the ions in the electrolyte which are electrochemically adsorbed on or near the interface of electrode and electrolyte³⁵



The last type of pseudocapacitance, intercalation pseudocapacitance, is given rise by the intercalation of ions in the electrolyte into the layer or tunnels of electrode materials without obvious crystallographic phase change. The general reaction of intercalation can be written as³⁶



where MO is a layered transition metal oxide and A^+ is a cation.

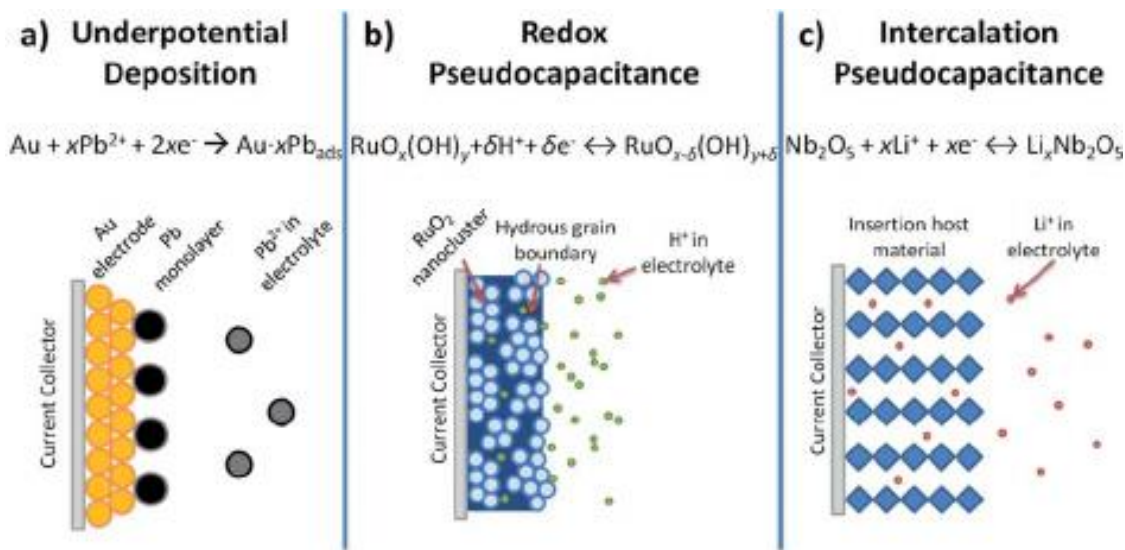


Figure 1.7. Schematics of pseudocapacitance mechanisms: (a) underpotential deposition, (b) redox pseudocapacitance, and (c) intercalation pseudocapacitance. (© 2014 Royal Society of Chemistry, reprinted with permission.)³⁴

Those three types of pseudocapacitance are based on different physics process and with different types of materials, in the thermodynamic point of view, however, they all follow the Langmuir-type isotherm:³⁷

$$\frac{y}{1-y} = K \exp\left(\frac{EF}{RT}\right) \quad (1.14)$$

where the quantity y can be fractional coverage θ of an electrode surface (underpotential deposition); conversion R of an oxidized species to a reduced species (or vice versa) in a redox system in solution (redox pseudocapacitance); or fractional absorption X into some intercalation

host (intercalation pseudocapacitance). E is the potential, F is the Faraday constant, R is the ideal gas constant, T is the temperature.

Therefore, the capacitance can be derived from Eqn. 1.12 as³⁷

$$C = q \left(\frac{dy}{dE} \right) = \frac{qF}{RT} \frac{K \exp\left(\frac{EF}{RT}\right)}{1 + K \exp\left(\frac{EF}{RT}\right)} \quad (1.15)$$

where q is the faradic charge required for adsorption/desorption of ions. The value of capacitance C is not entirely linear, so it is termed pseudocapacitance.

In an electrothermal point of view, the current response is different depending on whether the redox reaction is diffusion-controlled or surface-controlled. In the cyclic voltammetry (CV) measurement, the current response at a given potential to an applied voltage scan rate (mV/s) can be written as³⁸

$$i = k_1 v^{1/2} + k_2 v \quad (1.16)$$

where v is the scan rate. The current response varies with $v^{1/2}$ or v for the diffusion-controlled and surface-controlled process, respectively. As a result, the capacity follows the equation³⁹

$$Q = Q_{v=\infty} + \text{constant}(v^{-1/2}) \quad (1.17)$$

which means that the capacity contribution from the surface-controlled process ($Q_{v=\infty}$) is constant, while the capacity contribution from diffusion-controlled process varies with $v^{-1/2}$.

Careful attention must be paid in distinguishing pseudocapacitors and batteries since they both perform redox reaction during charge/discharge process. The term pseudocapacitance was originally used to describe the electrochemical behaviors of certain metal oxides (RuO₂, MnO₂, et

al.). Such metal oxide materials exhibit similar characteristics as capacitors, namely rectangle-shaped CV curves and triangular-shaped charge-discharge curves. However, some literatures presented other types of material, mostly nickel oxide/hydroxide and cobalt oxide/hydroxide, as pseudocapacitive materials. As shown in Figure 1.8a,⁴⁰ the CV curve of Co_3O_4 show a strong redox pair around 0.5 V vs. Hg/HgO, which is similar to that of batteries. As a result, the capacitance calculated in the different potential range is not constant. Therefore, such materials should be considered as battery-type rather than pseudocapacitance electrode, and the term capacity is more appropriate in describing their performance. On the contrast, MnO_2 show a CV curve of quasi-rectangular shape (Figure 1.8b). Yet, the reason why redox reactions in pseudocapacitors and batteries display such diverse signatures is still unclear. A commonly accepted explanation is that the overlapping of a serious redox peaks forms the overall quasi-rectangular shape, as shown in Figure 1.8b.^{18,41} However, a detailed theoretical study based on Nernst law reveals that redox process should always shows peak-shaped responses, despite broadening in varying extent.⁴²

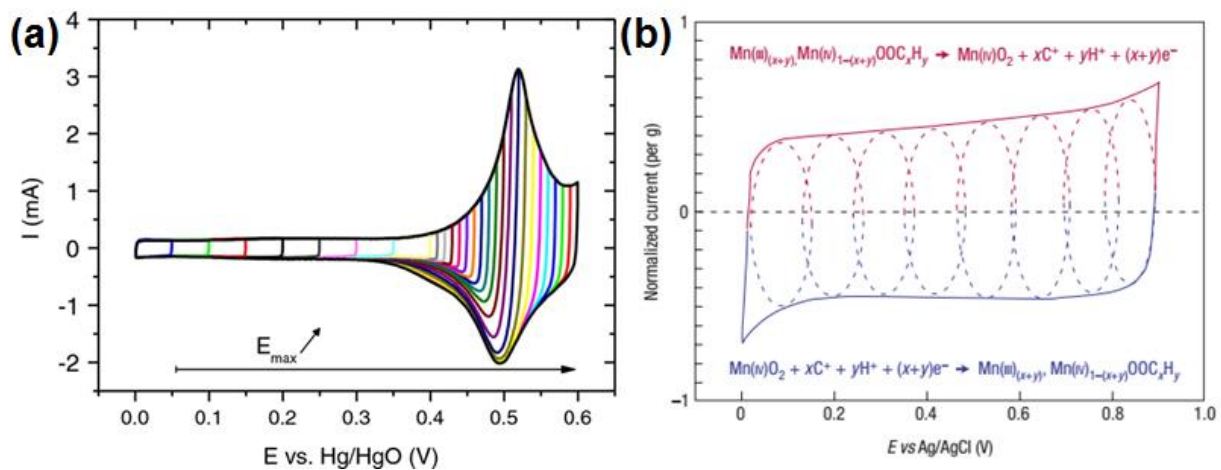


Figure 1.8. A typical CV curve of (a) an electroplated Co_3O_4 thin film, using different upper potential limits, in 1 M KOH electrolyte; (b) a MnO_2 electrode in 0.1 M K_2SO_4 , showing the successive multiple surface redox reactions leading to the pseudocapacitive behavior. (© 2015

Thierry Brousse et al., reprinted under the terms of the Creative Commons Attribution Non-Commercial No Derivatives 4.0 License, CC BY-NC-ND;⁴⁰ © 2008 Macmillan Publishers Limited, reprinted with permission.¹⁸⁾

Though double layer capacitance and pseudocapacitance are two different physics processes, they always coexist in a supercapacitor system. For example, depending on different preparation or pretreatment methods of carbon material, the surface or edge functional groups usually give rise to the pseudocapacitance contribution.⁴³ On the other hand, pseudocapacitors usually exhibit a small portion of their capacitance as electrostatic double-layer capacitance due to the ion adsorption/desorption in electrode/electrolyte interface.³³ Therefore, in practice, the capacitance behavior of pseudocapacitance can be considered as the sum of EDLC and the redox peaks, that is, the broadened peaks on top of a quasi-rectangular CV.⁴²

Another proposed explanation for the pseudocapacitance nature is based on the band structure of materials.^{44,45} In this model, charge/discharge process corresponds to electron transferring between different energy levels. As shown in Figure 1.9, for insulators, different redox sites are well separated and non-interactive, thus the energy levels are singular. Therefore, all the electrons will be the same energy level, resulting in a redox peak in CV curve of batteries. On the other hand, for semiconductors, the energy levels of these are no longer a single value but an energy band. In turn, the transfer of electrons occurs in a continuous range of potentials, instead of a fixed single potential. This model qualitatively explains why there is no redox peaks exist in CV curves of pseudocapacitors.

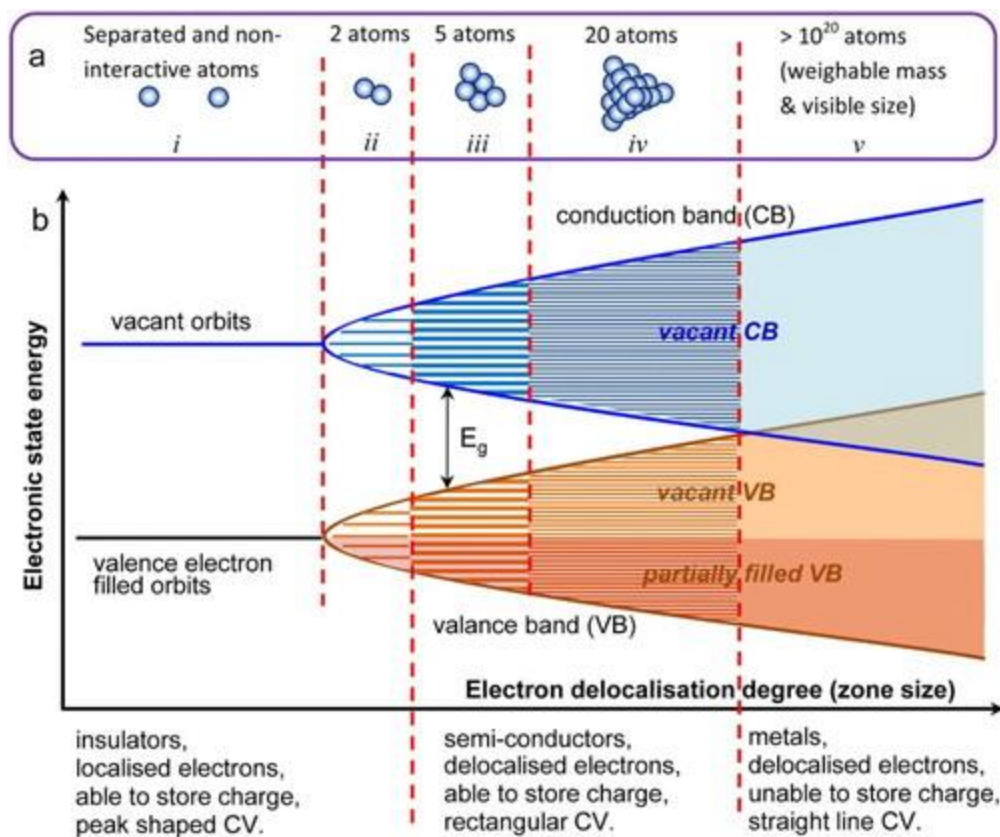


Figure 1.9. Schematic illustrations of the band model for chemical bonding (a) between metal atoms and (b) the corresponding energy levels of the valence electrons as a function of the degree of delocalization of valence electrons in the cluster of metal atoms. (© 2016 George Z. Chen, reprinted under the terms of the Creative Commons Attribution Non-Commercial No Derivatives 4.0 License, CC BY-NC-ND.)⁴⁵

1.3. Supercapacitor Configuration

In general, supercapacitors consist of a positive and a negative electrode, an electrolyte, and a separator, as shown in Figure 1.10. It is worth mentioning that in many papers, the anode is used for the negative electrode, while the cathode is used for the positive electrode. However, the usage of anode and cathode is based on the electrochemical redox reaction, i.e. the anode

materials are being oxidized and the cathode materials are being reduced. This terminology is appropriate in primary non-rechargeable batteries since only one type of redox reaction (oxidation or reduction) is allowed in either electrode. Yet in a supercapacitor, the reactions are reversed during charge and discharge.⁴⁵ Moreover, in EDLC, energy are storage by physics process instead of redox reactions. Therefore, positive and negative electrodes should be the appropriate usage for supercapacitors.

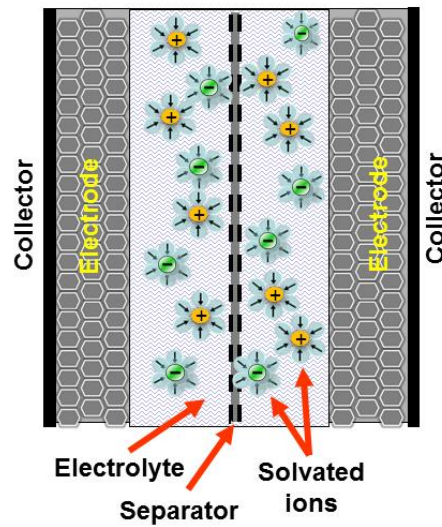


Figure 1.10. The basic configuration of an ideal supercapacitor.

For an ideal capacitor, the capacitance C is defined as the ratio of a charge Q to the potential

V :

$$C = \frac{Q}{V} \quad (1.18)$$

As shown in Figure 1.11, the relationship between charge and potential is constant through the entire charge and discharge process, therefore the capacitance of a supercapacitor is a constant value. On the other hand, the potential of the battery is independent of the extent charge added.

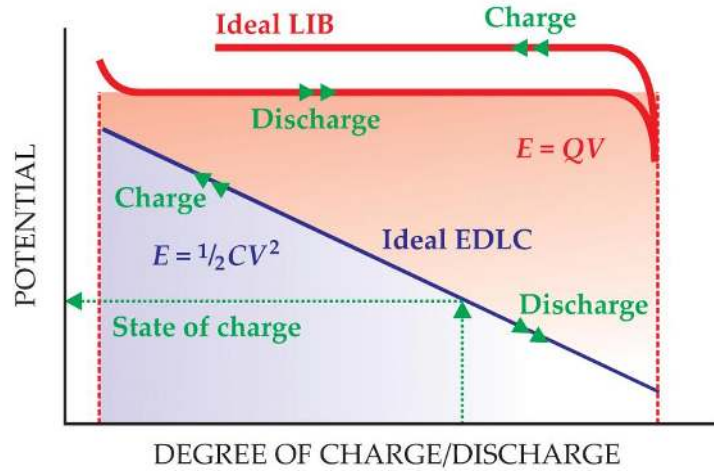


Figure 1.11. Comparison of the charge-discharge curves between supercapacitor and battery. (© 2008 American Institute of Physics, reprinted with permission.)⁴⁶

The energy storage in a supercapacitor can be calculated as

$$E = \int_0^Q V(q) dq = \int_0^Q \frac{q}{C} dq = \frac{1}{2} \frac{Q^2}{C} = \frac{1}{2} QV = \frac{1}{2} CV^2 \quad (1.19)$$

which is only half of that of the battery ($E=QV$).

The maximal power of a supercapacitor is given by

$$P_{\max} = \frac{V}{4R_{\text{ES}}} \quad (1.20)$$

where R_{ES} is equivalent series resistance.

In practice, the average power

$$P_{\text{avg}} = \frac{E}{t} \quad (1.21)$$

is often used.

Based on Eqn. 1.17 and 1.18, to achieve best performance, a supercapacitor should meet certain requirements, such as high capacitance, high voltage window, and low equivalent series resistance.

The electrode is the most important component of the supercapacitor. Based on the charge mechanism, electrode materials for supercapacitor can be classified into two categories: carbon-based materials for EDLCs; redox-active materials, such as metal oxides (nitrides, sulfides, and phosphides) and conducting polymers, for pseudocapacitors. Despite the fundamental difference, the proper material design is required to maximize the electrode performance for both types. From the material's perspective, several aspects need to be taken into account:^{47,48} 1) surface area and pore size distribution; 2) electronic/ionic conductivity; 3) electrochemical and mechanical stability. The details for each electrode material will be discussed in the next section.

Besides improving the properties of each component, the rational design of device configuration is also important to maximize the supercapacitor performance. As shown in Eqn. 1.17, the energy of a supercapacitor can be improved more effectively by increasing the capacitance or operation voltage because the energy density increases in proportion to squared voltage. However, the practical operational window is limited by several factors. For the aqueous electrolyte, the operation window is typically below 1 V, which is mainly due to the thermodynamic limit of water electrolysis.⁴⁹ Using organic or ionic liquid electrolytes can increase the operation window up to 3 V.⁵⁰ However, lower ion conductivity compared to that of aqueous electrolytes remains a major challenge of organic and ionic electrolytes, resulting in inferior device performance. Moreover, high cost, high toxicity, inflammability and other safety issues of organic and ionic electrolytes severely hinder their applications.⁵¹ On the other hand, electrodes, especially pseudocapacitance electrodes, have their own working potential windows, i.e. the irreversible

charge storage in each electrode, that is $Q_+ = Q_-$. Therefore, the mass or areal ratio can be given by:⁵⁴

$$\frac{m_+}{m_-} = \frac{C_{m-}V_-}{C_{m+}V_+} \text{ or } \frac{A_+}{A_-} = \frac{C_{A-}V_-}{C_{A+}V_+} \quad (1.23)$$

For symmetrical supercapacitors, because the positive and negative electrodes have the same working potential range, the capacitance of them must be equal. However, this is more complicated in the case of ASC. According to Eqn. 1.21, the electrode voltages are crucial in determining the ASC performance. Figure 1.13 illustrated the concept of supercapacitor maximum charging voltage (MCV), potential of zero voltage (PZV), and electrode capacitive potential range (CPR).⁵⁵ CPRs are determined by the lower and upper potential limits of positive and negative electrodes, E_{N1} , E_{N2} , E_{P1} , and E_{P2} , respectively. PZV is the equal potential of both electrodes when an ASC is fully discharged. In most cases, the CPRs of negative and positive electrodes are overlapped, therefore, PZV should be in-between E_{P1} and E_{N2} . If $PZV - E_{N1} > E_{P2} - PZV$, and the capacitances of two electrodes are equal, we have $MCV = (E_{P2} - PZV) \times 2$. In this case, MCV is determined by the upper potential limit of the positive electrode. On the other hand, since the CPRs of both electrodes are usually different, it is unnecessary to have equal capacitance. In this case, the relationships of charge storage, capacitance, potential ranges and specific energy of each electrode and the cell are:⁵⁶

$$Q = C_P U_P = C_N U_N \text{ or } U_N = U_P \frac{C_P}{C_N} \quad (1.24)$$

$$C_{cell} = \frac{C_P C_N}{(C_P + C_N)} = \frac{C_P}{(1 + C_P/C_N)} \quad (1.25)$$

$$U = U_P + U_N = U_P \left(1 + \frac{C_P}{C_N} \right) \quad (1.26)$$

$$E = \frac{CU^2}{2} = \frac{1}{2} C_P U_P^2 \left(1 + C_P/C_N \right) \quad (1.27)$$

where $U_P = E_P - \text{PZV}$ and $U_N = \text{PZV} - E_N$.

Clearly, raising the C_P/C_N ratio would increase the cell voltage U and cell energy E , even though decrease the cell capacitance C_{cell} . In addition, unequalisation of electrode capacitances can avoid the wasted potential, i.e. the difference between MCV of equal and unequal conditions as shown in Figure 1.13. However, in practice, U_P and U_N and often unknown as PZV is difficult to predict. Not to mention that varying the C_P/C_N ratio may lead to degradation of cycle stability resulting from the increasing potential beyond the CPR.⁵³ Therefore, careful attention must be paid in determining the electrode balance.

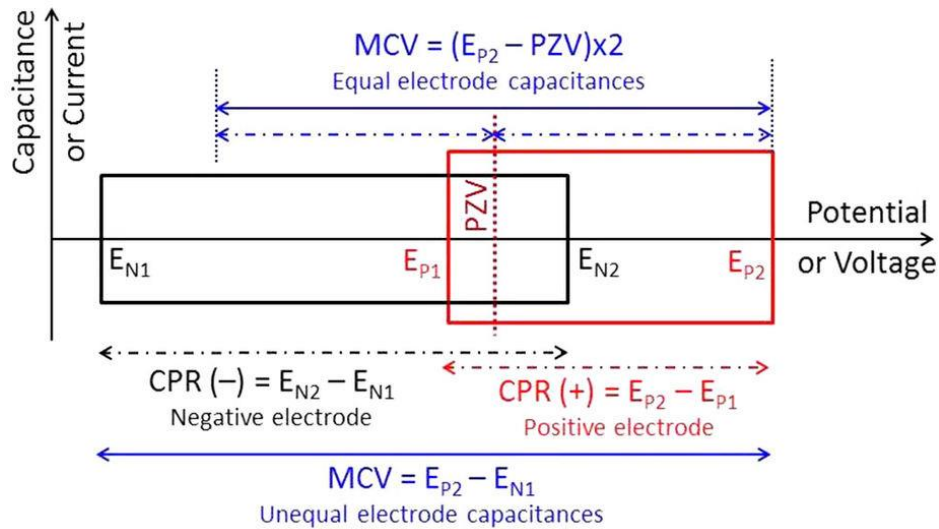


Figure 1.13. Schematic illustration of supercapacitor maximum charging voltage (MCV), potential of zero voltage (PZV), and electrode capacitive potential range (CPR). (© 2015 Nature Publishing

Group, reprinted under the terms of the Creative Commons Attribution Non-Commercial No Derivatives 4.0 License, CC BY-NC-ND.)⁵⁵

Another strategy in improving the energy is to fabricate a hybrid supercapacitor. In contrast to ASC, a hybrid supercapacitor consists one capacitance electrode and one battery-like electrode. In such hybrid systems, we can combine the high power of supercapacitors and high energy of batteries. Many hybrid supercapacitors have been developed, such as Li-ion capacitor, Na-ion capacitor, acidic battery-supercapacitor hybrid device, and alkaline battery-supercapacitor hybrid device.⁵⁷ Figure 1.14 shows the comparison of a symmetric EDLC using AC as both electrodes, and a Li-ion capacitor using $\text{Li}_4\text{Ti}_5\text{O}_{12}$ as negative electrode and AC as positive electrodes.⁵⁸ In the typical symmetric configuration, the voltage profiles of both electrodes are linear (blue lines). By replacing the positive electrode using the battery-type material, the potential remains constant associated with the phase change (red lines). It is well known that the area between the voltage profiles of positive and negative electrodes represents the energy storage. Therefore, the Li-ion capacitor can store more energy than symmetric EDLC. The energy can be calculated by:⁵⁹

$$E_h = (1 - k_1)(1 - k_2) \frac{1}{2} \frac{q_1 V}{m_1} \quad (1.28)$$

where k_1 and k_2 are the ratio of mass and working potential range between the battery-type electrode and the cell, q_1 and m_1 are the energy storage and mass of the EDLC electrode. Compared to that of symmetric configuration:

$$E_s = \frac{1}{2} \frac{1}{2} \frac{q_1 V}{m_1} \quad (1.29)$$

to get a higher energy in the hybrid system, the mass of a battery-type electrode should be lower than half of the total mass of the system and the working potential range of the battery-type electrode cannot exceed $1/2^{0.5}$ of the total working potential range.

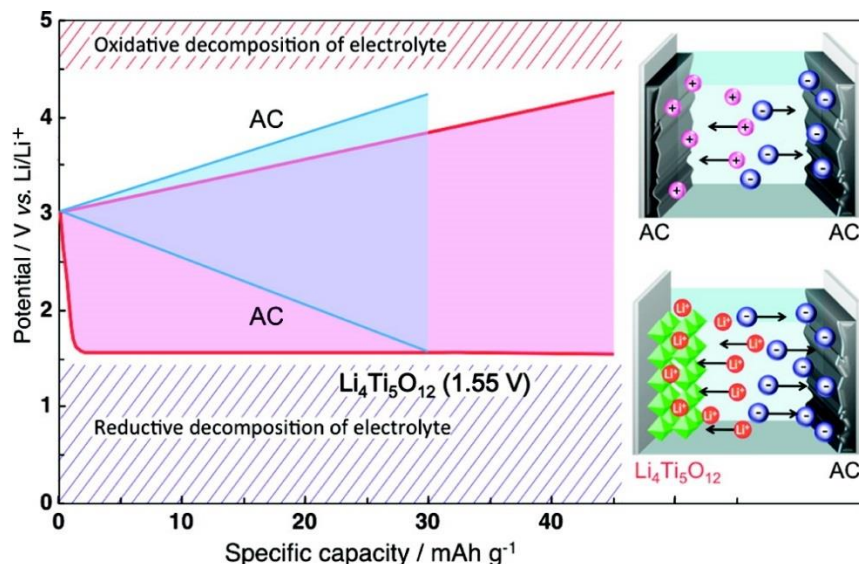


Figure 1.14. Typical voltage profiles and schematic device configurations of symmetric and hybrid supercapacitors. (© 2012 American Chemical Society, reprinted with permission.)⁵⁸

Recently, another novel concept called flow capacitor which is benefit from both flow battery and supercapacitor electrode has been developed. As shown in Figure 1.15a, the reverse flow of charged and discharged electrode materials creates a dynamic energy storage system. The charge is stored in the slurry of carbon particles by the means of EDLC mechanism (Figure 1.15b). Figure 1.15c shows the system architecture of a flow capacitor. The charged and discharged electrode materials are being stored in external reservoirs separately. During charge/discharge process, the discharged/charged slurry is pumped through the flow cell, respectively. Consequently, the decoupling of energy and power enables the flow capacitor to overcome the energy limitation of conventional supercapacitors, thus, making flow capacitor a promising candidate for grid-scale energy storage.^{60,61}

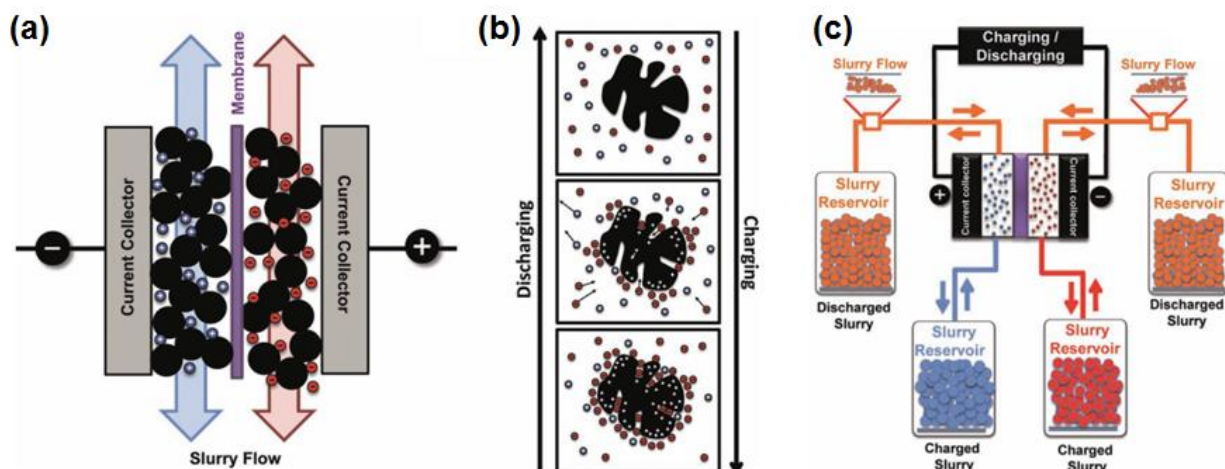


Figure 1.15. (a) The concept, (b) charge mechanism, and (c) system architecture of the flow capacitor. (© 2012 WILEY-VCH Verlag GmbH & Co. KGaA, Weinheim, reprinted with permission.)⁶⁰

The past decades have witnessed the rapid developing of the integrated circuit and portable electronic devices, consequently, new demands are emerging for supercapacitors and other energy storage systems. Integration of energy storage system with electronic circuits is challenging as conventional supercapacitors with sandwich or rolling structures are incompatible with planar geometries of most integrated fabrication processes.⁶² In addition, various advanced electronic devices hold specific requirements for energy storage systems. Thus, tremendous efforts have been made in developing supercapacitors with unconventional structure, including flexible, micro-, stretchable, compressible, transparent and fiber supercapacitors.⁶³ For example, micro-supercapacitors which utilize arrays of in-plane microelectrode fingers are highly promising for integration into integrated electronics.⁶⁴ On the other hand, flexible and fiber supercapacitors have attracted much attention due to the increasing demand of power system for flexible electronics and wearable system.^{65,66} Another recent advancement of supercapacitors is to integrate them with

various energy sources, such as solar cells, nanogenerators, and thermoelectric generators. The combination of energy conversion and energy storage in a single device provides a solution to simultaneously capture and store energy from the environment.⁶⁷

1.4. Electrode Materials

Regardless the configuration of supercapacitors, electrode materials play a crucial role in determining the overall performance of a supercapacitor device. Based on the charge mechanism, electrode materials can be classed into two categories, carbon-based materials for EDLCs, metal oxides (nitrides, sulfides, et al.) and conducting polymers for pseudocapacitors. Among them, carbon is the most widely used in commercial supercapacitors owing to its abundance, lower cost, easy processing, non-toxicity, higher specific surface area, good electronic conductivity, high chemical stability, and wide operating temperature range.⁶⁸ But extensive research has been conducted into pseudocapacitive materials due to their high specific capacitance. In addition, performance beyond the limitations of each material has been realized by implementing composite materials which combine the advantages of both EDLCs and pseudocapacitors.⁶⁹

1.4.1. Carbon Materials

A large variety of carbon materials, such as activated carbon, carbon nanotube (CNT) and graphene, have been investigated as supercapacitor electrodes.⁷⁰ Activated carbon is the most widely used electrode material for commercial EDLCs, but with the limited specific capacitance of about 100 F/g. CNTs and Graphene, on the other hand, could offer additional advantages as more effective electrode materials in supercapacitors owing to their large surface area, and good electrical properties.⁷¹ However, it is still challenging to further improve the performance of

supercapacitors based on carbon materials. Taking graphene as an example, the restacking of graphene sheets leads to the unsatisfied specific capacitance between 100 to 300 F/g compared to the theoretical value of 550 F/g.⁷² In addition, the high cost of CNTs and graphene limits their widespread applications.

For all carbon materials, the electrochemical performance is influenced by several important factors, such as specific surface area, pore-size distribution, pore shape and structure, electrical conductivity, and surface functionality.²⁷ In general, carbon material with larger specific surface area presents higher capacitance as more charges accumulate in the electrode/electrolyte interface.⁷³ However, as we discussed in section 1.2.1, the capacitance of carbon materials is not always propagation to the surface area. The pore distribution is another major factor which affects the electrochemical performance. It is believed that macropores and mesopores facilitate ion diffusion kinetic and thus improve the rate capacity, while the role of micropores is to increase the ion-accessible surface area and capacitance.⁷⁴ Therefore, rational design of porosity of carbon materials is of great importance to maximize the electrochemical performance. Different methods have been adopted to carbon materials to create multiscale pores, ranging from micropores to macropores. The templet method is most commonly used to control the pore structure of the carbon materials. The general procedure of templet method is to synthesize or deposit carbon or carbon precursors on a well-defined templet, followed by carbonization if carbon precursors are used, and finally, remove of the templets, leave behind the porous carbon structure.²⁷ Various materials have been studied as templets to produce porous carbons, including silica, metal oxides, inorganic salts and sublimable organic compounds.⁷⁵

In addition to high surface area and pore size distribution, heteroatom doping is another efficient method to improve the performance of carbon materials. The idea of doping is to

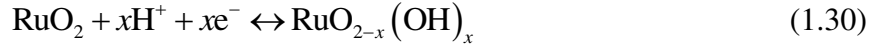
introduce various functional groups on the surface of carbon materials or improve their electric conductivity and charge transport capability. Three methods are generally used in doping process for carbon materials: i) the carbonization of a heteroatom rich precursor, ii) post-treatment in heteroatom containing atmosphere, and iii) grafting of molecules containing suitable functional groups.⁷⁶ Different heteroatom dopants have been extensively studied, such as oxygen, boron, nitrogen, sulfur, and phosphorous.

1.4.2. Transition Metal Oxides

Although carbon materials exhibit numerous advantages for supercapacitor electrode, their capacitance is relatively small. Pseudocapacitance materials can provide much higher capacitance owing to the different charge mechanism. Particularly, transition metal oxides are of great interest because of their variety of oxidation states available for redox charge transfer.⁷⁷ In 1971, RuO₂ was discovered to exhibit the pseudocapacitance profile for the first time.⁷⁸ Since then, various metal oxides (MnO₂,^{79–81} Co₃O₄,^{82–84} Fe₂O₃,^{85–87} V₂O₅,^{88,89} NiO,^{90,91} CuO,^{92,93} MoO₃,^{94–96} Nb₂O₅,⁹⁷ SnO₂,⁹⁸ TiO₂,^{99–101} WO₃,^{102,103} et al.) have been widely investigated. In general, the charge storage in transition metal oxides are based on two mechanisms, redox pseudocapacitance and intercalation pseudocapacitance.¹⁰⁴

After the first demonstration of pseudocapacitance, RuO₂ has been extensively studied for more than four decades. Owing to its wide potential window, highly reversible redox reactions, three distinct oxidation states, high proton conductivity, remarkably high specific capacitance, good thermal stability, long cycle life, metallic-type conductivity, and high rate capability, RuO₂ has been considered as one of the most promising candidates for supercapacitor application.⁴⁷ The

charge/discharge of RuO₂ is based on the rapid reversible electron transfer of protons when the oxidation states of Ru changes between +2 and +4:³³



where $0 \leq x \leq 2$. It has been noted that combined water plays an important role in the electrochemical performance of RuO₂. In fact, the existing of hydrated water would benefit the cation diffusion via hopping of alkaline ions and H⁺ ions between H₂O and OH⁻ sites, thus enhance the proton transport.¹⁰⁵ Specific capacitance of 1340 F/g has been reported by utilizing RuO₂ nanoparticles dispersed onto activated carbon,¹⁰⁶ which is close to the theoretical value of 1450 F/g.

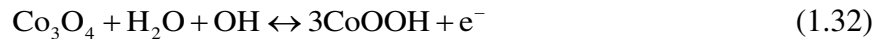
However, the high cost and toxicity of Ru limit its practical applications. Therefore, other inexpensive and environmentally friendly metal oxides have been investigated as alternatives. MnO₂, characterized by its high specific capacitance, low-cost, abundance and environmentally friendly nature, is another well studied pseudocapacitance metal oxide.¹⁰⁷ In general, charge storage of MnO₂ occurs through the redox reaction of Mn between the +4 and +3 oxidation states:¹⁰⁸



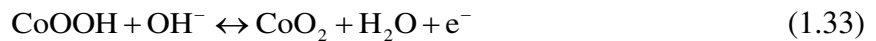
where C⁺ denotes the protons and alkali metal cations (Li⁺, Na⁺, K⁺, et al) in the electrolyte. The main challenge for MnO₂ is its low electrical conductivity. Thus, charge storage in MnO₂ mainly occurs within a thin layer of the surface, leading to the significantly lower capacitance (ranging between 200 and 250 F/g) than the theoretical value (1233 F/g). One method to compensate for

the poor electrical conductivity of MnO₂ is to process into ultrathin film, which can achieve specific capacitances of more than 1000 F/g.¹⁰⁹

Recently, spinel metal oxide, with a general formulation AB₂O₄, have received increasing attention owing to its robust crystalline architecture with three-dimensional diffusion pathways. Many metal oxides with spinel structure have been investigated for supercapacitors, including Co₃O₄, Fe₃O₄, Mn₃O₄ and mixed transition metal oxides such as NiCo₂O₄ and MnFe₂O₄. For example, Co₃O₄ has an ultrahigh theoretical specific capacitance as 3560 F/g originates from the following redox reactions:¹¹⁰



However, a second redox reaction of the electrochemically formed cobalt oxyhydroxide may occur during the charge/discharge process,³⁴



In turn, the electrochemical signature of Co₃O₄ combines pseudocapacitive and battery contributions. Such confusion exists in most Co and Ni based materials, such as Co₃O₄, NiO, Co(OH)₂, Ni(OH)₂, and NiCo₂O₄ as discussed in section 1.2.2.

Another important metal oxide electrode material is Fe₂O₃, due to its high theoretical specific capacitances, natural abundance, low cost, and non-toxicity.¹¹¹ The pseudocapacitive performance of Fe₂O₃ originates from the reversible electrochemical oxidation/reduction reaction between Fe³⁺ and Fe²⁺.¹¹² One merit making Fe₂O₃ stand out is that it serves as the negative electrode, while most of other metal oxides can only be used as positive electrodes. However, the same challenge remains in developing high-performance Fe₂O₃ supercapacitor as for MnO₂, that

is, the poor electric conductivity.¹¹³ In addition, iron-based materials usually suffer from the inferior cycling stability resulting from the physiochemical change/structural deformation during the long-time redox reaction.^{114,115}

Above mentioned metal oxides are all based on redox process. Another important group of metal oxides exhibit pseudocapacitance behavior yet due to a different mechanism, that is, ion intercalation. The key advantage of such material is to balance the intrinsic differences of charge/discharge rate of the electrodes in hybrid supercapacitors. In general, intercalation pseudocapacitive material exhibits an open, layered structure that enables fast ion transport.¹⁷ Several metal oxides have been studied as intercalation pseudocapacitive material, including TiO_2 , V_2O_5 , Nb_2O_5 , and MoO_3 . In contrast to redox pseudocapacitive oxides, the crystal structure is crucial in intercalation pseudocapacitive oxides. For example, monoclinic phase TiO_2 , usually denoted as $\text{TiO}_2(\text{B})$, has more open structures than anatase or rutile phases, therefore the lithium storage is controlled by the capacitive intercalation. Whereas in anatase and rutile, the solid-state diffusion of Li^+ dominates the overall capacity.^{116,117} Compared to battery-type intercalation materials, one unique feature of pseudocapacitive intercalation materials is that there is no significant crystallographic phase change in the charge storage.^{118,119}

Although metal oxides show great promising in supercapacitor electrode, the poor electrical conductivity has severely limited their application. Several methods have been developed aiming to address this issue. For instance, the electrical conductivity can be improved by controlling the oxygen vacancies in metal oxide materials. Hydrogen treatment has been proved as an efficient way to enhance the electrochemical performance on TiO_2 ,¹²⁰ MnO_2 ,¹²¹ and MoO_3 .¹²² Other oxygen deficient annealing atmosphere can also be used, such as nitrogen or argon, to avoid the unwanted reduction of certain metal oxides.⁸⁵ In addition to thermal annealing, the oxygen

vacancies can be also introduced using chemical or electrochemical methods, in which the degree of reduction can be better controlled.^{101,123}

Besides introducing the oxygen vacancies, the electrical conductivity can also be improved by doping. Not only modulate the electrical properties, the introduction of extrinsic impurities also improve ion diffusion and create new valence states of metal oxides.¹²⁴ Both metal (such as Au¹²⁵ and Ti¹²⁶) and non-metal (such as S¹²⁷ and B¹²⁸) have been investigated as efficient dopants to boost the electrochemical performance of metal oxides.

1.4.3. Transition Metal Sulfides, Nitrides and Phosphides

Metal sulfides, such as CuS,¹²⁹ CoS,¹³⁰ and NiS,¹³¹ are recently receiving more and more interest as electrode materials for supercapacitors due to their high electrical conductivity.¹³² Among the various metal sulfides evaluated, NiCo₂S₄ is considered as one of the most promising electrode material for supercapacitor by providing much higher electrochemical activity and specific capacitances than those of monometal sulfides, as well as more than 100 times higher conductivity than the corresponding oxide, NiCo₂O₄.¹³³ To date, specific capacitance in the range of 1000 – 2000 F/g has been reported in various structures of NiCo₂S₄ based materials.¹³⁴ Another group of interesting metal sulfide is transition metal dichalcogenides (TMDCs), such as VS₂, MoS₂ and WS₂.^{135,136} With the similar 2D structure as graphene, TMDCs provide facial ion intercalation channels between nanosheets, thus are favorable for fast charge storage.¹³⁷ Moreover, transition metal dichalcogenides with metallic 1T phase are of special interest for supercapacitor, as they present much higher conductivity.¹³⁸ However, the charge mechanism of most metal sulfides are unclear, therefore more fundamental studies are still needed.¹⁰⁴

Similar to metal sulfides, metal nitrides are considered as promising electrode materials for supercapacitors owing to their high conductivity. Numerous studies have demonstrated the utilization of a variety of metal nitrides, such as nitrides of Ti, V, Mo, and W, in supercapacitor electrodes.¹⁴¹ Interestingly, most of the metal nitrides are used as the negative electrode in supercapacitors. It is reported that the pseudocapacitance of metal nitrides are origin from the surface-modified oxides or oxynitrides.¹⁴¹ Yet, the poor stability remains a major challenge for metal nitrides.¹⁴²

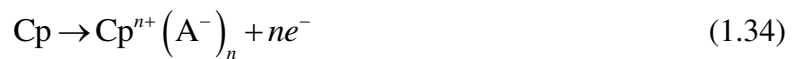
As an interesting class of multifunctional materials, metal phosphides exhibit superior electrical conductivity and redox activity, together with other advantages, such as earth abundance and environment-friendly.¹⁴² Therefore, they are considered as promising materials for supercapacitor electrodes. However, they haven't been studied as supercapacitor electrode materials until very recently. There have been a few reports on metal phosphide-based electrode materials, mainly focused on nickel phosphide,^{143–150} cobalt phosphide,^{151–153} and copper phosphide,¹⁵⁴ as well as bimetallic phosphide, in practical nickel cobalt phosphide.^{155–157} As inspired by metal nitrides, one should expect certain metal phosphides to be good negative electrode material. However, to the best of our knowledge, the use of metal phosphides as a negative electrode material for supercapacitors remains unexplored.

1.4.4. Conducting Polymers

Conducting polymer (CP) were first discovered in 1977 by Shirakawa, MacDiarmid and Heeger,¹⁵⁸ who were awarded the 2000 Nobel Prize in Chemistry. CP was exploited as supercapacitor electrode material in the mid-1990s, and have drawn increasing attention thereafter.¹⁵⁹ The most commonly used CPs for supercapacitor electrode are polyaniline (PANi),

polypyrrole (PPy), polythiophene (PTh) and its corresponding derivatives. CPs have a low band gap (1-3 eV) and high conductivity (from a few S cm^{-1} to 500 S cm^{-1}) compared with conventional polymers. The conductivity of such polymers arises from a so-called “doping” process by chemical or electrochemical oxidation/reduction process, which a large number of delocalized π electrons formed on the conjugated bond system along the polymer backbone. Analogous to silicon semiconductors, the terms “p-doped” and “n-doped” were used to describe the results of oxidation and reduction. From the band structure point of view, when oxidized (p-doping), electrons were removed from the valence band, creating intermediate band structures which facilitate electronic transport.¹⁶⁰ When reduced (n-doping), electrons insert into the conduction band. In practice, most CPs are p-doped.

The redox reaction in CP associated with the intercalation and deintercalation of ions. The ions from the electrolyte are transferred into the polymer backbone during charging and then release into electrolyte through discharging. In differ from other pseudocapacitance materials, the charge storage of CP can also be described as the doping process. When positive charged, CPs are p-doped with anions, while negative charged CPs are n-doped with cations. The simplified equations for these two charging processes are as follows:¹⁵⁹



Similarly, the discharging can be treated as “un-doping” process. Since the redox process happens in the bulk of the material, rather than only on the surface, CP-based supercapacitor can provide high energy density. Another benefit of CPs is their inherent flexible polymeric nature, which makes them apposite for flexible supercapacitor applications.¹⁶¹

One unique characteristic of CP electrode is that the electrochemical properties can be well controlled by doping type and doping rate. Four types of CP-based supercapacitor can be constructed.¹⁶⁰ A type I device uses two identical p-doped CP for both electrodes. When fully charged, the positive electrode is fully doped and the negative electrode reminds un-doped state. When fully discharged, both electrodes are half-doped (Figure 1.16a). For type I device, the overall operation window V is the same as the potential windows of each electrode. A type II device uses two different p-doped CP with distinct potential windows. The one with a higher potential window serves as the positive electrode whereas the other with a lower potential window is the negative electrode. When fully charged, two electrodes behave the same as type I device (Figure 1.16b). After fully discharged, both electrodes are partially doped due to the difference in the potential window. Compared to type I device, type II device has a higher operation window, resulting in a higher energy density. Type III and IV devices are different from type I and II devices in the fact that both p-doped and n-doped CPs are used, making them operated as asymmetric supercapacitors. In type III device, the same CP which can be p-doped and n-doped is used as both electrodes with the p-doped form used as the positive electrode and the n-doped form used as the negative electrode. In fully charged condition, both electrodes can be fully doped (Figure 1.16c). Owing to the higher operation window, type III device has higher energy density than type I and II devices. However, the p-doping and n-doping capability are usually different in CP, given by the fact that p-doped CPs are usually more stable than n-doped CPs. Therefore, both electrodes remain slightly p-doped even when the device has been fully discharged. To solve this problem, a type IV device was developed. Similar to type III, type IV device consists a p-doped positive electrode and a n-doped negative electrode. The difference between type III and IV device is that the potential windows of two electrodes in type IV are well separated. In this way, both electrodes return to the neutral state

(Figure 1.16d). The type IV device has the highest cell operation window, resulting in the highest energy density among these four types of devices.

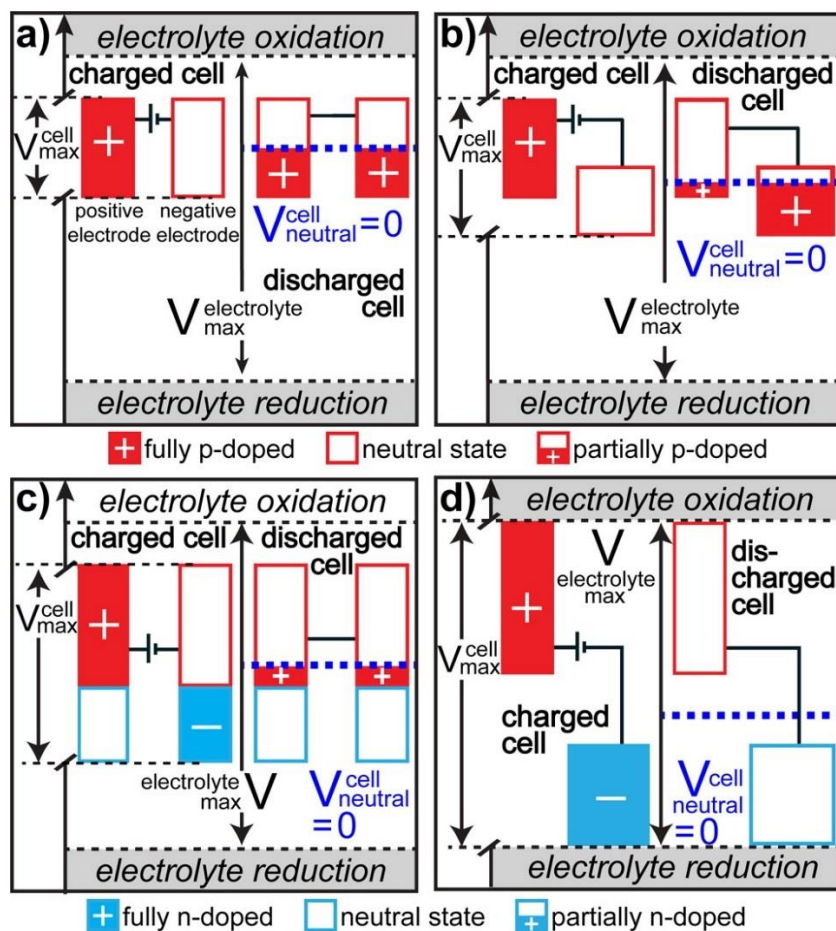


Figure 1.16. Potential diagrams of fully charged and discharged states of (a) Type I, (b) Type II, (c) Type III and (d) Type IV CP-based supercapacitor. (© 2016 American Chemical Society, reprinted with permission.)¹⁶⁰

Unfortunately, poor stability remains the major issue for most CP-based electrodes. The primary reason causes such problem is the repeated swelling and shrinking, and eventually structural the pulverization of CPs during charge/discharge.¹⁶² Several approaches have been investigated to improve the stability: (1) Improving structures and morphologies of CP materials. By reducing the diffusion length, nanostructured CP could reduce cycling degradation problems

caused by volumetric changes. (2) Hybridizing supercapacitor device. Since n-doped CPs are less stable than p-doped ones, one strategy is to replace the negative electrode with other more stable materials, especially carbon-based materials. (3) Fabricating composite electrode materials. CP/carbon composite has been demonstrated as one of the most promising candidates for supercapacitor electrode since it combines the large pseudocapacitance of CP and the good mechanical and chemical stability of carbon, as well as good conductivity of both materials.⁴⁷

1.4.5. The Role of Nanomaterials in Supercapacitor Electrodes

Despite different materials used in supercapacitor electrodes, the charge of supercapacitors are mainly located on or near the very surface of electrode materials, engineering the nanostructured materials has been proved as an efficient approach improve the performance.¹⁶³ It has been widely accepted that the progress in supercapacitor can benefit by nanostructured materials include:⁷⁷

1. Nanostructured electrodes enlarge the surface area noticeably compared to bulk electrodes, therefore provide more ion adsorption sites for EDLCs or more charge transfer active sites for pseudocapacitors.

2. Both electronic and ionic conductivity can be enhanced by precisely tailoring the pore structure, resulting in the improved specific capacitance and rate capability.

3. Nanostructured engineering of electrode materials can also modify the phase change during charge/discharge, avoid undesirable side reactions, and improve the mechanical stability, therefore leading to higher cycling stability.

4. Nanostructured materials offer additional properties for advanced device configuration otherwise difficult to achieve for bulk or thin film materials, such as lightweight, flexibility, transparency.

1.5. Overview of this Dissertation

The work presented in this thesis is focused on the synthesis of three-dimensional nanomaterials and their application in supercapacitor electrodes. Two groups of pseudocapacitance material have been studied: metal oxides (Chapter 2) and metal phosphides (Chapters 3 and 4).

Chapter 2 will report the one-step hydrothermal synthesis method of TiO₂ nanorod arrays on Ti substrate and their applications on supercapacitor. A possible “dissolve and grow” mechanism of the TiO₂ nanorods growth will be discussed in detail based on systematically structural characterization. As the supercapacitor electrode, the TiO₂ nanorod arrays exhibit good areal capacitance and excellent cyclic stability by retaining more than 98% of the initial specific capacitance after 1000 cycles. In addition, a good flexibility of the Ti foil with TiO₂ nanorod arrays was demonstrated by the stable electrochemical performance under different bending angles.

In **Chapter 3**, three-dimensional CoP nanowire and nanosheet arrays were synthesized on carbon cloth by a two-step method and were utilized as the binder-free supercapacitor negative electrodes. The as-synthesized CoP nanowire arrays presented a high capacitance of 571.3 mF/cm² at a current density of 1 mA/cm². By using CoP nanowire arrays as the negative electrode and MnO₂ nanowire arrays as the positive electrode, a flexible solid-state asymmetric supercapacitor has been fabricated and has exhibited excellent electrochemical performance, such as a high energy density of 0.69 mWh/cm³ and a high power density of 114.2 mW/cm³. In addition, the solid-state asymmetric supercapacitor shows high cycle stability with 82% capacitance

retention after 5000 charge/discharge cycles. In addition, the areal capacitance can be further improved by successive sulfidation.

Chapter 4 focus on the further enhancement of the supercapacitance performance of metal phosphide materials with conducting polymer coating. FeP/PEDOT core/shell nanorod arrays have been demonstrated as a high-performance negative electrode with an excellent areal capacitance of 790.59 mF/cm² and significantly improved cycling stability of 82.12% retention after 5000 cycles. Compared to bare FeP nanorod arrays, not only the areal capacitance, but also the stability has been improved significantly. Moreover, an aqueous ASC device was fabricated using MnO₂ positive and FeP/PEDOT negative electrodes with excellent capacitance and energy density.

Chapter 2 TiO₂ Nanorod Arrays on Ti Substrate for Supercapacitor Application

2.1. Introduction

Titanium dioxide (TiO₂) has the long history of the usage in numerous commercial productions, such as pigment and in sunscreens, paints, ointments, toothpaste, etc.¹⁶⁴ Since the discovery of the photocatalytic water splitting,¹⁶⁵ TiO₂ has drawn tremendous attention in extensive promising applications of solar cells, photocatalysts, Li-ion batteries, smart coatings, etc.¹⁶⁶

TiO₂ shows many advantages such as low cost, natural abundance and environmentally friendly, making it a very promising electrode material for supercapacitors. However, it suffers from poor electrical conductivity and low specific surface area, leading to a relatively low specific capacitance.¹⁶⁷ To overcome such limitations, nanostructures have been demonstrated to be unique in facilitating the fast ion diffusion and electron transfer, thus dramatically boosting the electrochemical performance. Among different nanoarchitectures, three-dimensional nanostructures, such as nanorod, nanowire and nanotube arrays, exhibit additional advantages such as providing direct pathways for ion/electron transport and large surface area for charge storage enhancement.¹⁶⁸ Different methods have been reported to synthesize 3D TiO₂ nanostructures including template sol-gel,¹⁶⁹ anodic oxidation,¹⁷⁰ and chemical vapor deposition (CVD) methods,¹⁷¹ although instrumental complexity poses high investment costs as well as limits of scalability. In this respect, low-cost solution-based methods are of immense interest for inexpensive mass production. Hydrothermal growth is one of simplest and most cost-effective solution-based synthesis methods, which can achieve not only high-purity nanostructures with

Part of this chapter was published in Zhi Zheng *et al.* One-step synthesis of TiO₂ nanorod arrays on Ti foil for supercapacitor application, *Nanotechnology*, 2014, 25 (43), 435406.

high-crystallinity but also can be easily scaled up for large area nanostructures fabrication for various device applications.^{172,173}

In this chapter, we demonstrate a facile one-step hydrothermal method to grow TiO₂ nanorod arrays directly on Ti foil and Ti wire for supercapacitor application. Owing to the unique 3D configuration of TiO₂ nanorod arrays, a decent electrochemical property with high specific capacitance and excellent cycling stability was achieved. In addition, the flexible supercapacitor electrode using Ti foil with TiO₂ nanorod arrays was also demonstrated.

2.2. Experiments

2.2.1. Synthesis of TiO₂ nanorod arrays

TiO₂ nanorod arrays on Ti foil or Ti wire was synthesized via a hydrothermal method. Titanium foil (0.5 mm thickness) or wire (0.81 mm diameter) was first cleaned with acetone, and then etched in 18 wt% HCl solution at 85 °C for 10 min to remove the native oxide layer. In a typical hydrothermal procedure, titanium substrate was placed in a Teflon-lined stainless steel autoclave filled with a 2.5 wt% HCl aqueous solution and kept at 180 °C for 12 h. After the synthesis, the autoclave was cooled down naturally to room temperature. After being dried in air, the samples were annealed at 600 °C under argon atmosphere for 1 h.

2.2.2. Material Characterizations

Field-emission scanning electron microscopy (FESEM) images were taken on a Carl Zeiss 1530 VP microscope. Transmission electron microscopy (TEM) experiments were conducted on a JEOL 2010 transmission electron microscope equipped with X-ray energy dispersive spectroscopy (EDS). Cross-section TEM analysis and EDS mapping were conducted on a JEM-

2100 F-field emission TEM equipped with Oxford EDS spectroscopy. X-ray photoelectron spectroscopy (XPS) spectrum was recorded with an XPS system (Perkin-Elmer Phi 560) and the binding energy was calibrated using the C 1s photoelectron peak at 284.6 eV as the reference. X-ray diffraction (XRD) patterns were recorded on Philips X'Pert-MPD X-ray diffractometer with Ni-filtered Cu K α radiation (40 kV, 40 mA).

2.2.3. Electrochemical Measurements

The electrochemical properties were investigated by a Gamry Reference 600 electrochemical workstation. A typical three-electrode experimental cell equipped with a prepared Ti foil served as the working electrode, a platinum foil as the counter electrode, and an Ag/AgCl as the reference electrode was used for measuring the electrochemical properties of the working electrode. Cyclic voltammetry (CV) of the electrode was obtained at different scan rates of 1, 2, 5, 10, 20, 50, 100, 500 and 1000 mV/s in the potential range of -0.2 to 0.6 V. Galvanostatic charge/discharge curves were measured in the potential range of 0 to 0.6 V at different current densities of 10, 20, 50 and 100 $\mu\text{A}/\text{cm}^2$. The stability of the electrode was tested by galvanostatic charge/discharge measurement during 1000 cycles at a current density of 100 $\mu\text{A}/\text{cm}^2$. Electrochemical impedance spectroscopy (EIS) measurements were carried out at a direct current bias of 0.1 V, with a signal of 5 mV, over the frequency range of 0.1 to 100 kHz. Mott-Schottky plots were measured at a frequency of 10000 Hz. All the electrochemical measurements were performed in 1 M Na₂SO₄ solution at room temperature.

2.3. Results and Discussion

2.3.1. Growth Mechanism

Figure 2.1a and b show typical FESEM images of the as-grown TiO₂ nanorod arrays on Ti foil after the hydrothermal reaction. As seen in Figure 2.1a, TiO₂ nanorods with clear tetragonal shape were grown from the entire surface of the Ti foil. The inset, enlarged from one nanowire tip, shows pyramid shape with the tetragonal edge arranging from 50-200 nm. A cross-sectional view of the TiO₂ nanorod arrays is shown in Figure 2.1b, revealing the nanorods grew out randomly from the Ti foil with length about 1 μm long. The crystal structure of the nanorods was determined by XRD as shown in Figure 2.1c and all diffraction peaks are in good agreement with the tetragonal rutile phase (JCPDS No. 88-1175) except the peaks from the Ti foil, as denoted by asterisks. XPS (Figure 2.1d) was further employed to confirm the chemical composition and oxide state of the nanorods through photoelectron peaks of Ti and O. The binding energies of Ti 2p_{3/2} and Ti 2p_{1/2} peaks observed at 458.8 eV and 463.4 eV, respectively, with a spin orbit splitting of 4.6 eV (shown in Figure 2.1e), match with the values for bare TiO₂ very well,¹⁷⁴ suggesting that the oxidation state of the Ti in the nanorods is 4.

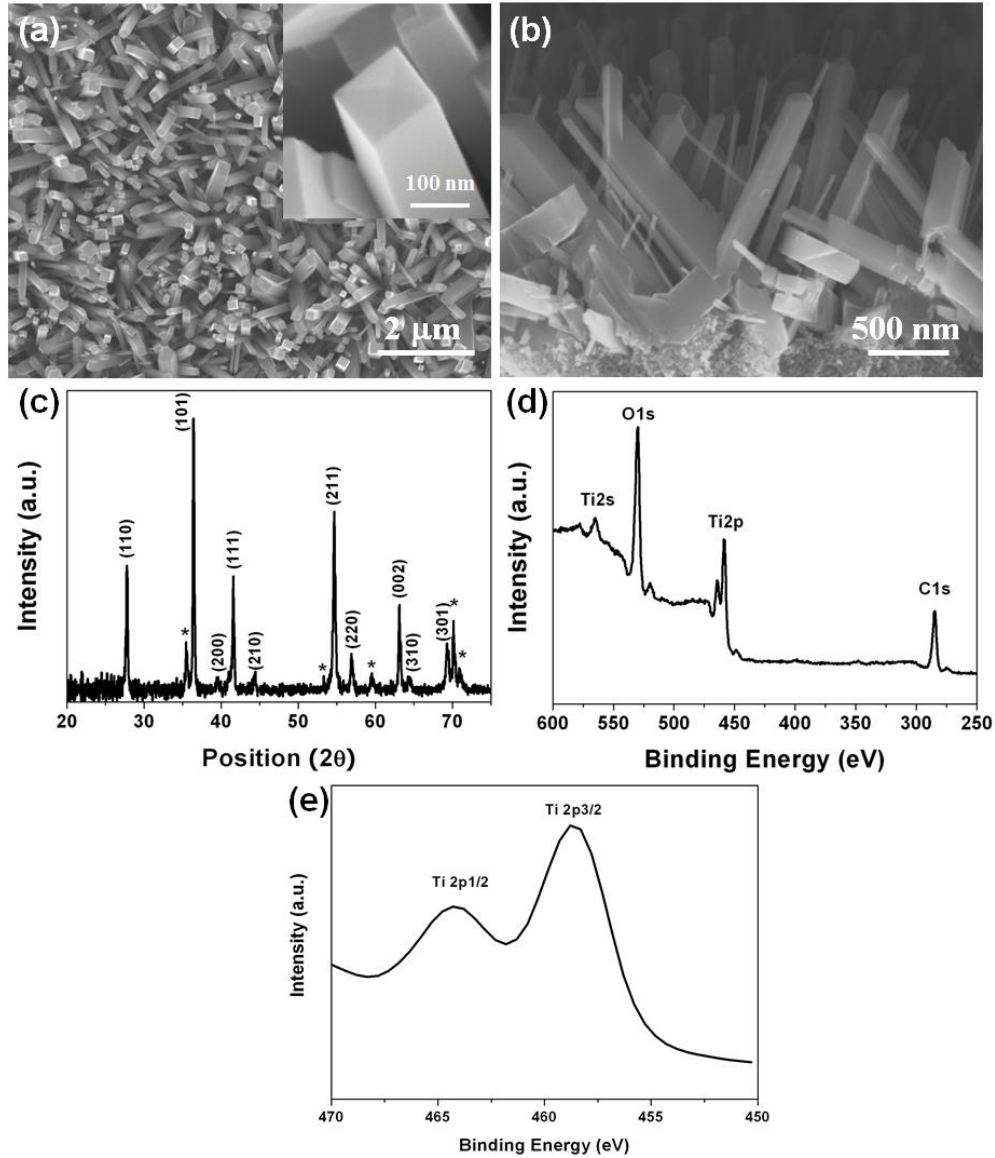


Figure 2.1. (a) Top view and (b) cross-sectional FESEM images of TiO₂ nanorod arrays on Ti foil. The inset in (a) is enlarged images of TiO₂ nanorod tip. (c) XRD pattern, (d) XPS survey spectra and (e) Ti 2p XPS spectra of TiO₂ nanorod arrays.

Traditional electronic devices have typically been fabricated from rigid plates, which restrict the flexibility, shape, weight, and integration of the cells, and result in some complexities in transport and installation. Fiber-shaped electronic devices show an impressive potential to

overcome those disadvantages. Herein, we have confirmed that this simple hydrothermal method can be applied to the synthesis of TiO₂ nanorod arrays on Ti wire. As can be seen from Figure 2.2, the entire surfaces of the Ti wire are covered uniformly by TiO₂ nanorods. The morphology of TiO₂ nanorods on Ti foil and Ti wire are the same, indicating the same growth process.

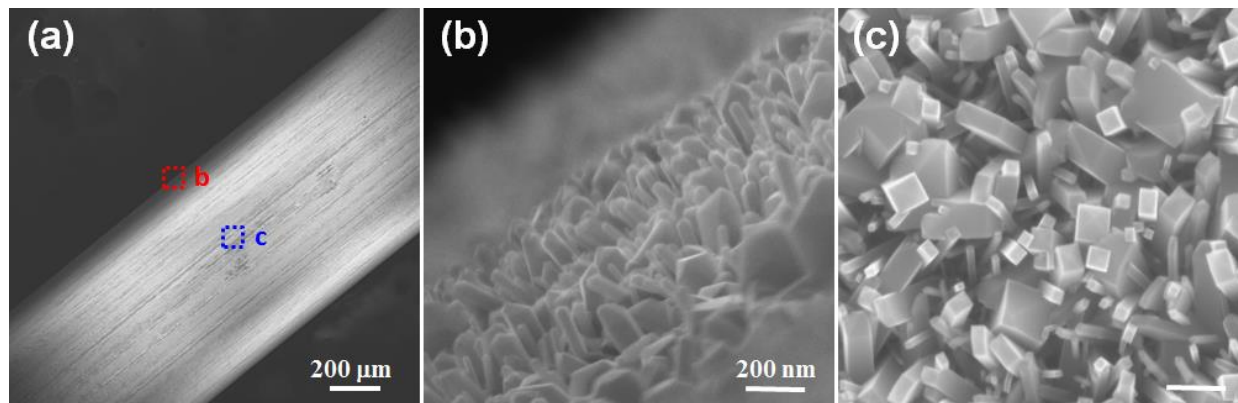


Figure 2.2. FESEM images of TiO₂ nanorod arrays on Ti wire. (a) low-magnification, (b, c) high magnification from squares b and c in panel a.

The morphology and structures of the TiO₂ nanorods were further characterized by using TEM. Figure 2.3a is the low-magnification TEM image of a single TiO₂ nanorod. The corresponding selected-area electron diffraction patterns (SADP) taken from [110] (Figure 2.3b) and [111] (Figure 2.3c) zone axis reveal the single-crystalline feature of the nanorod, which can be indexed to the pure rutile TiO₂ phase. From the SADPs, the growth direction of the TiO₂ nanorod can be easily determined along the [001] direction, which agrees with the tetragonal crystal shape and pyramid tip observed under FESEM. The EDS spectrum shown in Figure 2.3d further confirms the successful synthesis of TiO₂ nanorods. The phase and crystal structure of the TiO₂ nanorod were confirmed with high-resolution TEM (HRTEM) image shown in Figure 2.3e and f. The distance between lattice fringes, 0.23 and 0.22 nm, are consistent with (200) and (111) of the rutile TiO₂ phase, respectively.

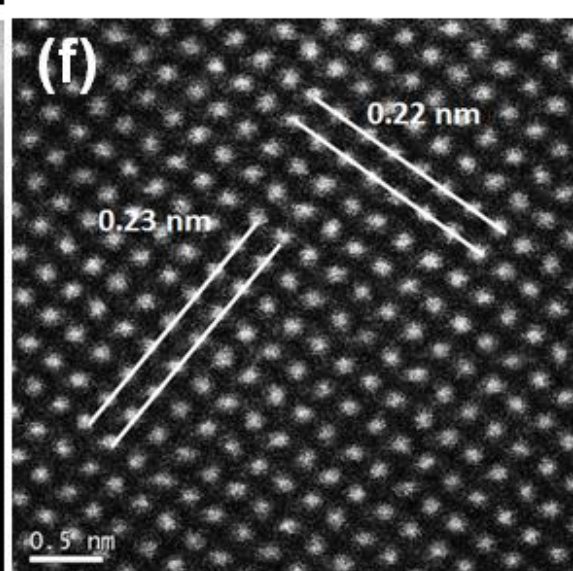
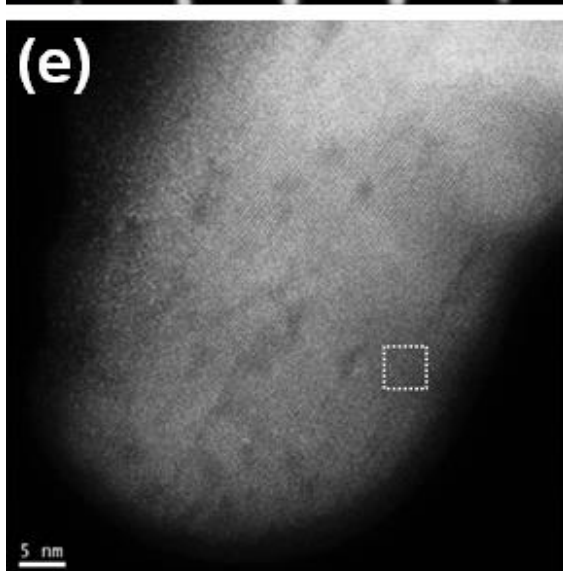
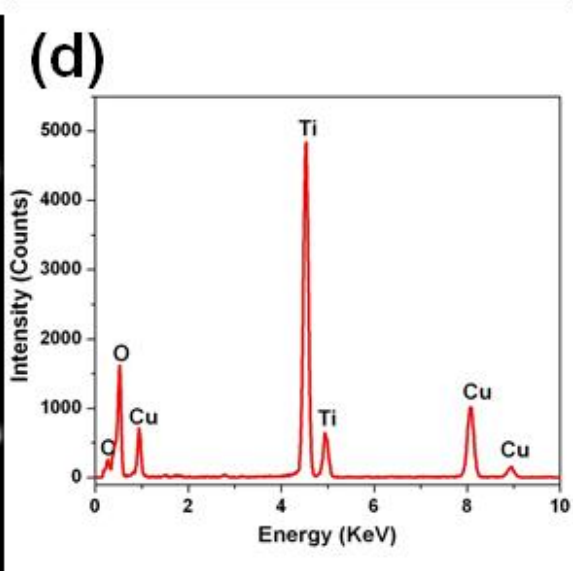
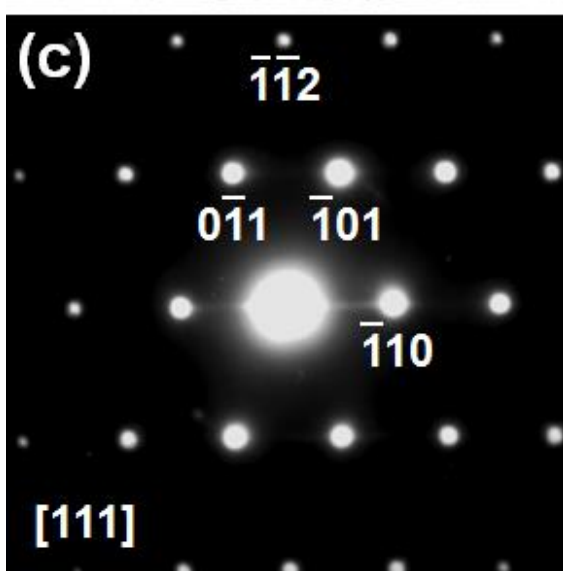
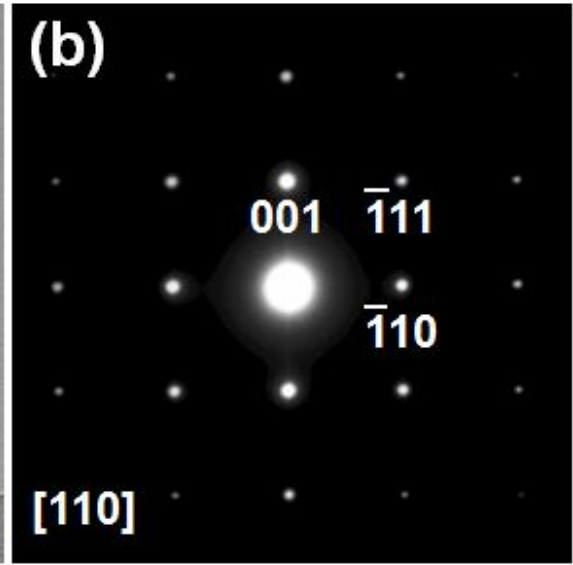
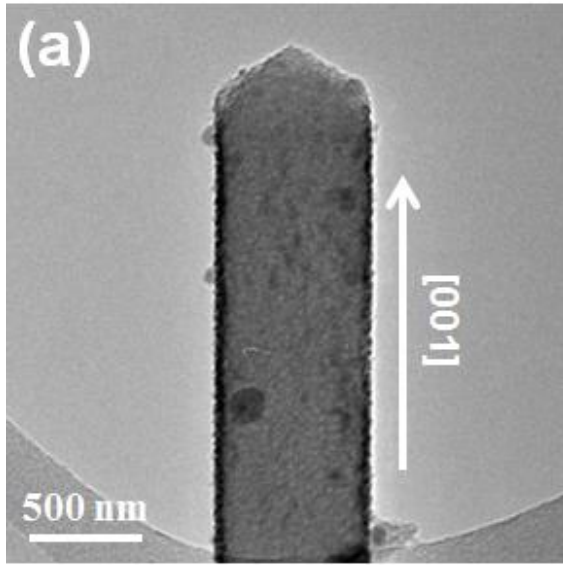


Figure 2.3. (a) TEM image of an individual TiO₂ nanorod. (b) and (c) are SADPs taken from [110] and [111] zone axis, respectively. (d) EDS spectra of an individual TiO₂ nanorod. The Cu peak originates from the copper grid for TEM observation. (e) and (f) HRTEM image of a single TiO₂ nanorod.

To better understand the growth mechanism of TiO₂ nanorods, a cross-sectional TEM specimen of the TiO₂ nanorod arrays was prepared by focused ion beam (FIB). As shown in Figure 2.4a, a buffer layer between TiO₂ nanorod and Ti substrate can be observed. Note the nanorod is much shorter than average length because it has been broken during the FIB process. The detail EDS spectra from each area can be found in Figure 2.4b. The corresponding EDS mapping images of Ti and O distribution are displayed in Figure 2.4c and d, respectively, clearly indicating the formed buffer layer between TiO₂ nanorods and Ti substrate is composed of Ti and O, whose structure will be further characterized below.

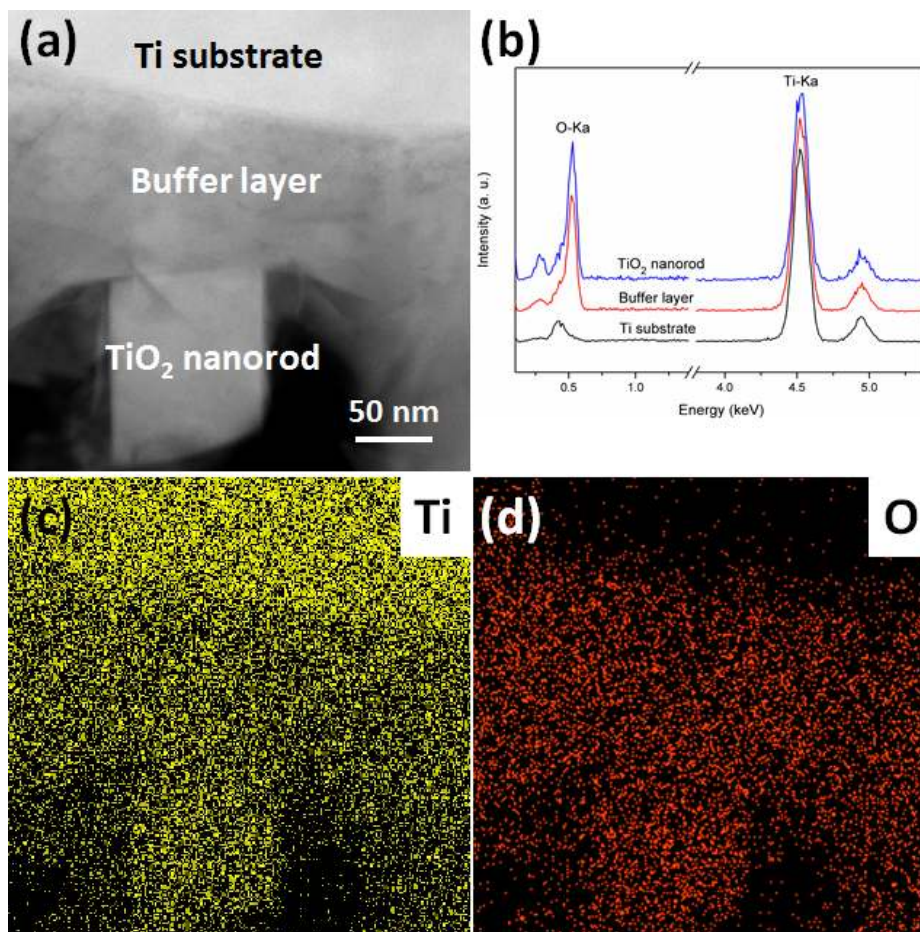


Figure 2.4. (a) STEM dark field image of Ti/TiO₂ interface. (b) EDS spectra of each area in panel a. (c) and (d) are EDS elemental mappings corresponding to titanium (Ti) and oxygen (O), respectively.

Figure 2.5a is a low magnification bright-field TEM image, showing a rough Ti/TiO₂ interface. SAEDs, performed on different regions of areas b, c and d of the interface, are shown in Figure 2.5b-d, respectively. The diffraction pattern from the substrate (Figure 2.5b) can be indexed as pure Ti hexagonal close-packed structure. Besides the diffraction spots from single crystal TiO₂ nanorod, denoted in the small rings in Figure 2.5c, there is also the presence of diffraction rings in the diffraction pattern from the interface. Such diffraction rings can be indexed as rutile TiO₂ (simulated with the PCED2.0 program),¹⁷⁵ which further confirms the formation of polycrystalline

TiO₂ in the buffer layer. Figure 2.5d shows the SADP taken from the area with several small TiO₂ nanorods, in which the diffraction rings can be indexed to the rutile TiO₂ phase, matching EDS mapping results above. Furthermore, no special growth orientation between the nanorod and the substrate was observed. Based on the above experimental results, the possible growth mechanism of the TiO₂ nanorod is detailed as follows.

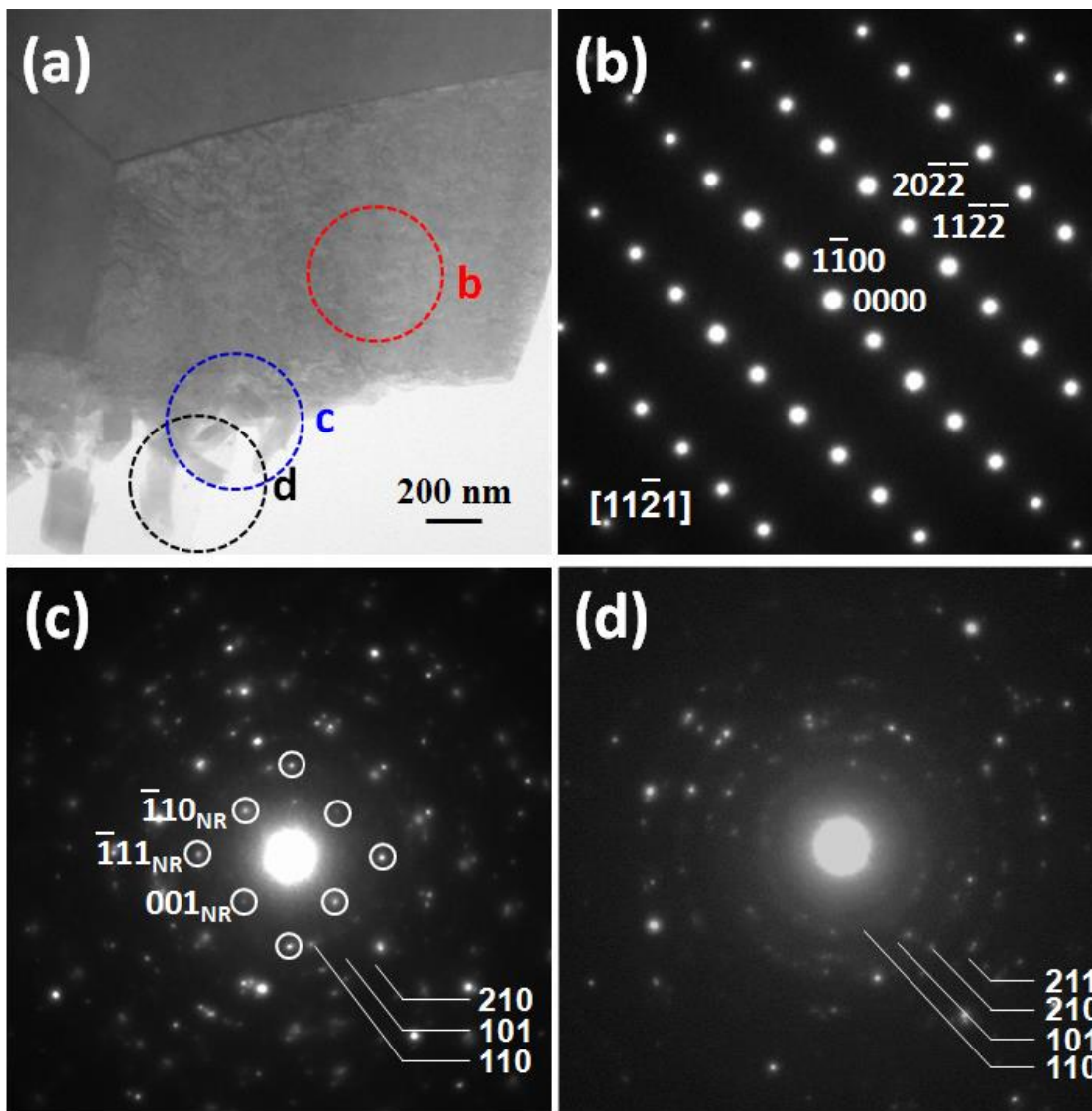


Figure 2.5. (a) Cross-sectional TEM image of Ti/TiO₂ interface. (b)–(d) Diffraction patterns taken from the circled areas b, c, and d in figure (a), respectively.

On the basis of the above experimental results, the possible “dissolve and grow” mechanism of the TiO₂ nanorod is proposed. The schematic diagram of the formation process is shown in Figure 2.6.

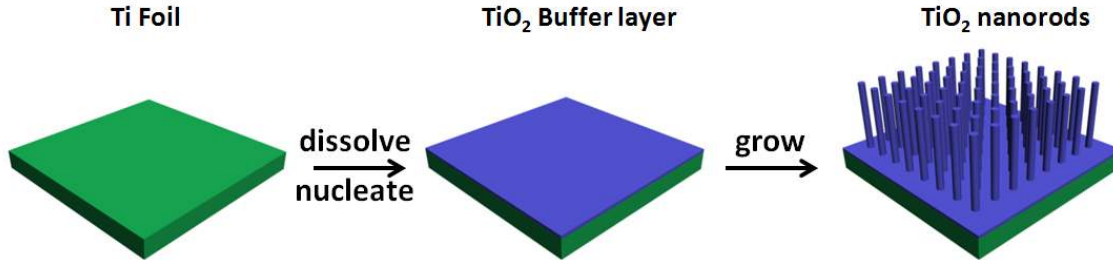
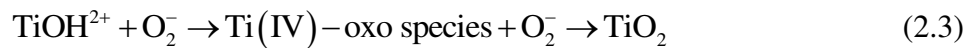
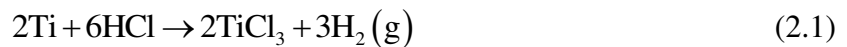


Figure 2.6. The schematic formation process of TiO₂ nanorod arrays on Ti foil.

At first, Ti substrate reacts with H⁺ in HCl solution at high temperature and pressure and gradually dissolves, releasing the Ti³⁺ precursors into the reaction solution continually. Ti³⁺ is easy to hydrolyze in aqueous solution, resulting in the production of TiOH²⁺. TiOH²⁺ is then reacted with dissolved oxygen forming Ti⁴⁺ precursors. The Ti⁴⁺ complex ions are thus used as the growth units for TiO₂. The overall reaction can be summarized as:^{176,177}



Apparently, due to the big polycrystalline grains of Ti substrate (Figure 2.5a) and different crystal structures between the TiO₂ (tetragonal) nanorods and the Ti (hexagonal) substrate, it is unlikely for TiO₂ nanorods to directly grow out from the Ti surface. Instead, TiO₂ polycrystalline buffer layer was observed to form on the surface of the Ti substrate (Figure 2.4). It is well known that the growth on the existing seeds is more favorable compared to the formation of new nuclei

because the heterogeneous nucleation in solution has a lower activation energy barrier than homogeneous nucleation.¹⁷⁸ Hence, the TiO₂ buffer layer can provide initial nucleation sites by reducing the nucleation energy. Since the buffer layer was composed of small randomly oriented TiO₂ crystallites, each nanorod tended to grow randomly, which is consistent with the cross-sectional SEM observation shown in Figure 2.1b. However, the growth rate of rutile TiO₂ nanorod follows the sequence of (110) < (100) < (101) < (001).¹⁷⁹ Therefore, TiO₂ nanorods growing along the [001] direction was eventually dominated

It should be noted that there are several reports claim that using the same method would grow Ti nanorod or Ti/TiO₂ core/shell nanorod arrays.¹⁸⁰⁻¹⁸⁴ Nevertheless, our comprehensive study clearly indicates the synthesis of TiO₂ nanorod arrays.

2.3.2. Electrochemical Performance

The electrochemical performance of TiO₂ nanorod arrays was investigated by cyclic voltammetry and galvanostatic charge/discharge measurements in a conventional three-electrode configuration. Figure 2.7a shows the CV curves of as-synthesized TiO₂ nanorod arrays on Ti foil at different scan rates. All the CV curves exhibit almost rectangular shapes without obvious redox peaks, indicating ideal supercapacitance behavior and fast charging-discharging process based on good charge propagation. The calculated areal capacitances as a function of scan rate are shown in Figure 2.7b. The capacitance values of the TiO₂ nanorod arrays are in the range of 81.2 to 174 $\mu\text{F}/\text{cm}^2$, as the applied scan rate is varied from 1000 mV/s to 1 mV/s.

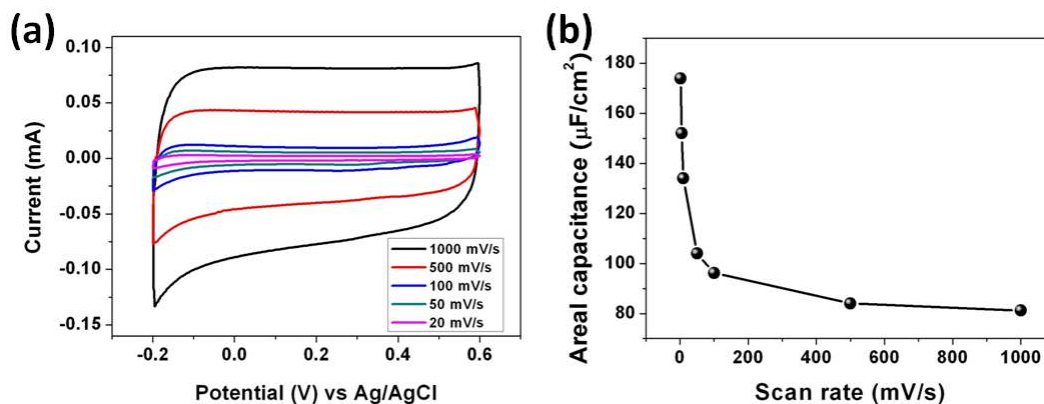


Figure 2.7. (a) Cyclic voltammetry curves of the as-synthesized TiO₂ nanorod arrays on Ti foil at different scan rates, (b) areal capacitance of the as-synthesized TiO₂ nanorod arrays on Ti foil as a function of scan rate.

The CV curves of TiO₂ nanorod arrays on Ti wire at the scan rate of 20-1000 mV/s were shown in Figure 2.8. Similar to TiO₂ nanorod arrays on Ti foil, the shapes of these curves are quasi-rectangular, indicating the ideal electrical double-layer capacitance behavior and fast charging/discharging process characteristic. The calculated specific capacitance is 64.8 μF/cm² at the scan rate of 1000 mV/s. As expected, the specific capacitance is similar as the value of TiO₂ nanorod arrays on Ti foil.

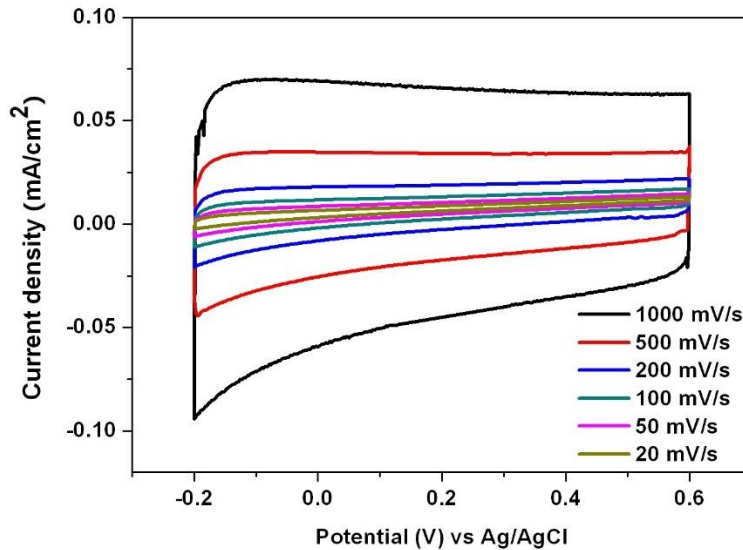


Figure 2.8. CV curves of TiO₂ nanorod arrays on Ti wire.

To further improve the performance, as-synthesized TiO₂ nanorod arrays were annealed in N₂ atmosphere. Figure 2.9a shows the CV curves of heat treated TiO₂ nanorod arrays at different scan rates. After heat treatment, the areal capacitance increases significantly and reaches 83.7 to 856.2 $\mu\text{F}/\text{cm}^2$ (Figure 2.9b), which is substantially higher than the values recently reported for TiO₂ nanoparticles (33 $\mu\text{F}/\text{cm}^2$ at scan rate of 100 mV/s)¹⁶⁷ and TiO₂ nanorod arrays on FTO glass (85 $\mu\text{F}/\text{cm}^2$ at scan rate of 100 mV/s).¹⁸⁵ The enhancement was due to the introduction of oxygen vacancies during heat treatment.¹⁸⁶ The electrochemical performance of TiO₂ nanorod arrays were further studied by galvanostatic charge/discharge method. Figure 2.9c illustrates the charge/discharge curves at different current densities of 10, 20, 50 and 100 $\mu\text{A}/\text{cm}^2$. The charge/discharge curves of the TiO₂ electrode show good symmetry and a small IR drop (0.07 V), indicating the TiO₂ nanorod arrays have ideal electrochemical capacitance behavior and good redox reaction reversibility.

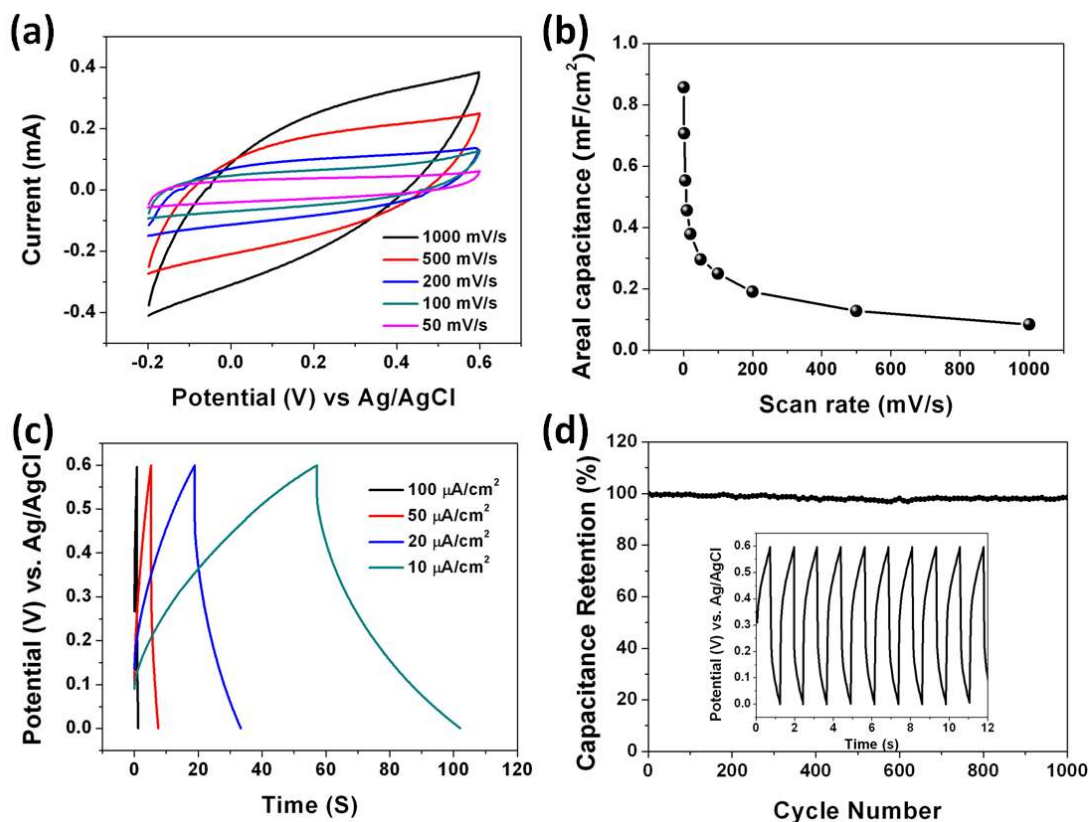


Figure 2.9. (a) Cyclic voltammetry curves of the TiO₂ nanorod arrays at different scan rates. (b) Areal capacitance of TiO₂ nanorod arrays as a function of scan rates. (c) Galvanostatic charge/discharge curves of TiO₂ nanorod arrays at different current densities. (d) Cycle performance of TiO₂ nanorod arrays measured by galvanostatic charge/discharge at a scan rate of 100 μA/cm² for 1000 cycles. Insert is the typical charge-discharge curves within ten cycles.

The long-term cycling stability is one of the most important characteristics for supercapacitor. The stability of TiO₂ nanorod arrays was tested by galvanostatic charge/discharge at 100 μA/cm² for 1000 cycles, and the results are shown in Figure 2.9d. The decrease of capacitance after 1000 cycles is less than 1.6%, revealing the TiO₂ nanorod arrays have a superior long-term cyclic performance. Meanwhile, as shown in the insert, the typical charge-discharge

curves within 10 cycles exhibit almost identical sharp triangular curve shapes, indicating a stable redox reaction, which further confirms the outstanding long-term stability.

EIS analysis was also measured to further understand the fundamental electrochemical behavior of TiO₂ nanorod arrays. The corresponding Nyquist plots are shown in Figure 2.10a. The impedance plot, as inserted, is composed of a semicircle arc in the high-frequency region followed by a linear response in the low frequency. The high-frequency region corresponds to the combined resistances of ionic resistance of the electrolyte, intrinsic resistance of the substrate, and contact resistance at the active material/current collector interface.¹⁸⁷ The linear part in the low-frequency region is related to the frequency dependence diffusive resistance of the ion diffusion at electrolyte/electrode interface. It is noticeable that the Nyquist plot shows a large slope at lower frequencies, indicating the high capacitive behavior of the TiO₂ nanorod arrays.¹⁸⁸ Figure 2.10b represents the Mott-Schottky plot observed in the range of positive dc potentials. The correlation between $1/C^2$ and the applied potential exhibits a positive linear dependence, indicating the n-type semiconductor nature. The carrier density calculated from the slope of this Mott-Schottky plot is $2.1 \times 10^{21} \text{ cm}^{-3}$, which is accordant with the expected values for TiO₂.¹⁸⁹

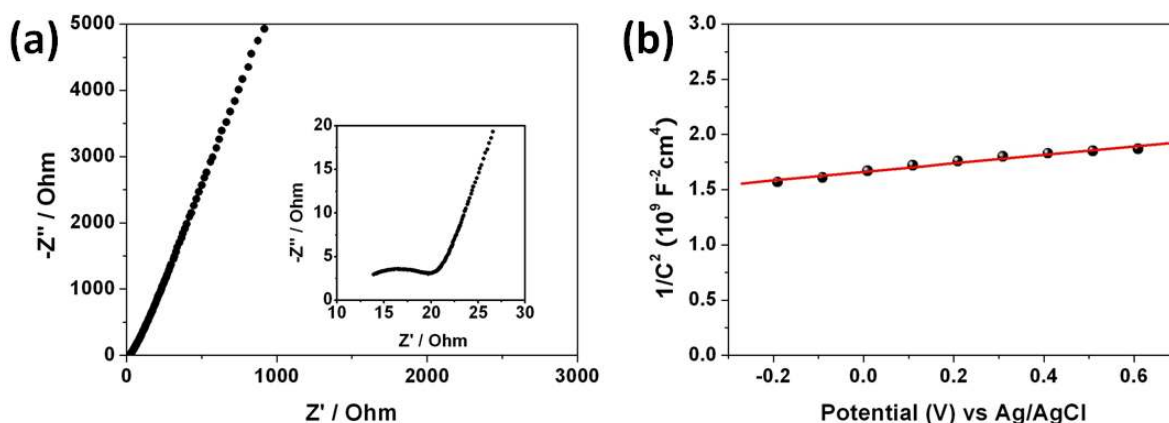


Figure 2.10. (a) The Nyquist plot and (b) Mott–Schottky plot of TiO₂ nanorod arrays. The inset in (a) shows the high-frequency part of the Nyquist plot.

To evaluate the feasibility of this TiO₂ nanorod arrays directly grown on Ti foil for flexible supercapacitor application, the cyclic voltammetry test under different bending conditions were performed. The foil with as-synthesized TiO₂ nanorod arrays shows high flexibility upon repeated bending (Figure 2.11a) and, more importantly, the CV curves collected did not significantly change under different bending angles (Figure 2.11b, c, and d), demonstrating that the TiO₂ nanorod arrays on Ti foil have high mechanical flexibility, which can be potentially applied for flexible supercapacitor fabrication.

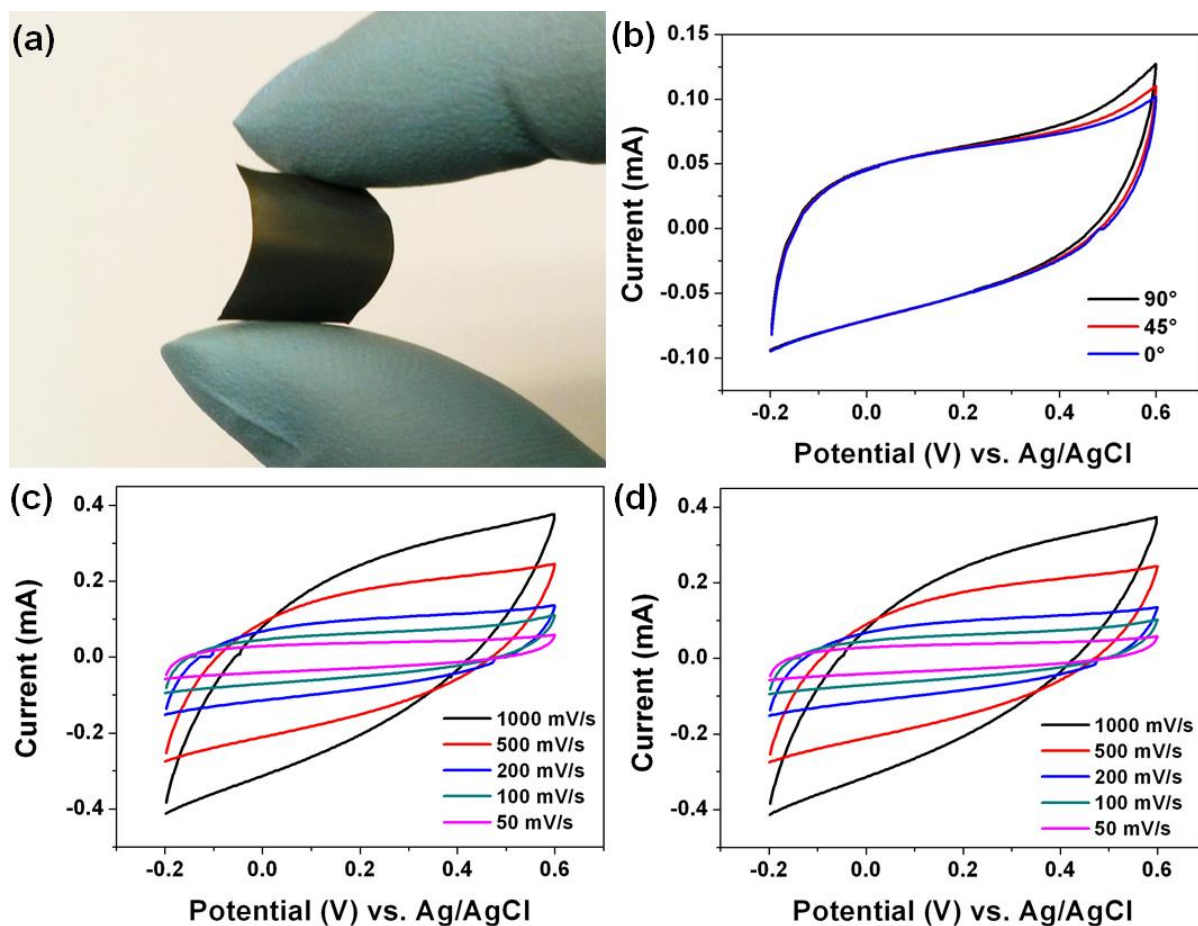


Figure 2.11. (a) Optical micrograph of bended Ti foil with TiO₂ nanorod arrays. (b) CV curves collected at 100 mV s⁻¹ under different bending conditions. CV curves of the TiO₂ nanorod arrays on Ti foil at different scan rates under (c) 45° and (d) 90° bending angles.

2.4. Conclusion

In summary, a facile one-step hydrothermal method is developed to directly grow TiO₂ nanorod arrays on Ti substrate. The TiO₂ nanorods are single rutile crystalline with [001] growth involving dissolving of the Ti substrate and growing of the nanorods. The electrochemical performance of the nanorod arrays, used as supercapacitor electrodes, was systematically investigated. The results demonstrate that TiO₂ nanorod arrays exhibit an ideal capacitive behavior, such as high specific capacitance and excellent cyclic stability. The TiO₂ nanorod arrays were further used as a flexible electrode and showed good stability under different bending conditions, which suggests that TiO₂ nanorod arrays grown directly on Ti foil can be employed for flexible energy storage applications as well.

Chapter 3 Nanostructured Cobalt Phosphide as Negative Electrode for Flexible Solid-State Asymmetric Supercapacitors

3.1. Introduction

In spite of the great improvement that has been achieved in developing positive electrode materials, the advancement of negative electrode materials has been relatively slow.^{190,191} Various materials have been studied as promising candidates for supercapacitor negative electrodes, such as carbon, transition metal oxides, and nitrides.^{27,89,114,127,192–196} Among them, metal oxides exhibit superior specific capacitance through fast and reversible surface Faradaic reactions during the charging/discharging process¹⁷ and, therefore, show great promise as negative electrode materials for supercapacitors. However, metal oxides often present a compromise of specific capacitance due to their poor intrinsic electrical conductivity.¹⁹⁷ Thus, it is still crucial to explore new classes of materials to further improve the negative electrode performance. As a class of interesting multifunctional semiconductors, metal phosphides have attracted much attention owing to their remarkable properties and various electrochemical applications, such as Li-ion batteries,¹⁹⁸ water splitting,^{199–202} and sensing.²⁰³ Compared with metal oxides, metal phosphides exhibit metallic properties and superior electrical conductivity, rendering them to be suitable supercapacitor electrode materials. Several research groups have reported that metal phosphides, such as Ni₂P,^{143,144,147–149,204} Ni₁₂P₅,¹⁴⁵ Co₂P,²⁰⁵ and NiCoP,¹⁵⁶ present excellent performance as positive electrode materials for supercapacitors. To the best of our knowledge, however, the use of metal phosphides as a negative electrode material for supercapacitors remains unexplored. In addition, using nanomaterials, especially three-dimensional nanowire arrays, which provide a large surface

Part of this chapter was published in: Zhi Zheng *et al.* Three-Dimensional Cobalt Phosphide Nanowire Arrays as Negative Electrode Material for Flexible Solid-State Asymmetric Supercapacitors, *ACS Appl. Mater. Interfaces*, 2017, 9 (20), 16986–16994.

area and short ionic and electronic diffusion paths, is one of the most promising strategies to improve the supercapacitance performance.^{163,206,207}

In this chapter, two different three-dimensional CoP nanostructures composed of nanowire and nanosheet arrays were synthesized on carbon cloth by a hydrothermal method followed by low-temperature phosphidation. Both nanostructures show excellent performance as supercapacitor negative electrodes, such as high capacitance and good rate capacity. In addition, high energy and power density, as well as good stability, have been achieved by designing a solid-state ASC based on a CoP nanowire array negative electrode, an MnO₂ nanowire array positive electrode, and a poly(vinyl alcohol) (PVA)/LiCl gel electrolyte, which demonstrates that the as-synthesized CoP nanowire arrays provide great potential for supercapacitor negative electrode material applications.

3.2. CoP Nanowire Arrays

3.2.1. Experiments

Materials

All reagents used in the experiments were of analytical grade and were used without further purification. Co(NO₃)₂·6H₂O was purchased from Alfa Aesar. NH₄F, NaH₂PO₂, KMnO₄, and urea were purchased from Sigma-Aldrich. Carbon cloth (AvCarb 1071 HCB) was purchased from Fuel Cell Store. A cellulosic separator (TF4030, NKK) was used to make the solid-state symmetric and asymmetric supercapacitors.

Synthesis of CoP Nanowire Arrays

CoP nanowire arrays on carbon cloth were synthesized by a two-step method.²⁰⁸ The carbon cloth (2 × 3 cm²) was first sonicated in acetone, ethanol, and deionized (DI) water for 30

min. $\text{Co}(\text{NO}_3)_2 \cdot 6\text{H}_2\text{O}$ (0.22 g), NH_4F (0.225 g), and urea (0.07 g) were dissolved in 15 mL of water and transferred to a 20 mL Teflon-lined stainless steel autoclave. The autoclave with a piece of carbon cloth was kept at 120 °C for 12 h. The sample was taken out and washed with DI water and ethanol thoroughly after the autoclave was cooled to room temperature. Once dried, the sample and NaH_2PO_2 were placed in a tube furnace with NaH_2PO_2 at the upstream side. The furnace was heated to 300 °C at 1 °C/min and kept for 2 h under 50 sccm Ar flow. The loading amount of CoP nanowire arrays was determined as 3.66 mg/cm² by a high precision microbalance. For comparison, cobalt oxide nanowire arrays were synthesized by annealing the sample in air.

Synthesis of MnO₂ Nanowire Arrays

MnO_2 nanowire arrays were synthesized by a hydrothermal approach.¹⁹³ KMnO_4 (2.5 mmol) and 1 mL of concentrated HCl were dissolved in 45 mL of water. The solution was then transferred into a 100 mL Teflon-lined stainless steel autoclave with a piece of carbon cloth and kept for 12 h at 140 °C. The sample was then annealed in air at 400 °C for 2 h. The loading mass of MnO_2 was about 2.47 mg/cm².

Material Characterizations

Field-emission scanning electron microscopy (FESEM) and transmission electron microscopy (TEM) images were obtained on a Hitachi S-4800 FESEM and a JEOL 2010 TEM, respectively. The elemental mapping and electron energy loss spectroscopy (EELS) mapping were obtained using scanning transmission electron microscopy (JEM-2400FCS, JEOL) equipped with a spherical aberration corrector, double Wien filter monochromator, X-ray energy-dispersive spectrometer (EDS) systems, and Gatan image filter system, which is operated at 60 kV. For the EELS analysis, the utilized energy dispersion is 0.1 eV per channel. The energy resolution for the EELS is 0.3 eV determined by the full width at half-maximum of the zero loss peak. The high-

resolution TEM (HRTEM) data were captured using the E-Titan equipped with an image corrector and operated at 300 kV. The X-ray photoelectron spectroscopy (XPS) spectrum was recorded on PerkinElmer Phi 560. A Philips X'PertMPD X-ray diffractometer was used for X-ray diffraction (XRD) measurements.

Fabrication of Solid-State Symmetric and Asymmetric Supercapacitor

The PVA/LiCl gel electrolyte was prepared by adding 12.6 g of LiCl and 6 g of PVA to 60 mL of water under vigorous stirring at 80 °C for 2 h. The electrode and separator were immersed in the prepared gel electrolyte for 10 min. To assemble symmetric supercapacitor (SSC), two identical CoP electrodes and a separator were sandwiched together and kept overnight in a drying oven. The ASC was assembled similarly to SSC except MnO₂ was used as the positive electrode and CoP was used as the negative electrode. The thickness of both SSC and ASC was measured to be 0.8 mm.

Electrochemical Measurements

A Gamry Reference 600 potentiostat was used for the electrochemical measurements. The electrochemical performance of the single electrode was measured in a three-electrode configuration in a 1 M LiCl aqueous electrolyte. A Pt foil and Ag/AgCl were used as counter and reference electrodes, respectively. Electrochemical impedance spectroscopy (EIS) measurements were conducted with a potential amplitude of 5 mV in the frequency range of 0.01 Hz to 100 kHz. For single electrode, the areal capacitance (C_a) of the single electrode is calculated from galvanostatic charge/discharge curves by the following equation:

$$C_a = \frac{I\Delta t}{A\Delta V} \quad (3.1)$$

where I is the discharge current, Δt is the discharge time, ΔV is the potential window during the discharge process removed by the IR drop, and A is the active area of the electrode.

The volumetric capacitance (C_v) of SSC and ASC are calculated from galvanostatic charge/discharge curves according to the following equation:

$$C_v = \frac{I\Delta t}{V\Delta V} \quad (3.2)$$

where I is the discharge current, Δt is the discharge time, ΔV is the potential window during the discharge process removed by the IR drop, and V is the volume of the total device.

The average energy density (E) and power density (P) of SSC and ASC are calculated by the following equation:

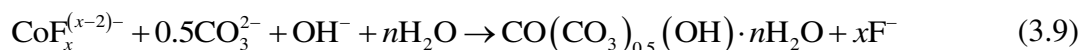
$$E = \frac{1}{2}C_v V^2 \quad (3.3)$$

$$P = \frac{E}{t} \quad (3.4)$$

3.2.2. Results and Discussion

CoP nanowire arrays on carbon cloth were synthesized by a two-step process (Figure 3.1a). The $\text{Co}(\text{CO}_3)_{0.5}(\text{OH})\cdot 0.11\text{H}_2\text{O}$ precursor was first synthesized by a hydrothermal method, followed by low-temperature phosphidation (Figure 3.1b). The reactions could be described as:²⁰⁹





During the phosphorization reaction, the NaH_2PO_2 was thermally decomposed to PH_3 , and serves as both the phosphorus source as well as the reducing agent.²¹⁰

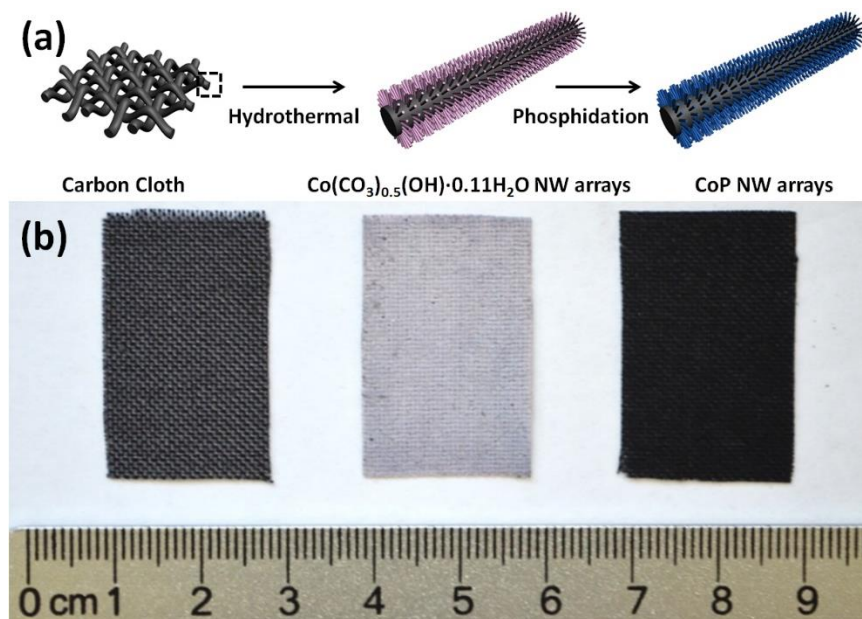


Figure 3.1. (a) Schematics of the synthesis procedure of CoP nanowire arrays on carbon cloth, (b) photograph showing (from left to right) blank carbon cloth, $\text{Co}(\text{CO}_3)_{0.5}(\text{OH}) \cdot 0.11\text{H}_2\text{O}$ and CoP nanowire arrays on carbon cloth.

The crystal structures of the $\text{Co}(\text{CO}_3)_{0.5}(\text{OH}) \cdot 0.11\text{H}_2\text{O}$ precursor and the CoP final product were determined by XRD, as shown in Figure 2a. All of the diffraction peaks of the precursor are in good agreement with orthorhombic $\text{Co}(\text{CO}_3)_{0.5}(\text{OH}) \cdot 0.11\text{H}_2\text{O}$ (JCPDS No. 48-0083), except the carbon peaks, as denoted by asterisks. After phosphidation, all of the diffraction peaks can be indexed as an orthorhombic CoP structure (JCPDS No. 29-0497) with no significant impurity peaks, suggesting successful synthesis with high purity of the CoP phase.²⁰⁸

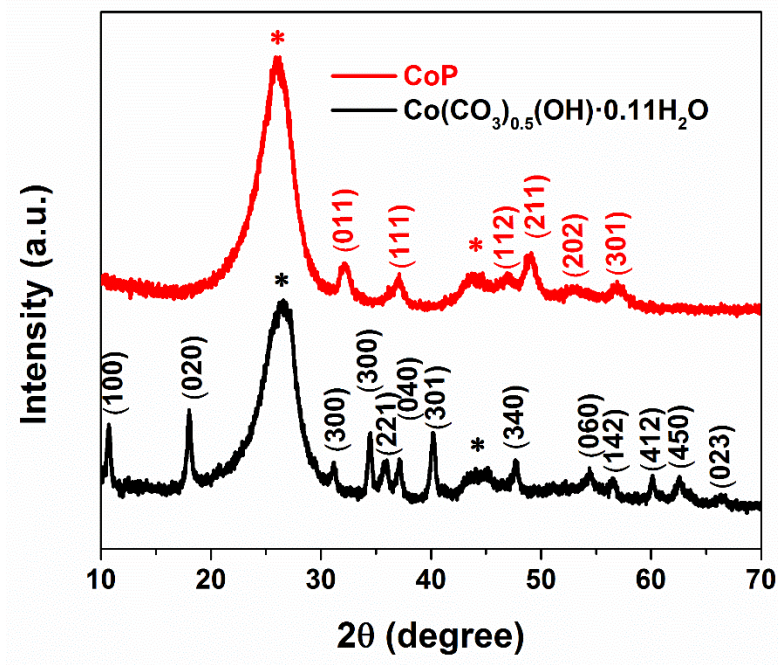


Figure 3.2. XRD patterns of $\text{Co}(\text{CO}_3)_{0.5}(\text{OH})\cdot 0.11\text{H}_2\text{O}$ and CoP nanowire arrays.

The typical FESEM images of Figure 3.3a show the uniform growth of $\text{Co}(\text{CO}_3)_{0.5}(\text{OH})\cdot 0.11\text{H}_2\text{O}$ on the carbon cloth in the form of nanowire arrays. As shown in the TEM image of Figure 3.3b, the solid $\text{Co}(\text{CO}_3)_{0.5}(\text{OH})\cdot 0.11\text{H}_2\text{O}$ nanowire presents a smooth surface. The corresponding selected-area electron diffraction patterns of $\text{Co}(\text{CO}_3)_{0.5}(\text{OH})\cdot 0.11\text{H}_2\text{O}$ (Figure 3.3c) shows single crystalline feature, and can be indexed as orthorhombic phase ($a = 8.792 \text{ \AA}$, $b = 10.15 \text{ \AA}$, $c = 4.433 \text{ \AA}$). The growth direction can be determined as the [010] direction, which agrees well with the previous reports.^{211,212} The EDS spectrum (Figure 3.3d) shows only the peaks of Co, O and C, along with Cu from the TEM grid.

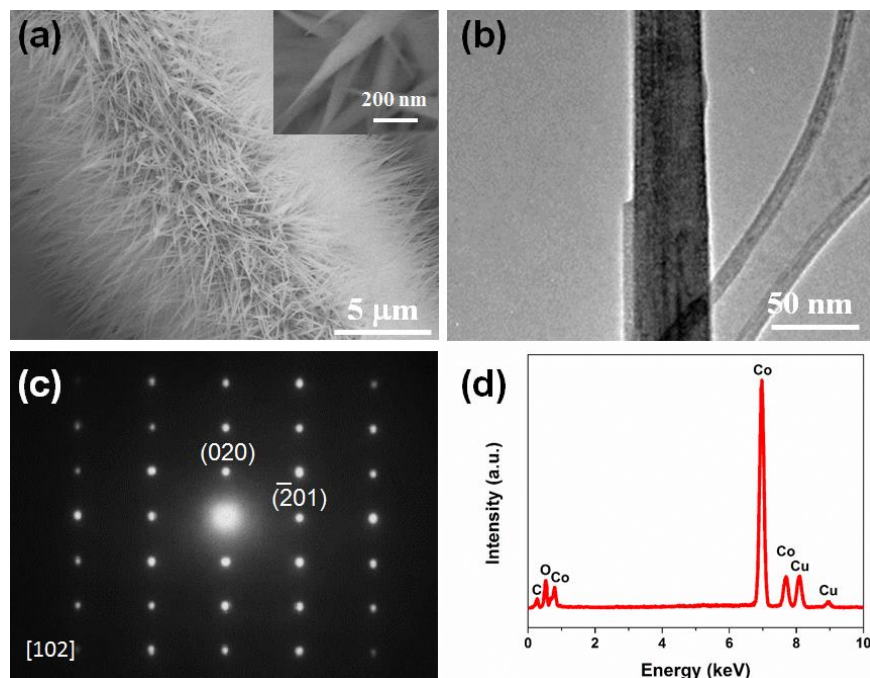


Figure 3.3. (a) Low- and (inset) high-magnification SEM images, (b) TEM image, (c) SAED pattern and (d) EDS spectrum of $\text{Co}(\text{CO}_3)_{0.5}(\text{OH})\cdot 0.11\text{H}_2\text{O}$ nanowire.

After phosphidation, the nanowire array structure kept intact, as shown in Figure 3.4a. The inset, enlarged from nanowire tips, shows sharp tips of CoP nanowires with the width of 50 to 100 nm. In contrast to $\text{Co}(\text{CO}_3)_{0.5}(\text{OH})\cdot 0.11\text{H}_2\text{O}$ nanowire, CoP nanowire shows a rough surface (Figure 3.4b). Correspondingly, the diffraction rings in Figure 3.4c reveals that CoP nanowire presents a polycrystalline feature with indexed diffraction rings of (011), (111), (112), (211), (202), and (301) planes of the orthorhombic CoP phase ($a = 5.077 \text{ \AA}$, $b = 3.281 \text{ \AA}$, $c = 5.587 \text{ \AA}$), which could be caused by the dehydration and gas release of the $\text{Co}(\text{CO}_3)_{0.5}(\text{OH})\cdot 0.11\text{H}_2\text{O}$ nanowire in the phosphidation process.²¹³ The inset HRTEM lattice image in Figure 3.4b shows the lattice fringes with an interplane spacing of 0.247 nm, repressing the (111) planes of CoP. In addition, the EDS spectrum shown in Figure 3.4d confirm the successful introduction of P element after phosphidation. Figure 3.4e shows the high-angle annular dark field scanning TEM (HAADF

STEM) image and the corresponding EDS elemental mappings (P, O, Co, and P + O) of a single CoP nanowire, further confirming the homogeneous distribution of P and Co elements along the nanowire. The combined mapping image of P and O elements (Figure 3.4e(v)) reveals a thin layer of oxygen on the surface of the CoP nanowire, indicating a formation of a thin oxidation surface layer. Furthermore, a low-loss electron energy loss spectrum (EELS) mapping (Figure 3.4f,g) using an energy range of 6.0-7.0 eV (Figure 3.4h) indicates the occurrence of Co^{2+} on the surface. The Co^{2+} can be assigned to the interband transition of the extended O 2p states to the conduction band (O 2p to Co 3d (eg)) in cobalt oxide,²¹⁴ which confirmed that the cobalt oxide layer with a thickness of about 8 nm was formed and concentrated on the surface of the CoP nanowire. The formation of the surface oxidation layer is caused by the reaction of CoP and O_2 in ambient air due to the metallic nature of CoP.^{215,216}

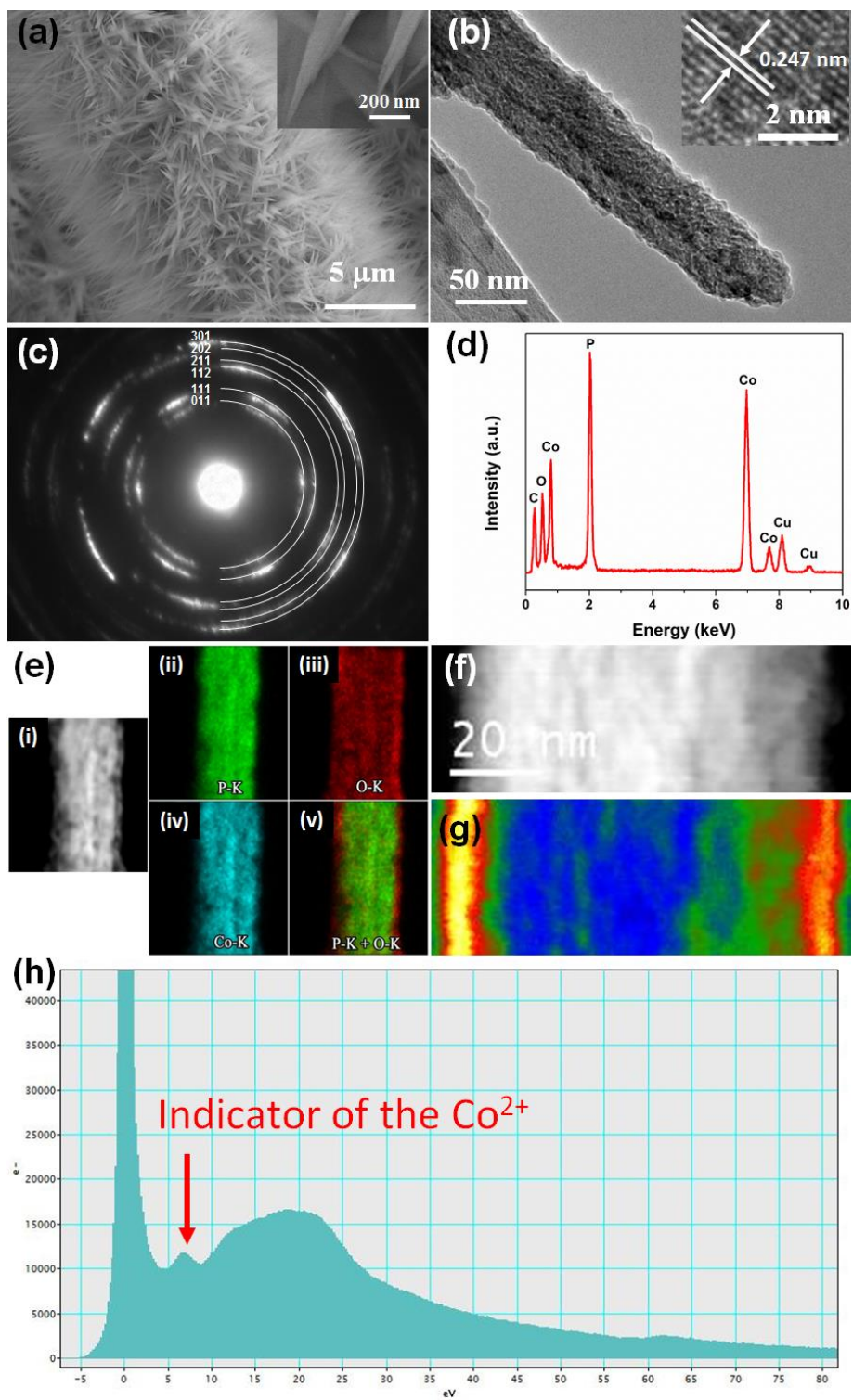


Figure 3.4. (a) FESEM images of CoP nanowire arrays. (b) TEM image of a single CoP nanowire and the inset showing the HRTEM lattice image of the (111) plane. (c) Indexed SAED pattern of

the CoP nanowire. (d) EDS spectrum of CoP nanowire. (e) HAADF-STEM and corresponding EDS elemental maps imaged by P, O, Co, and P + O. (f, g) HAADF-STEM image and corresponding EELS maps using the energy range of 6.0-7.0 eV for CoP nanowire, respectively. (h) EELS spectra from the CoP nanowire.

In the controlled experiment, the $\text{Co}(\text{CO}_3)_{0.5}(\text{OH})\cdot 0.11\text{H}_2\text{O}$ precursor was annealed in the air to order to get cobalt oxide nanowire arrays. The SEM image and XRD patterns are shown in Figure 3.5.

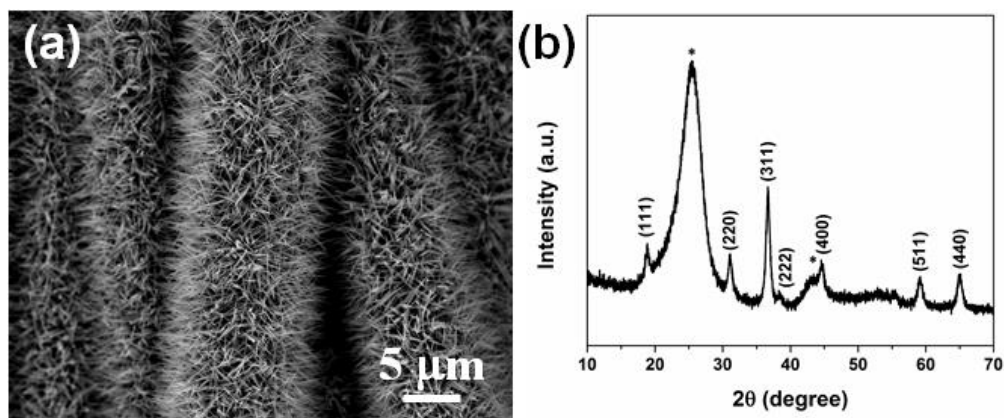


Figure 3.5. (a) SEM image and (b) XRD patterns of cobalt oxide (Co_3O_4) nanowire arrays.

On the basis of the discussion by Gogotsi and Simon,²¹⁷ the best practice performance metric for a supercapacitor should include all device components, hence arealmetric and volumetric were used instead of gravimetric to describe the performance of the present electrodes and full devices. The electrochemical properties of the CoP nanowire arrays were investigated by cyclic voltammetry (CV) and galvanostatic charge/discharge measurements in a conventional three-electrode configuration using a 1 M LiCl aqueous solution as the electrolyte. It is important to rule out the possibility of significant capacitive contribution from the carbon cloth or the cobalt oxide surface layer. We have, therefore, measured the CV curves of the CoP nanowire arrays,

cobalt oxide nanowire arrays, and blank carbon cloth after phosphidation, as shown in Figure 3.6a. Clearly, the carbon cloth shows an insignificantly small capacitance compared to that of the CoP electrode. In addition, the capacitance of the cobalt oxide electrode was more than 1 order lower than that of the CoP electrode with the same loading amount. It was reported that the ions from the electrolyte can be easily transported through the electronically insulating layers with a thickness of a few nanometers. Hence, given the fact that the cobalt oxide layer on the CoP nanowire surface is negligibly thin, about 8 nm, it is reasonable to conclude that the capacitance is primarily contributed from the CoP itself. Figure 3.6b shows the CV curves of the CoP nanowire array electrode at different scan rates from 10 to 100 mV/s. A potential of -0.8 V was applied on the CoP nanowire array electrode to match the operation window of the positive electrode in ASC, to be discussed in further detail. The symmetrical quasi-rectangular shape of the CV curves reveals the typical supercapacitor characteristic of the CoP nanowire array electrode. However, at high scan rates, the CV curves show larger polarization, which may be caused by the incomplete desolvation process of the Li^+ ions.²¹⁸ Figure 3.6c illustrates the charge/discharge curves at different current densities of 1, 2, 5, and 10 A/cm^2 . The good symmetry of the charge/discharge curves demonstrated the ideal capacitive behavior of the CoP nanowire array electrode. As shown in Figure 3.6d, the areal capacitance of the CoP nanowire array electrode was calculated as 571.3, 482.3, 402.2, and 333.5 mF/cm^2 at current densities of 1, 2, 5, and 10 mA/cm^2 , respectively, which are higher than most of the recently reported as-synthesized negative electrode materials, such as CoSe_2 (332 mF/cm^2 at 1 mA/cm^2),²¹⁹ Fe_2O_3 (180.4 mF/cm^2 at 1 mA/cm^2),¹⁹³ and Mn_3O_4 (372.5 mF/cm^2 at 1 mA/cm^2).²²⁰ The rate capacity was 58.3% when the current density increased from 1 mA/cm^2 to 10 mA/cm^2 . The excellent electrochemical performance of the CoP nanowire arrays can be attributed to three main aspects. First, the superior electrical conductivity of CoP facilitated

electron transfer within the electrode. Second, the 3D configuration of the CoP nanowire arrays offered a large surface area and short ionic and electronic paths. Third, direct growth of the CoP nanowire arrays on the carbon cloth provided robust mechanical adhesion and good electrical contact.^{13,50}

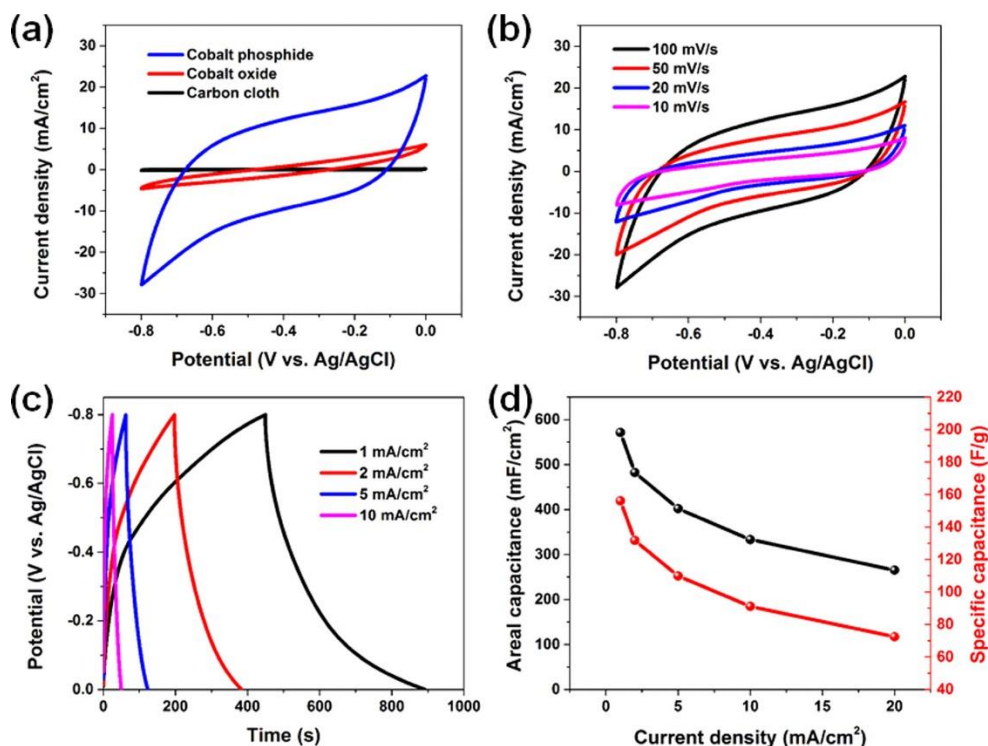


Figure 3.6. (a) CV curves of CoP, cobalt oxide, and blank carbon cloth after phosphidation at a scan rate of 100 mV/s. (b) CV curves of the CoP nanowire array electrode at different scan rates. (c) Galvanostatic charge/discharge curves of the CoP nanowire array electrode at different current densities. (d) Areal and specific capacitance of the CoP nanowire array electrode as a function of current density.

It should be noted that the CoP nanowire array electrode suffered poor stability in the aqueous electrolyte (Figure 3.7a). The EIS was performed to study the electrical conductivity before and after the cycling test. Two typical Nyquist plots of the CoP nanowire array electrode

before and after the cycling test are shown in Figure 3.7b. The measured impedance spectra are fitted by an equivalent circuit (Figure 3.7c), which consists of an equivalent series resistance R_S , a charge transfer resistance R_{CT} , a pseudocapacitive C_L from the redox process of CoP, a constant phase element (CPE) of the double layer capacitance and a leakage resistance R_L .⁹⁶ The impedance plots are composed of a semicircle arc in the high-frequency region followed by a linear response in the low frequency. The high-frequency region corresponds to the equivalent series resistance, which combines resistances of ionic resistance of the electrolyte, intrinsic resistance of the substrate, and contact resistance at the active material/current collector interface. The linear part in the low-frequency region is related to the frequency dependence charge transfer resistance. As shown in Figure 3.7d, the equivalent series resistance, R_S , was 2.337 Ω and remained constant during the cycling process, suggesting the high conductivity of the CoP nanowire arrays, as well as the good electric contact between the CoP nanowire arrays and the carbon cloth substrate. Contrastingly, the charge transfer resistance, R_{CT} , increased significantly from 5.163 to 30.9 Ω after 5000 cycles, which cause the stability reduction.

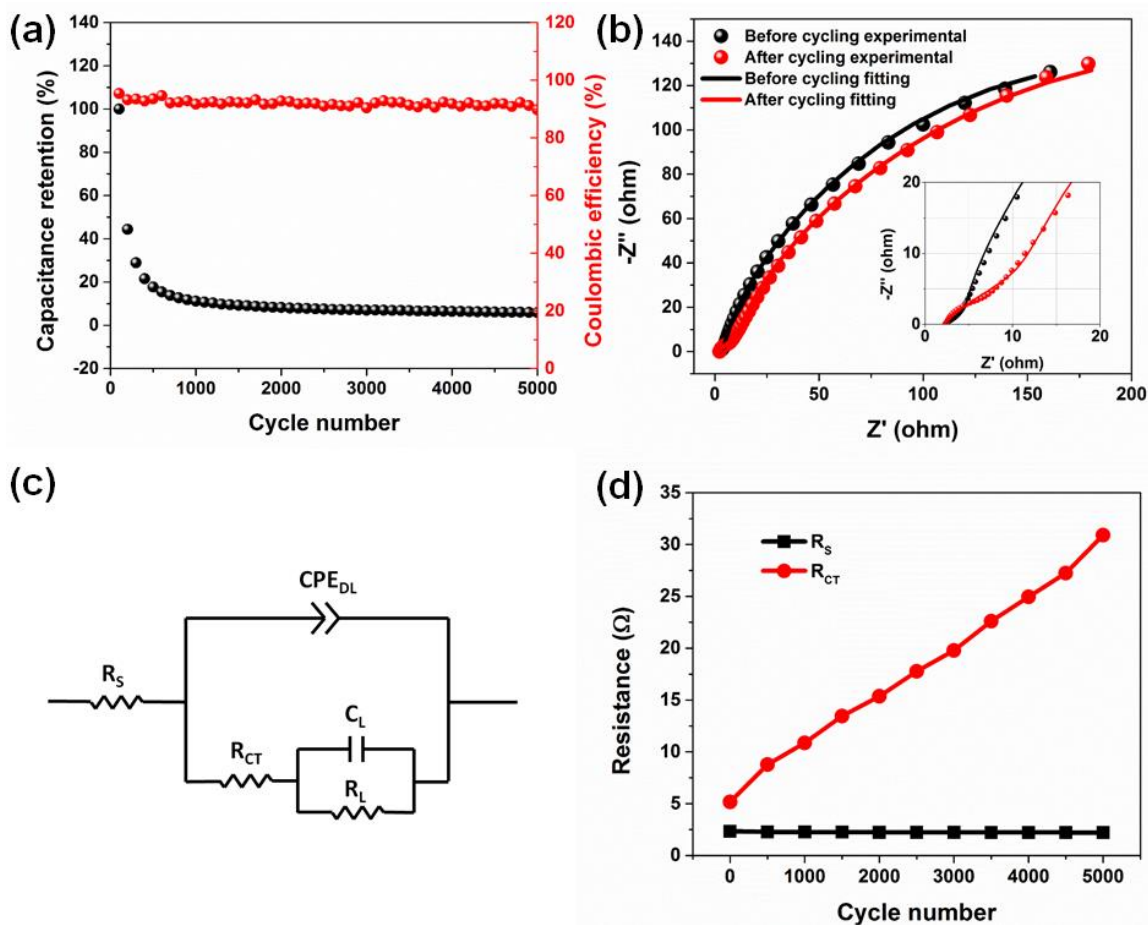
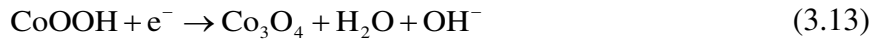
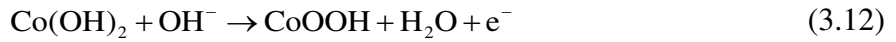


Figure 3.7. (a) Cycle performance of the CoP nanowire array electrode in 1 M LiCl aqueous electrolyte at a scan rate of 5 mA/cm² for 5000 cycles. (b) Nyquist plots of the CoP electrode collected before and after the cycling test. The inset is the high-frequency part of the Nyquist plot. (c) The equivalent circuit of CoP nanowire arrays electrode. (d) Plots of the equivalent series resistance R_S and the charge transfer resistance R_{CT} as a function of cycle number.

One possible reason causes the instability is the structure deformation. However, from Figure 3.8a, the SEM image of CoP nanowire arrays after cycling test, it is clear the nanostructure was well maintained. Another possible mechanism is the irreversible electrochemical oxidation reaction during the cycling process. XPS was used to investigate the chemical composition before and after the cycling test in an aqueous electrolyte to examine the conductivity change of the CoP

nanowire arrays. The XPS survey of the CoP nanowire arrays (Figure 3.8b) confirms the presence of Co and P elements. The high-resolution core level of Co 2p (Figure 3.8c) before the cycling test showed peaks at 779.05 (2p3/2) and 794 (2p1/2) eV corresponding to the binding energies of Co 2p in CoP. All of the other peaks, including 782.2 and 798.4 eV and the two satellite peaks at 786.4 and 803.6 eV, are associated with cobalt oxide,²²¹ which further confirm the formation of the surface oxidation layer on the as-synthesized CoP nanowire. Two peaks appearing in the P(2p) region (Figure 3.8d) were assigned to phosphide at 130 eV and orthophosphate (Co₃(PO₄)₂) at 134.2 eV, respectively.²²² After 5000 cycles, the Co 2p peaks in CoP fully disappeared (Figure 3.8c), and the phosphide peak also decreased significantly (Figure 3.8d). Those results indicated that the surface oxidation layer on the CoP nanowire increased during the cycling process by the possible irreversible electrochemical oxidation reaction^{82,223,224} as follows:



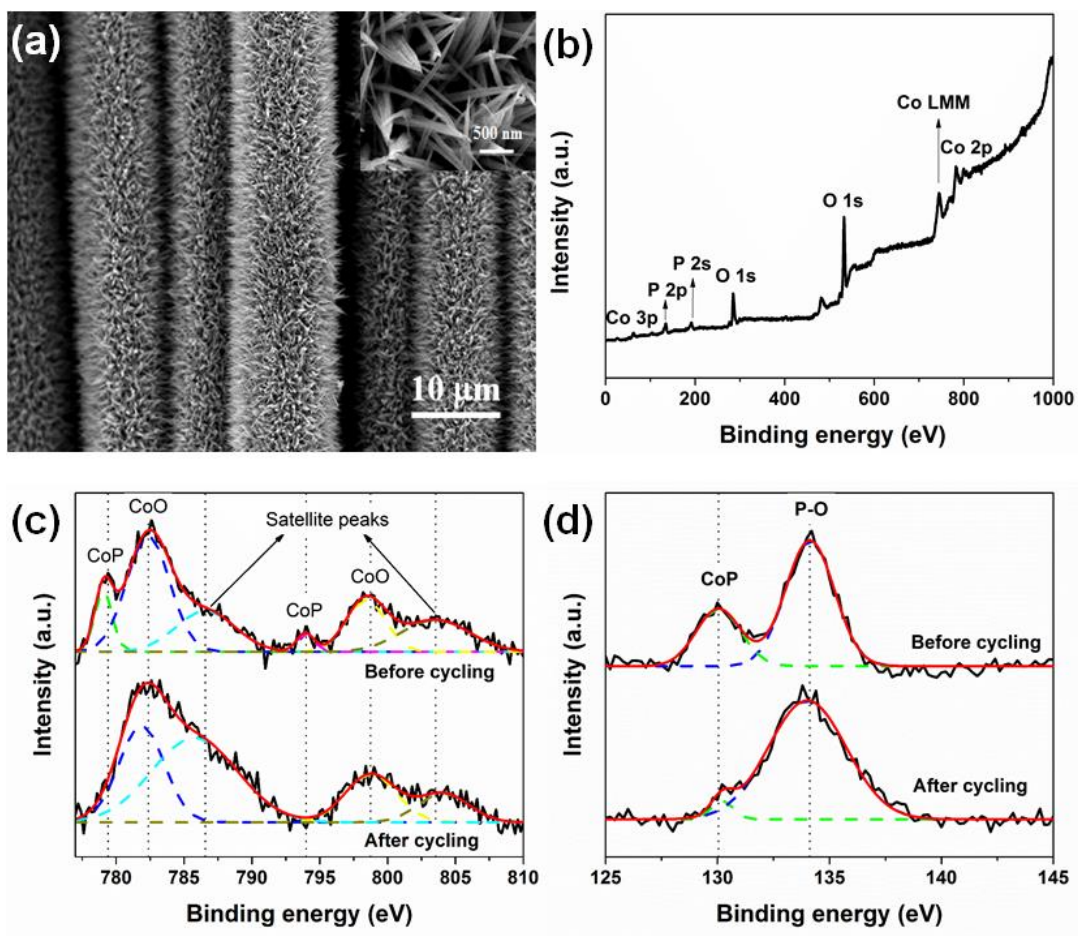


Figure 3.8. (a) SEM image of CoP nanowire arrays electrode after 5000 charge/discharge cycles at a scan rate of 5 mA/cm^2 . Insert shows the tips of nanowires. (b) XPS survey of CoP nanowire arrays. High-resolution core level of (c) Co 2p and (d) P 2p XPS spectra of the CoP nanowire arrays before and after the cycling test.

The increment of the surface cobalt oxide may prevent ions from penetrating into the CoP core in the nanowire,²²⁵ thus causing the reduction of capacitance. A similar diminishment of capacitance was observed in Ni_2P ascribed to the formation of $\text{Ni}(\text{OH})_2$.¹⁴⁸ On the basis of those results, it is believed that the irreversible electrochemical oxidation reaction of the CoP nanowire played a crucial role in the instability of the CoP nanowire array electrode. Nevertheless, the

irreversible oxidation reaction can be well suppressed by replacing the aqueous electrolyte with the solid-state gel electrolyte.^{226–228} In addition, solid-state supercapacitors offer numerous advantages, such as flexibility, lightweight, and environmental friendliness, in comparison to liquid-based supercapacitors and, hence, are appropriate to meet the urgent energy demand.^{13,229}

To examine the practical application of CoP nanowire arrays as flexible solid-state supercapacitor electrodes, a SSC was fabricated using the PVA/LiCl gel electrolyte (Figure 3.9a). The CV curves in the voltage range from -0.8 to 0.8 V at different scan rates are shown in Figure 3.9b. As shown in Figure 3.9c, the charge/discharge curves of the SSC showed good symmetry with a small IR drop of less than 0.05 V, revealing the good redox reaction reversibility. The calculated specific capacitances as a function of current density are plotted in Figure 3.9d. The capacitance value of the SSC was calculated as 35.4 and 22.65 mF/cm^2 at a current density of 1 and 10 mA/cm^2 , respectively, showing a good rate capability of 63.4% . Most importantly, as shown in Figure 3.9e, the SSC presented great stability with 87.05% capacitance retention after 5000 charge/discharge cycles, which demonstrated that the CoP nanowire arrays have great potential as highly stable negative electrodes for solid-state supercapacitors.

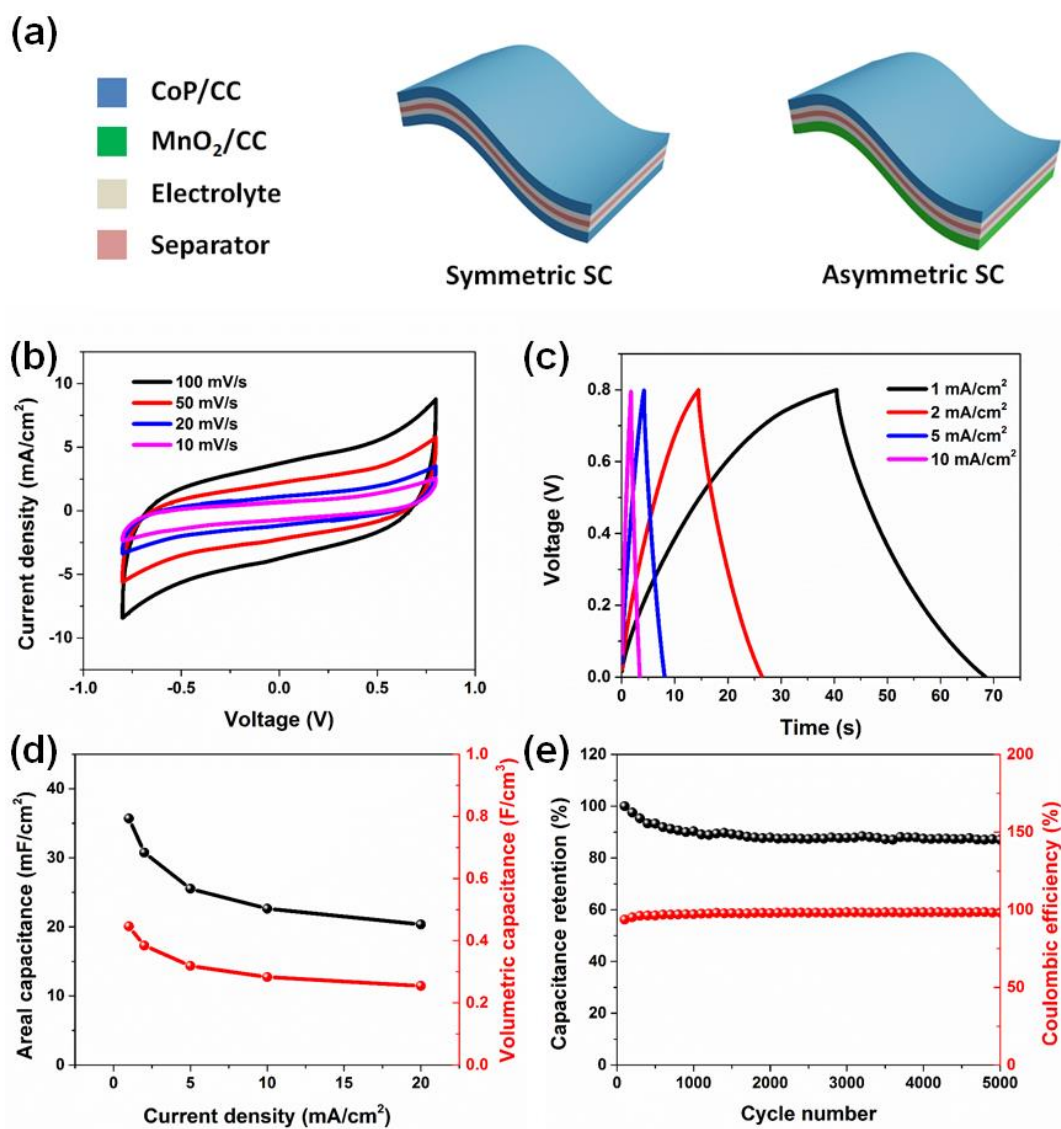


Figure 3.9. (a) Schematics the designed symmetric and asymmetric supercapacitors. (b) CV curves of the SSC at different scan rates. (c) Galvanostatic charge/discharge curves of the SSC at different current densities. (d) Areal and volumetric capacitance of the SSC as a function of current density. (e) Cycle performance of the SSC at a scan rate of 5 mA/cm² for 5000 cycles.

To further improve the energy density, an ASC was fabricated consisting of CoP nanowire arrays as the negative electrode and the MnO₂ nanowire array positive electrode (Figure 3.9a). The MnO₂ nanowire arrays were grown on the carbon cloth by a hydrothermal approach¹⁹³ and

characterized by XRD, FESEM, and TEM. The details can be found in Figure 3.10. As shown in SEM images (Figure 3.10a, b), MnO₂ nanowires were grown uniformly in carbon cloth. TEM image (Figure 3.10c) shows that the diameter of MnO₂ nanowire is around 50 nm. The lattice spacing was measured to be ~0.69 nm in HRTEM image (Figure 3.10d), corresponding to d-spacing of (110) planes of MnO₂. The energy dispersive X-ray spectrometry (EDS) spectrum in Figure 3.10e shows the existence of elements Mn, O, K, C, and Cu. Signals of C and Cu come from the TEM copper grid, and the signal of K is due to the possible K⁺ doping effect during synthesis.²³⁰ The XRD patterns are shown in Figure 3.10f, all the diffraction peaks are in good agreement with the tetragonal rutile phase (JCPDS No. 44-0141) except the peaks from the carbon cloth.

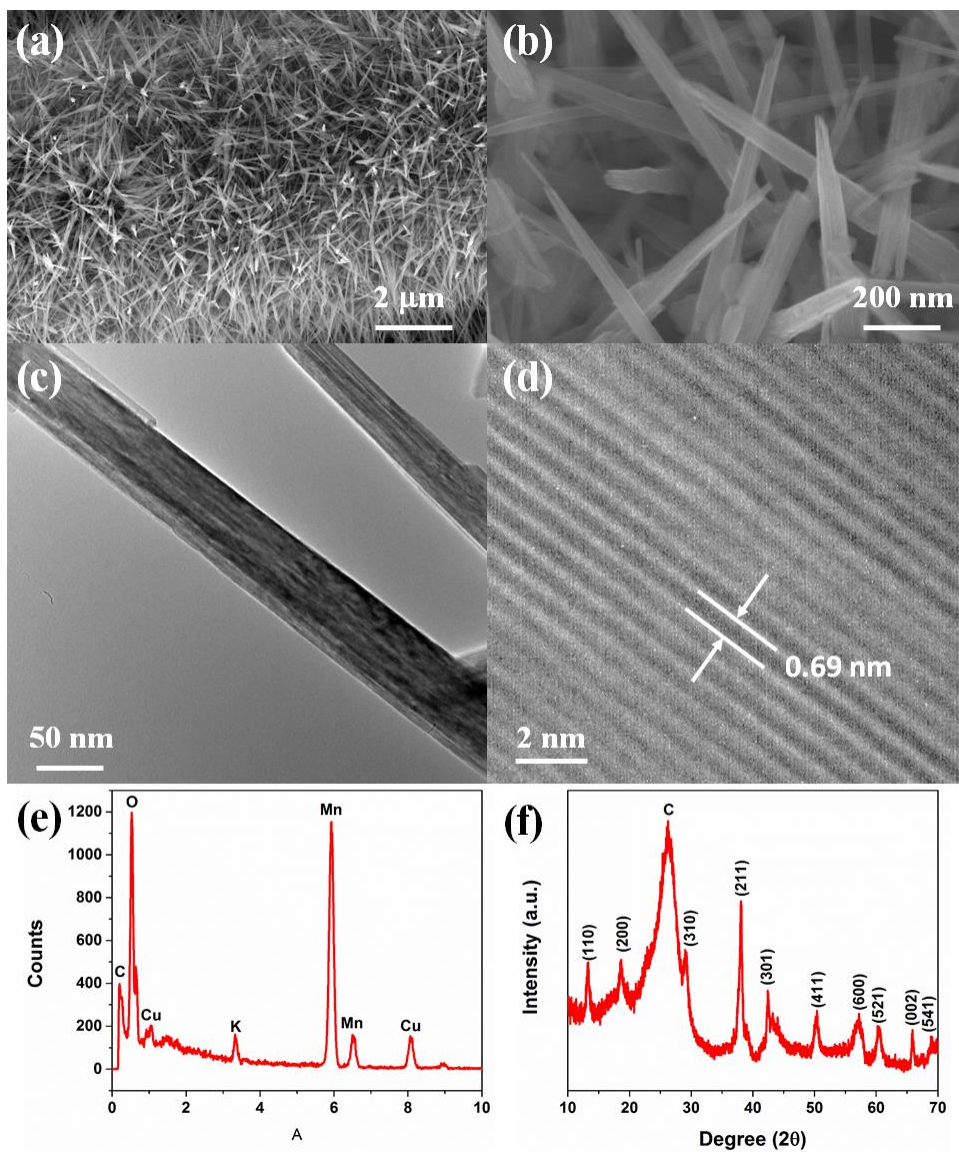


Figure 3.10. (a) Low and (b) high magnification SEM image of MnO₂ nanowire arrays. (c) TEM image of MnO₂ nanowire. (d) High-resolution TEM image of MnO₂ nanowire. (e) EDS spectra of MnO₂ nanowire. (f) XRD spectrum of MnO₂ nanowire arrays.

The electrochemical performance of the MnO₂ nanowires was also evaluated by CV and charge/discharge measurements using a three-electrode configuration with 1 M LiCl aqueous solution as the electrolyte (Figure 3.11). To maximize the performance of the ASC device, the

charge of different electrodes should be balanced according to the equation $q = C \times \Delta E \times A$. In

order to get $q_+ = q_-$, the areal balance was calculated by the equation $\frac{A_+}{A_-} = \frac{C_- \times \Delta E_-}{C_+ \times \Delta E_+}$.¹⁸⁷ The area

ratio between CoP and MnO₂ electrodes was calculated based on the charge/discharge curves to be 0.882.

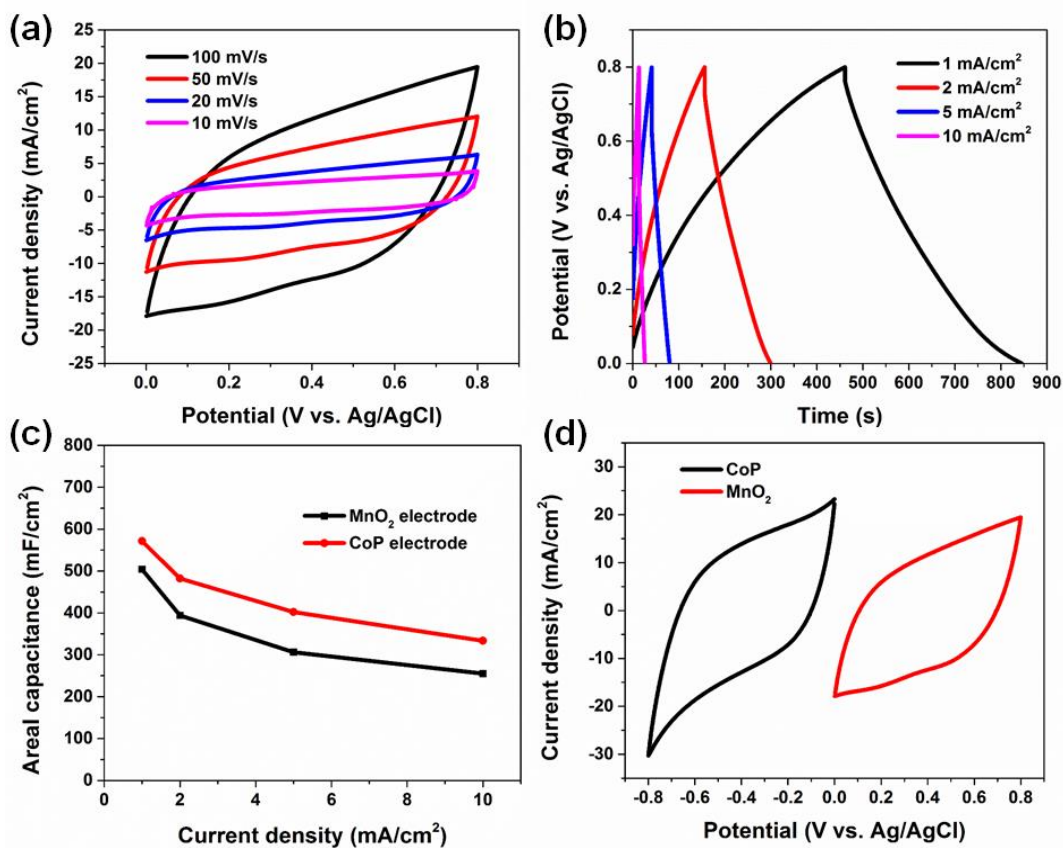


Figure 3.11. (a) CV curves of the MnO₂ electrode at different scan rates. (b) Galvanostatic charge/discharge curves of MnO₂ electrode at different current densities. (c) Areal capacitance of CoP and MnO₂ electrode as a function of current density. (d) CV curves of CoP and MnO₂ electrodes at 100 mV/s.

On the basis of the CV studies for the single electrodes, the total cell voltage can be expressed as the sum of the potential range of CoP and MnO₂ nanowire array electrodes, therefore a series of operating cell voltages from 0.8 to 1.6 V was applied to the ASC. Figure 3.12a shows the CV curves of the asymmetric device collected at 100 mV/s in different voltage windows. The ASC device demonstrated a typical supercapacitor behavior, evident by the nearly rectangular shape of all CV curves. In addition, the CV measurements were performed under different bending conditions to evaluate the feasibility of the ASC. As shown in the insert photographs of Figure 3.12b, the ASC presented high flexibility under bent and twisted conditions, and more importantly, no significant change of the CV curves was observed (Figure 3.12b), demonstrating the good flexibility and durability of the solid-state ASC. The galvanostatic charge/discharge tests at different current densities were also performed as shown in Figure 3.12c. The symmetrical charge/discharge characteristics represented good capacitive characteristics for the ASC. On the basis of the discharge curves, a volumetric capacitance of 1.94 F/cm³ at 1 mA/cm² was achieved for the ASC device, as shown in Figure 3.12d. Furthermore, the long-term stability of ASC has been investigated up to 5000 cycles, as shown in Figure 3.12e. The ASC exhibited good stability with 82% capacitance retention after 5000 charge/discharge cycles, as well as excellent Coulombic efficiency (>90%).

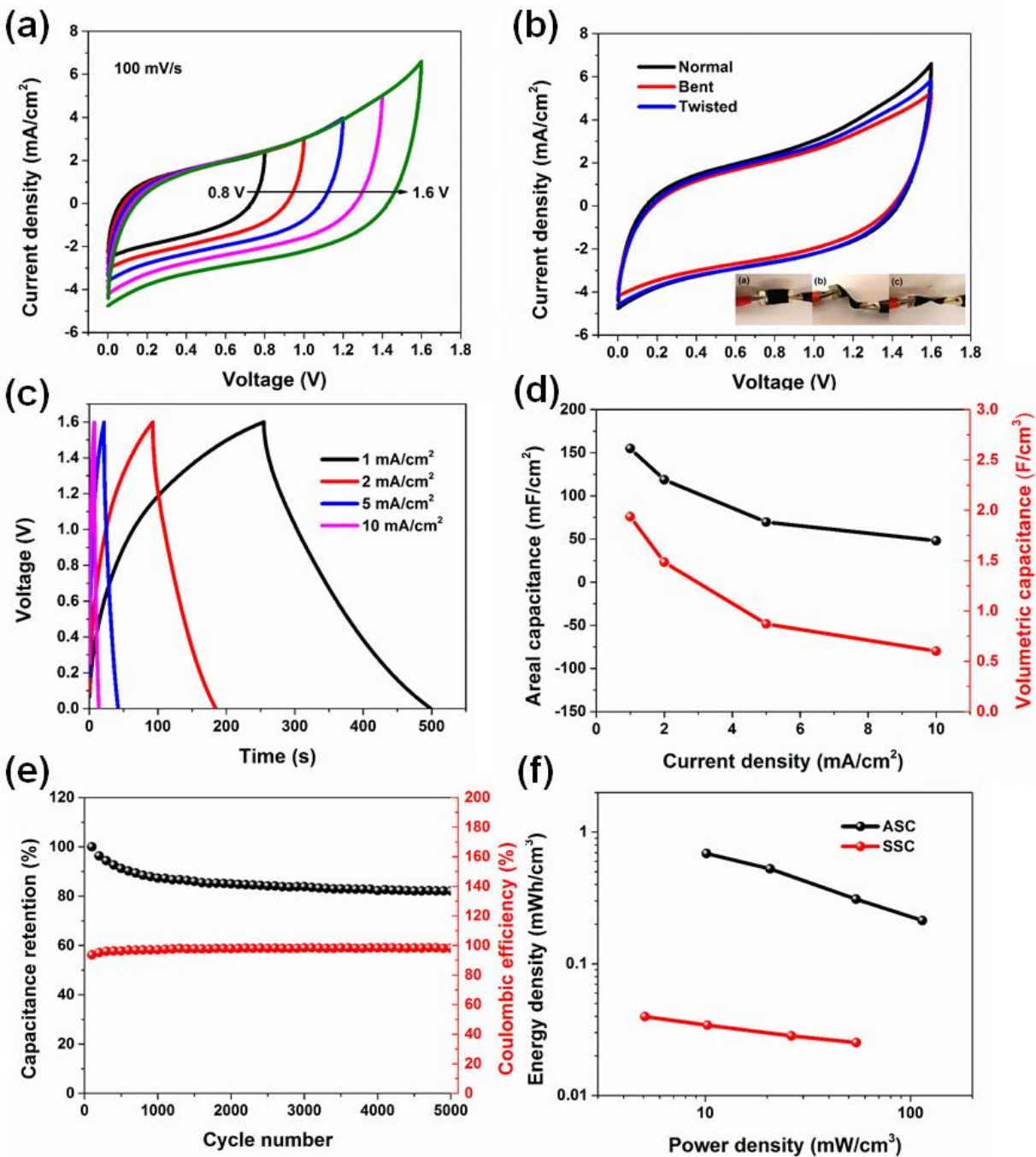


Figure 3.12. (a) CV curves of the ASC device collected in different scan voltage windows. (b) CV curves obtained at a scan rate of 100 mV/s under normal, bent, and twisted conditions. Insert are the photographs of the ASC device. (c) Galvanostatic charge/discharge curves of the ASC at different current densities. (d) Areal and volumetric capacitance of the ASC as a function of current

density. (e) Cycle performance of the ASC at a scan rate of 5 mA/cm² for 5000 cycles. (f) Ragone plots of the ASC and SSC devices.

The Ragone plots are also presented in Figure 3.12f to evaluate the average power density and energy density of both SSC and ASC. Compared to that of SSC, the ASC device showed a high energy density of 0.69 mWh/cm³ at a power density of 10.15 mW/cm³, which is higher than the recently reported values of flexible ASCs, as shown in Table 3.1.^{85,86,121,193,219,220,231,232} Moreover, the energy density can be well maintained at 0.21 mWh/cm³ at a high power density of 114.20 mW/cm³.

Table 3.1. Comparison of capacitive performances of reported negative electrode materials and their corresponding ASCs.

Negative electrode material	Areal capacitance	ASC device	Volumetric capacitance (mF/cm ³)	Energy density (mWh/cm ³)	Power density (mW/cm ³)	Cycling performance
CoP (Present work)	571.3 mF/cm ² at 1 mA/cm ²	MnO ₂ //CoP	1.94 F/cm ³ at 1 mA/cm ²	0.69	114.20	82.15% after 5000 cycles
Fe₂O₃ ¹⁹³	180.4 mF/cm ² at 1 mA/cm ²	MnO ₂ //Fe ₂ O ₃	1.5 F/cm ³ at 2 mA/cm ²	0.55	139.1	84% after 5000 cycles
Oxygen-deficient Fe₂O₃ ⁸⁵	382.7 mF/cm ² at 0.5 mA/cm ²	MnO ₂ //Fe ₂ O ₃	1.21 F/cm ³ at 0.5 mA/cm ²	0.41	100	81.6% after 6000 cycles
α-Fe₂O₃@PANI ⁸⁶	103 mF/cm ² at 0.86 mA/cm ²	PANI// α -Fe ₂ O ₃ @PANI	2.02 F/cm ³ at 5 mV/s	0.35	120.51	95.77% after 10000 cycles
CoSe₂ ²¹⁹	332 mF/cm ² at 1 mA/cm ²	MnO ₂ //CoSe ₂	1.77 F/cm ³ at 1 mA/cm ²	0.588	282	94.8% after 2000 cycles
Mn₃O₄ ²²⁰	372.5 mF/cm ² at 1 mA/cm ²	Ni(OH) ₂ // Mn ₃ O ₄	2.07 F/cm ³ at 1 mA/cm ²	0.35	32.5	83.3% after 12000 cycles
RGO ¹²¹	–	H-MnO ₂ //RGO	0.72 F/cm ³ at 10 mV/s	0.25	1430	95.5% after 5000 cycles
RGO ²³¹	250 mF/cm ² at 10 mV/s	MnO ₂ /ZnO//RGO	0.52 F/cm ³ at 10 mV/s	0.234	133	98.4% after 5000 cycles
H-TiO₂@C ²³²	–	H-TiO ₂ @MnO ₂ //H-TiO ₂ @C	0.71 F/cm ³ at 10 mV/s	0.3	230	91.2% after 5000 cycles

3.3. CoP Nanosheet Arrays

3.3.1. Experiments

To synthesize CoP nanosheet arrays, 0.44 g Co(NO₃)₂·6H₂O and 0.11 g hexamethylenetetramine (HMTA) were dissolved in 15 mL water and kept in autoclave with

carbon cloth at 100°C for 6 h.²³³ The phosphidation process was the same as CoP nanowire arrays. The samples were further sulfidated by heating the sample and sulfur powder under Ar atmosphere. The loading amount of CoP nanosheet arrays was determined as 1.33 mg/cm². The material characterization and electrochemical measurement methods are the same as described in section 3.2.1.

3.3.2. Results and Discussion

By changing the additives to HMTA during the synthesis, nanosheet arrays precursor can be grown on carbon cloth (Figure 3.13a). The reactions involved in the hydrothermal synthesis of Co(OH)₂ can be illustrated as follows.²³⁴



Figure 3.13b shows the XRD patterns of the nanosheet arrays sample before and after phosphidation. Besides the peaks from the carbon cloth substrate, all the diffraction peaks before phosphidation correspond to α -Co(OH)₂ phase (JCPDS No. 74-1057), the diffraction peaks after phosphidation can be indexed as orthorhombic CoP phase. Figure 3.13c presents the FESEM image of Co(OH)₂ nanosheet arrays, indicating a large area of vertically aligned nanosheets, uniformly distributed over the carbon cloth. As shown in Figure 3.13d, the nanosheet arrays format was kept intact after phosphidation.

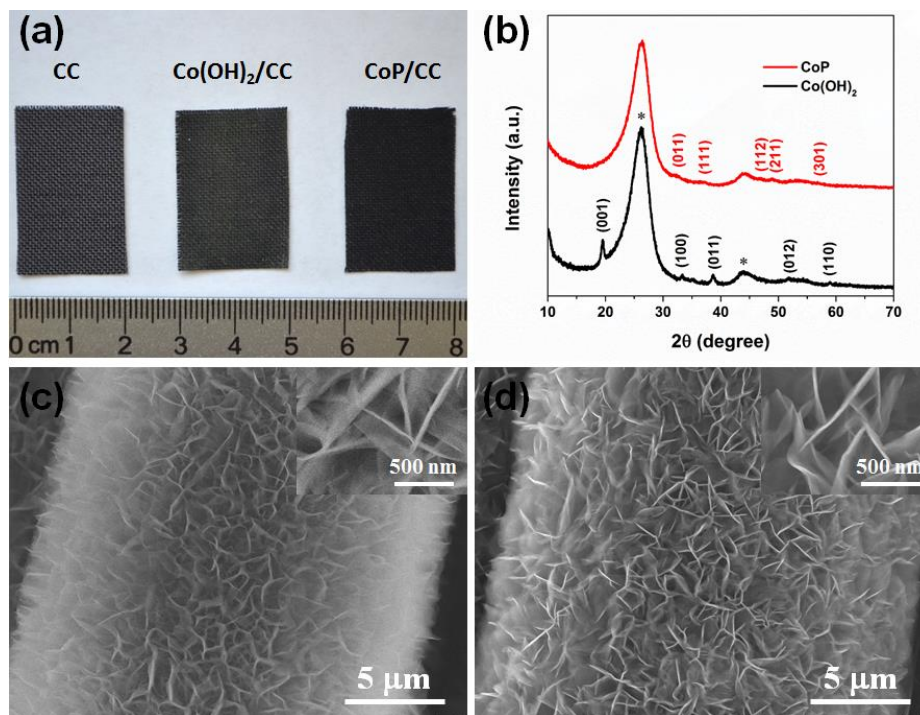


Figure 3.13. (a) Photograph (from left to right) of blank carbon cloth, Co(OH)₂ and CoP nanosheet arrays on carbon cloth. (b) XRD patterns of Co(OH)₂ and CoP nanosheet arrays on carbon cloth. Low- and (inset) high-magnification SEM images of (c) Co(OH)₂ nanosheet arrays and (d) CoP nanosheet arrays on carbon cloth.

The TEM images of Co(OH)₂ (Figure 3.14a) further confirmed the nanosheet morphology. The selected area electron diffraction pattern of Figure 3.14b reveals the single crystal feature of Co(OH)₂ nanosheet, and can be indexed as α -Co(OH)₂ phase from [001] zone axis. The EDS spectrum confirms the Co(OH)₂ nanosheet consists of Co and O elements (Figure 3.14c).

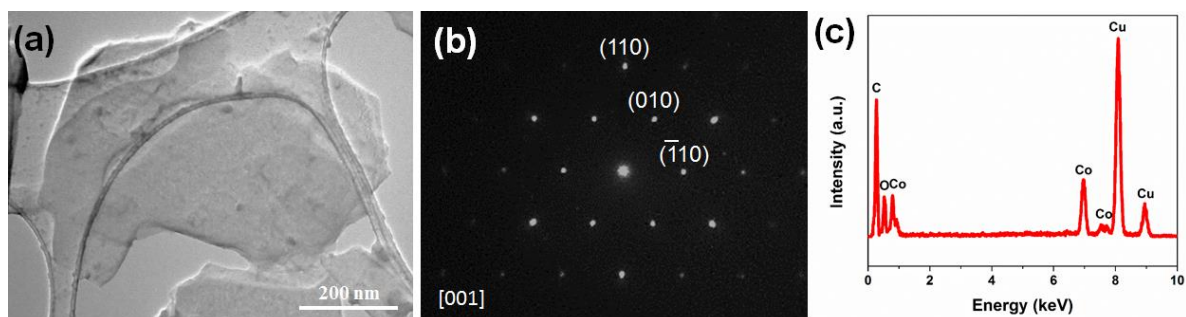


Figure 3.14. (a) TEM images, (b) Selected area electron diffraction patterns and (c) EDS spectra of and Co(OH)_2 nanosheet.

After phosphidation, the nanosheet is being reconstructed with much finer and pores (Figure 3.15a). Similar to CoP nanowire, the single crystalline Co(OH)_2 precursor transferred to the polycrystalline CoP (Figure 3.15b) after the phosphidation process. The EDS spectra as shown in Figure 3.15c further confirmed the P element in CoP nanosheet. A high-resolution electron microscopy image (Figure 3.15d) of the nanosheet also shows the features of polycrystalline nanocrystals, where the (111) and (200) lattice fringes can be clearly observed. EDS and EELS mappings were performed in the nanosheet, revealing the coexistence of cobalt, phosphorus, and oxygen in the nanosheet, as shown in Figure 3.15e and Figure 3.15g, which also confirmed the partial oxidation of CoP nanosheet.

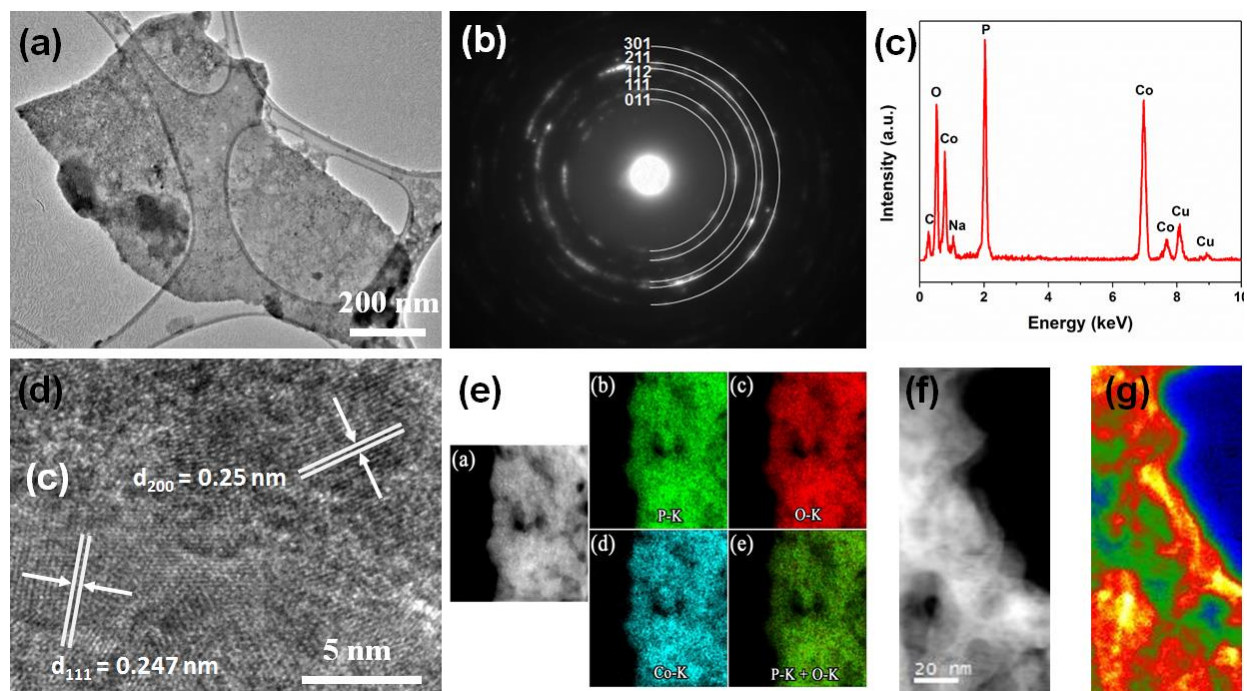


Figure 3.15. (a) TEM image, (b) selected area electron diffraction patterns, (c) EDS spectra, (d) HRTEM image, (e) HAADF-STEM and corresponding EDS elemental mapping images of P, O, Co and P+O, (f) dark field image and (g) EELS mapping on energy range 6.0-7.0 eV of CoP nanosheet.

The CV and galvanostatic curves of CoP nanosheet arrays electrode were similar to that of CoP nanowire arrays electrode, as shown in Figure 3.16a and b, showing good supercapacitive behavior as well. The areal capacitance of nanosheet arrays (Figure 3.16c) is relatively lower than that of nanowire arrays probably due to the lower loading mass (1.33 mg/cm^2 compared to 3.66 mg/cm^2). Nevertheless, the equivalent series resistance of CoP nanosheet arrays electrodes calculated from the Nyquist plots (Figure 3.16d) was only $3.412 \ \Omega$, suggesting the good conductivity. The improvement of capacitance may be raised from the enhancement of increment of the active sites for redox reactions

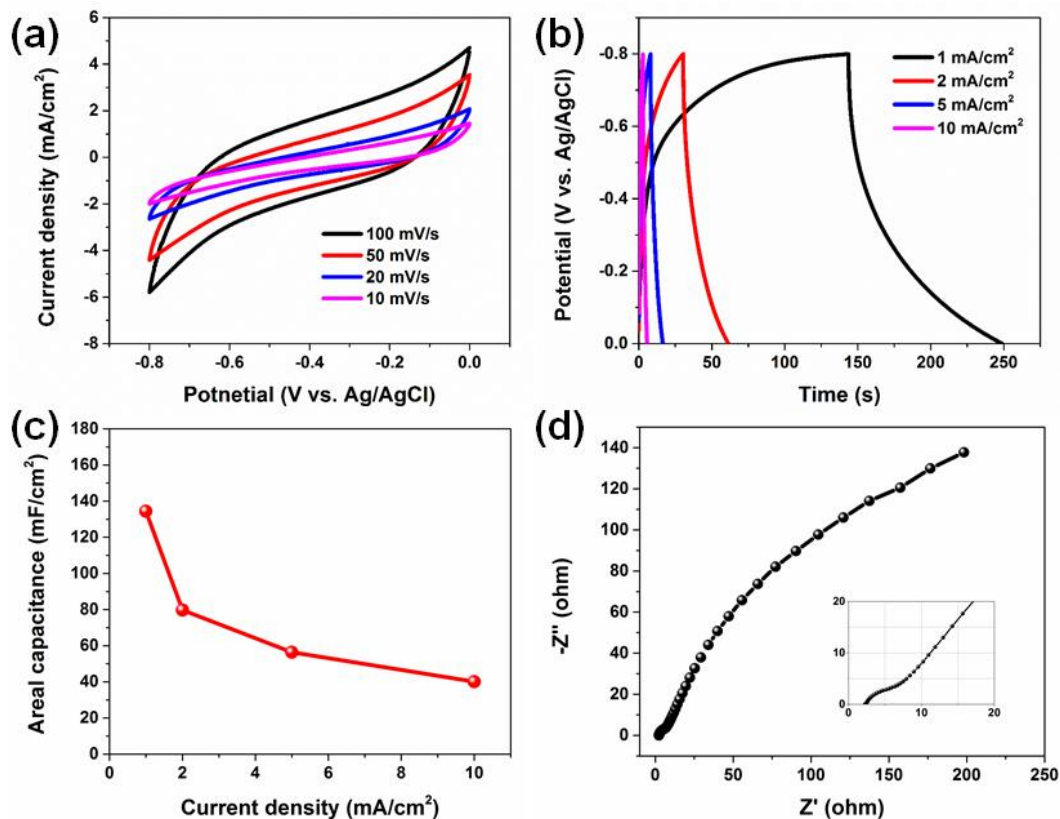


Figure 3.16. (a) CV curves of the CoP nanosheet arrays electrode at different scan rates. (b) Galvanostatic charge/discharge curves of CoP nanosheet arrays electrode at different current densities. (c) Areal capacitance of CoP nanosheet arrays electrodes as a function of current density. (f) Nyquist plots of CoP nanosheet arrays electrodes.

The supercapacitance performance of CoP nanosheet arrays can be further improved by successive sulfidation. Figure 3.17a shows the CV curves of sulfidated CoP (denoted as CoPS) and as-synthesized CoP. Clearly, the CoPS electrode exhibits higher current density, thus better capacitive behavior in comparison with those of the CoP electrodes. Figure 3.17b shows the calculated areal capacitances of the CoPS and CoP electrodes as a function of scan rate. Notably, the CoPS electrode yields an areal capacitance of 156 F/cm² at 10 mV/s, which is much larger than 29 F/cm² for the CoP electrode at the same scan rate.

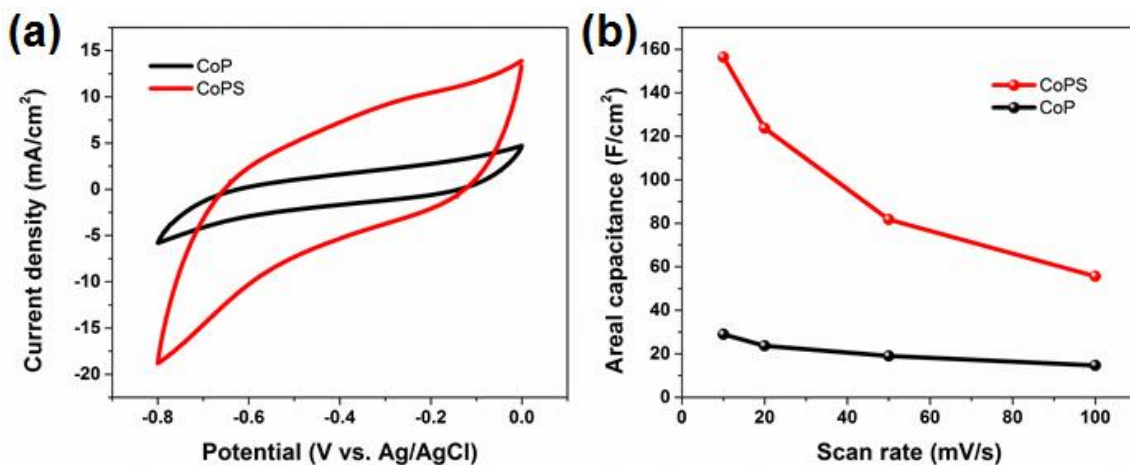


Figure 3.17. (a) CV curves of the CoPS and CoP electrodes at 100 mV/s. b) Areal capacitances of the CoPS and CoP electrodes as-a function of scan rate.

Additionally, the annealing temperature is crucial in sulfidation process. Figure 3.18 compares the CV curve of CoP nanosheet electrode under different sulfidation temperature from 200 to 350°C. Significantly, it was found that 300°C sulfidation temperature can result in largest areal capacitance for the CoPS electrode. Further increase of the temperature results in the decrease of capacitance.

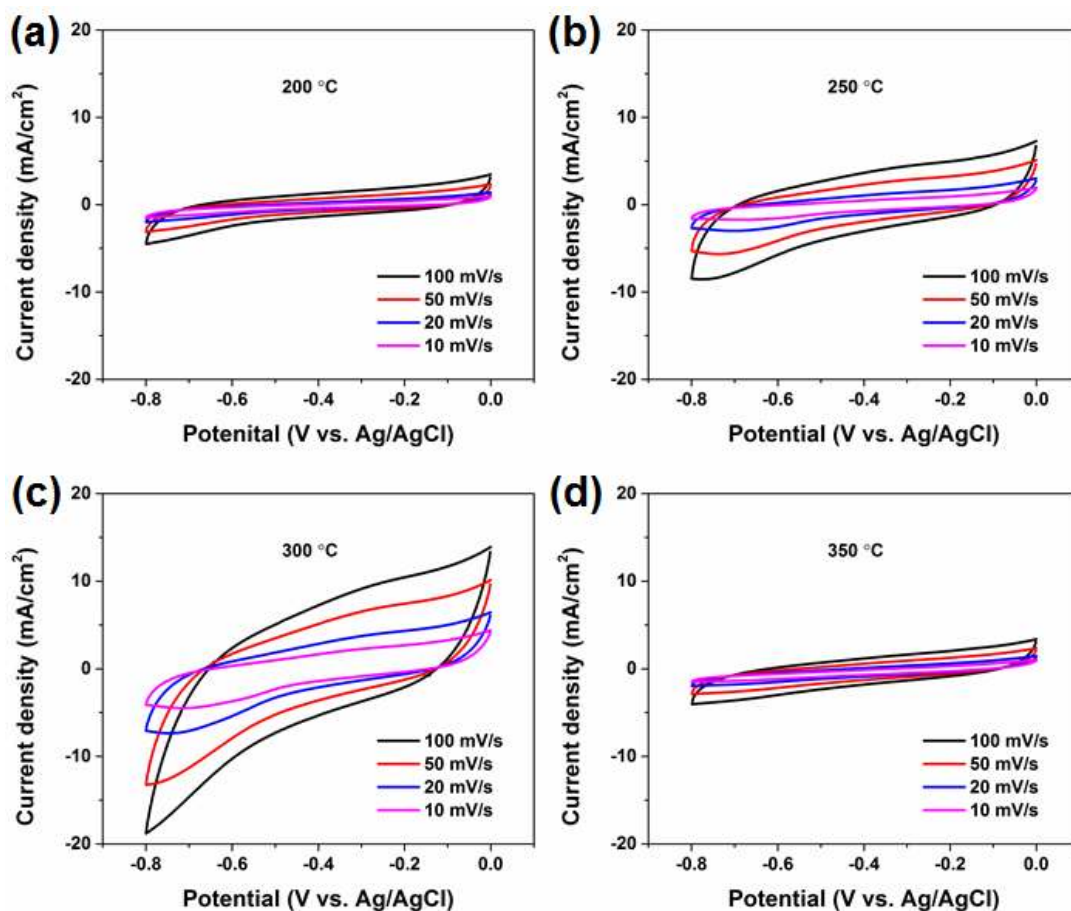


Figure 3.18. CV curves of CoP nanosheet electrode under different sulfidation temperature. (a) 200°C, (b) 250°C, (c) 300°C, and (d) 350°C.

3.4. Conclusion

In summary, we have successfully synthesized 3D CoP nanowire and nanowire arrays on a carbon cloth. The detailed characterizations revealed the transformation of the single crystal $\text{Co}(\text{CO}_3)_{0.5}(\text{OH})\cdot 0.11\text{H}_2\text{O}$ nanowire or $\text{Co}(\text{OH})_2$ nanosheet to the polycrystalline CoP nanowire and nanosheet with a negligibly thin oxidation layer on the surface. As a binder-free supercapacitor negative electrode, the as-synthesized CoP nanowire arrays demonstrated high areal capacitance and good rate capabilities. The solid-state flexible ASC based on the CoP nanowire array negative

electrode and MnO₂ nanowire array positive electrode exhibited a high volumetric capacitance of 1.94 F/cm³, an energy density of 0.69 mWh/cm³, and a power density of 114.20 mW/cm³, in addition to excellent durability in a large potential window of up to 1.6 V. Moreover, the solid-state ASC showed a significantly improved cycle stability with retention of more than 80% after 5000 cycles. The CoP nanosheet arrays show a relative lower areal capacitance than CoP nanowire arrays owing to the lower mass loading, yet its performance can be significantly improved by sulfidation.

Chapter 4 PEDOT Coated Iron Phosphide Nanorod Arrays as High-Performance Supercapacitor Negative Electrodes

4.1. Introduction

Among various negative electrode materials, iron-based materials, such as Fe_2O_3 ,^{193,235} Fe_3O_4 ,²³⁶ and FeOOH ,²³⁷ have recently attracted increasing attraction due to the various oxidation states, low cost, earth abundance, and non-toxicity.^{111–113,238} However, the poor electrical conductivity remains the key challenge for iron-based material.¹¹¹ In order to address this issue, numerous efforts have been devoted in designing nanostructured iron-based materials, which provide short ion/electron diffusion path and high surface active area. On the other hand, metal phosphides are reported as one of the promising candidates for supercapacitor electrode materials as they often exhibit metalloid properties and superior electrical conductivity.^{148,155,239} However, most reported metal phosphides for supercapacitor applications are focused on the positive electrodes.²⁴⁰ In the last chapter, cobalt phosphide has been demonstrated as a high-performance negative electrode material for ASC. Therefore, we expect that by combining the various oxidation states of iron and the good electrical conductivity of metal phosphide, iron phosphide could be a suitable candidate for high-performance, low-cost supercapacitor negative electrode materials. Apart from the poor electrical conductivity, iron-based electrode materials usually suffer from the inferior cycling stability resulting from the physiochemical change/structural deformation during the long-time redox reaction,^{114,115} thus seriously limits their practical applications. In this regard, conducting polymer coating has been demonstrated as an efficient method to stabilize the supercapacitor electrodes.^{86,126,235,241} For example, Zeng et al. recently reported the PEDOT coating to improve the cycling stability as well as the capacitive properties of Ti-doped Fe_2O_3

core/shell nanorod arrays as the negative electrode material.¹²⁶ The Ti-Fe₂O₃@PEDOT exhibits a remarkable areal capacitance of 1.15 F/cm² at 1 mA/cm² and capacitance retention of 96.1% after 30000 cycles, which are significantly improved compared to that of bare Fe₂O₃ and Ti-Fe₂O₃ electrodes.

Based on those discussions, we herein report the first demonstration of FeP as the negative electrode material for supercapacitors. The as-synthesized FeP nanorod arrays present a high areal capacitance of 438.39 mF/cm² at the current density of 1 mA/cm². Furthermore, a FeP/PEDOT core/shell structure was designed to further boost the supercapacitance performance. The FeP/PEDOT exhibit an excellent areal capacitance of 790.59 mF/cm² and significantly improved cycling stability of 82.12% after 5000 cycles. Moreover, an ASC device was fabricated using MnO₂ positive and FeP/PEDOT negative electrodes. This work demonstrates FeP as a new material for high-performance supercapacitor negative electrode.

4.2. Experiments

4.2.1. Synthesis of FeP nanorod arrays

The FeP nanorod arrays were synthesized on carbon cloth by a two-step method. First, FeOOH nanorod arrays were growth via a hydrothermal procedure.¹¹⁵ The reaction solution was prepared by dissolving 0.182 g FeCl₃·6H₂O, 0.107 g Na₂SO₄ into 15 mL DI water. The solution was then transferred to a 20 mL autoclave with a piece of carbon cloth immersed in. The autoclave was kept at 160 °C for 6 hours. The synthesized FeOOH nanorod arrays were converted to FeP nanorod arrays by a phosphidation process.^{242,243} The FeOOH sample and 0.5 g NaH₂PO₂ were placed in a tube furnace and heated to 300 °C and kept for 2 h under static Ar atmosphere. The

loading amount of FeP nanorod arrays was determined as 2.94 mg/cm² by a high-precision microbalance.

4.2.2. Synthesis of FeP/PEDOT nanorod arrays

The PEDOT (Poly(3,4-ethylenedioxythiophene)) were coated on FeP nanorod arrays using an in-situ polymerization method.²⁴¹ The coating process was performed in precursor solution consisting of 0.1 M LiClO₄, 0.03 M EDOT (3,4-ethylenedioxythiophene), and 0.07 M sodium dodecyl sulfate (SDS) at 1 V for 1 min. The mass loading of PEDOT was 0.70 mg/cm².

4.2.3. Preparation of MnO₂ electrode

The MnO₂ electrode was prepared by electrodeposition of MnO₂ on carbon cloth.¹²⁶ A three-electrode configuration was used with carbon cloth as the working electrode, Pt wire as the counter electrode, Ag/AgCl as the reference electrode a 0.1 M manganese acetate and 0.1 M Na₂SO₄ aqueous solution as the electrolyte. The MnO₂ was obtained by applying a constant voltage of 1.0 V for 5 min. The mass loading of MnO₂ was 1.60 mg/cm².

4.2.4. Fabrication of the ASC

To fabricate the ASC, one FeP/PEDOT positive electrode and one MnO₂ electrode was sandwiched together with a separator (TF4030, NKK) in between. The device was then warped with duct tape and the electrolyte (1 M Na₂SO₄ aqueous solution) was injected. The device was then sealed with epoxy gel to avoid leaking.

4.2.5. Material Characterizations

The FESEM images were taken from a Hitachi S-4800 FESEM. The X-ray diffraction (XRD) was recorded on Rigaku MiniFlex II X-ray diffractometer. Raman spectra were collected by a Thermo-Fisher DXR dispersive Raman spectrometer with the excitation wavelengths of 532 nm.

4.2.6. Electrochemical Measurements

For single electrode, the electrochemical measurements were performed in a 1 M Na₂SO₄ aqueous electrolyte at ambient temperature. The conventional three-electrode configuration was used with a Pt wire and Ag/AgCl as the counter and the reference electrodes, respectively. The electrochemical impedance spectroscopy (EIS) measurements were conducted with a potential amplitude of 5 mV in the frequency range of 0.01 Hz to 100 kHz. For the ASC device, a two-electrode configuration was used.

4.3. Results and Discussion

The FeP nanorod arrays were directly synthesized on carbon cloth by a two-step process. The FeOOH nanorod arrays were first synthesized (Figure 4.1a), followed by the phosphidation. The XRD pattern can be indexed as a pure orthorhombic phase FeOOH (JCPDS No. 29-0713). The hydrolysis and polymerization reactions of Fe³⁺ are:²⁴⁴



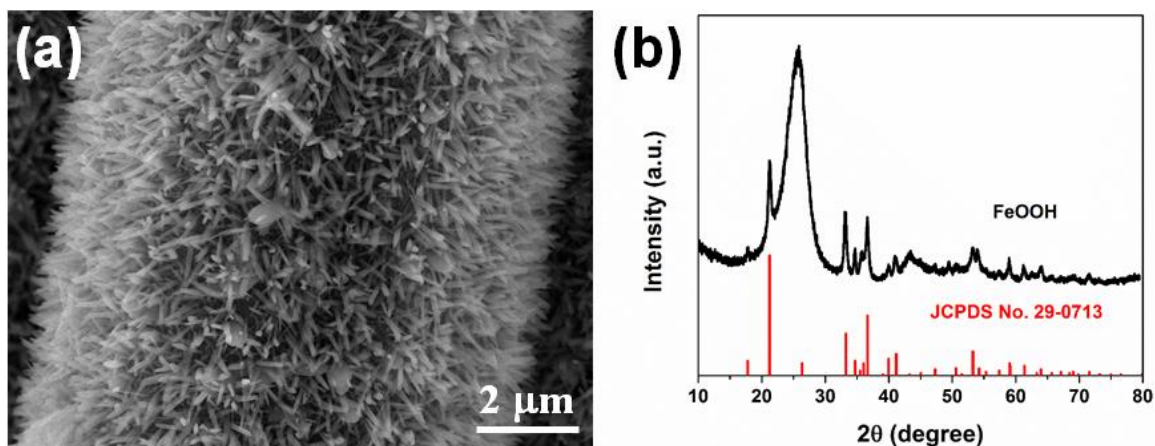


Figure 4.1. (a) FESEM image and (b) XRD patterns of FeOOH nanorod arrays.

As shown in the FESEM image of Figure 4.2a, the as-synthesized FeP nanorod arrays cover uniformly on the entire carbon cloth. The nanorods are with the typical length of around 1 μm and width of around 100 nm. After the PEDOT coating, the nanorod array nanostructures kept intact and no obvious morphology change was observed, as shown in Figure 4.2b. By comparing the inserted high magnification SEM images of Figure 4.2a and 1b, it is clear that the surface of nanorod became rough after the PEDOT coating. Some of the neighbor nanorods are fused together due to the excess coating process. The XRD patterns of FeP and FeP/PEDOT are shown in Figure 4.2c. All XRD peaks of FeP nanorod arrays, except two peaks around 25 and 43 degrees which belong to carbon cloth, can be indexed as orthorhombic FeP (JCPDS No. 65-2595). After PEDOT coating, the XRD patterns are similar to that of pure FeP, indicating that there is no phase change of FeP during the coating process. Moreover, the absence of extra peaks reveals the amorphous nature of PEDOT.^{245,246} The successful coating of PEDOT on the FeP nanorod arrays was further confirmed by Raman spectrum. As shown in Figure 4.2d, there are two broad peaks located at 1356 and 1597 cm^{-1} , corresponding to the D and G bands of carbon cloth, respectively.²⁴⁷ No peaks from FeP can be observed, which is consistent with previous reports.^{248,249} After coating, two

distinct Raman peaks located at 1441 and 1498 cm^{-1} emerged, which can be attributed to the symmetric and asymmetric C=C stretching of PEDOT, respectively.²⁵⁰ Additionally, two small shoulders are found at 1356 and 1597 cm^{-1} . They are due to the overlaying of D and G bands of carbon cloth and the strong Raman peaks of PEDOT.^{251–253} Overall, the presence of those Raman peaks proves the successful coating of the PEDOT on the FeP nanorod arrays.

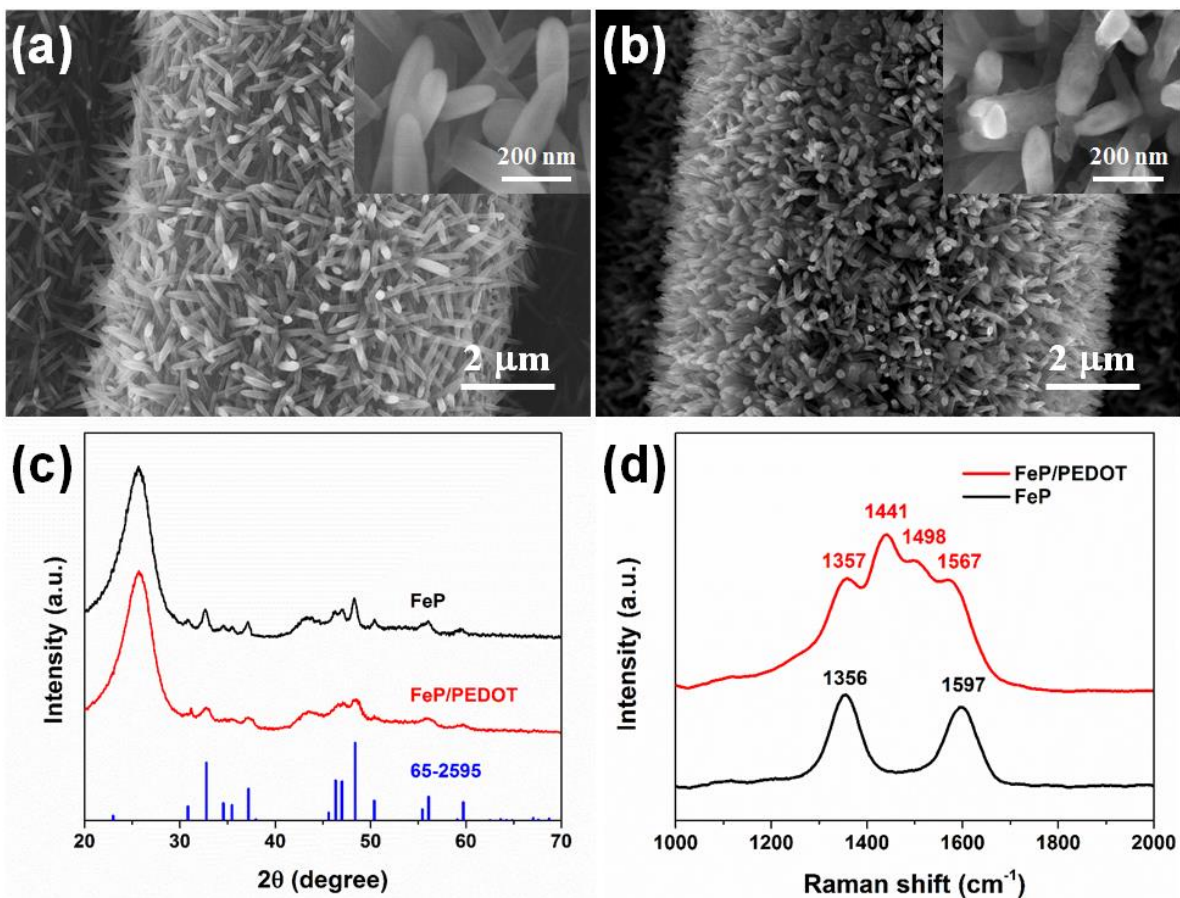


Figure 4.2. FESEM images of (a) FeP and (b) FeP/PEDOT nanorod arrays. The insets are the high magnification FESEM images. (c) XRD patterns and (d) Raman spectra of FeP and FeP/PEDOT nanorod arrays.

The PEDOT were coated on FeP nanorod arrays using an in-situ polymerization of EDOT. Figure 4.3 shows the chemical structures of EDOT and PEDOT. In the polymerization process,

LiClO_4 serves as the oxidation agent. SDS was used to increase the solubility of EDOT and to lower the oxidation potential.²⁵⁴

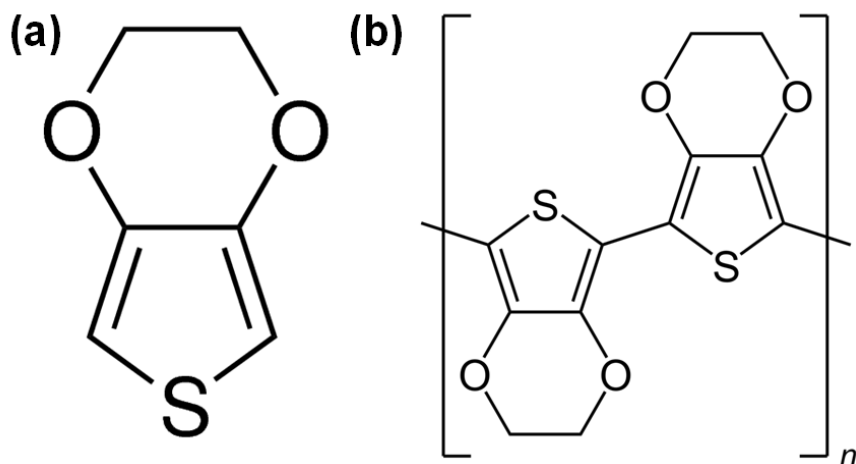


Figure 4.3. The chemical structures of (a) EDOT, and (b) PEDOT, respectively.

The morphology and structures of the FeP and FeP/PEDOT nanorods were further characterized by using TEM. Figure 4.4a shows the TEM image of a single FeP nanorod with a diameter around 100 nm. The electron diffraction patterns in Figure 4.4b reveal the polycrystalline nature of the FeP nanorod, and can be indexed as orthorhombic FeP phase. The HRTEM, as shown in Figure 4.4c, matches well with the simulation results of $[110]$ zone axis. Furthermore, the EDS mapping (Figure 4.4d) indicates the homogenous distribution of Fe and P elements, confirmed the successful synthesis of FeP nanorod. Similar to CoP nanowire as we discussed in the last chapter, the O element may come from the surface oxidation.

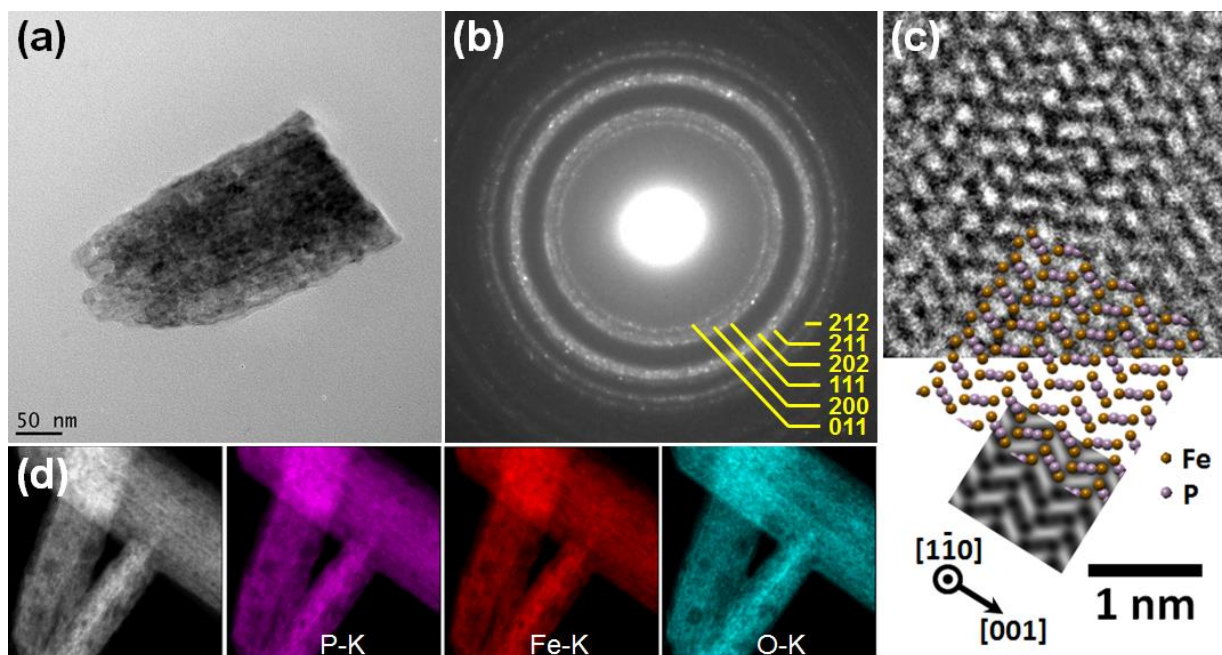


Figure 4.4. (a) TEM image, (b) SAED, and (c) HRTEM of FeP nanorod, (d) HAADF-STEM and corresponding EDS elemental mapping images of P, Fe, and O, respectively.

As shown in Figure 4.5a, it is clear that on a layer of shell has been deposited on the surface of FeP nanorod after the PEDOT coating. Compared to that of FeP nanorod, no change can be observed on either SAED (Figure 4.5b) or HRTEM (Figure 4.5c), revealing that the PEDOT shell is amorphous and there is no phase change of FeP core. To understand the chemical composition, EELS and EDS were performed. Figure 4.5d and e show the EELS spectrum FeP/PEDOT nanorod. As a result, EELS can detect these unambiguous Fe and P signals with phosphorus $L_{2,3}$ -edge and iron $L_{2,3}$ -edge at 713 and 148 eV, respectively.²⁴⁸ In addition, carbon K-edge and oxygen K-edge at 564 and 540 eV from the PEDOT are also included. The EDS spectra Figure 4.5f also confirmed the existence of Fe, P, C and O. Most importantly, from the EDS mapping of P, Fe, O, C and S elements as shown in Figure 4.5g, it is evidenced that the area of C and S is wider than that of Fe

and P (the length of yellow arrow \gg pink arrow). So, we can conclude FeP exist as the core and PEDOT as the shell.

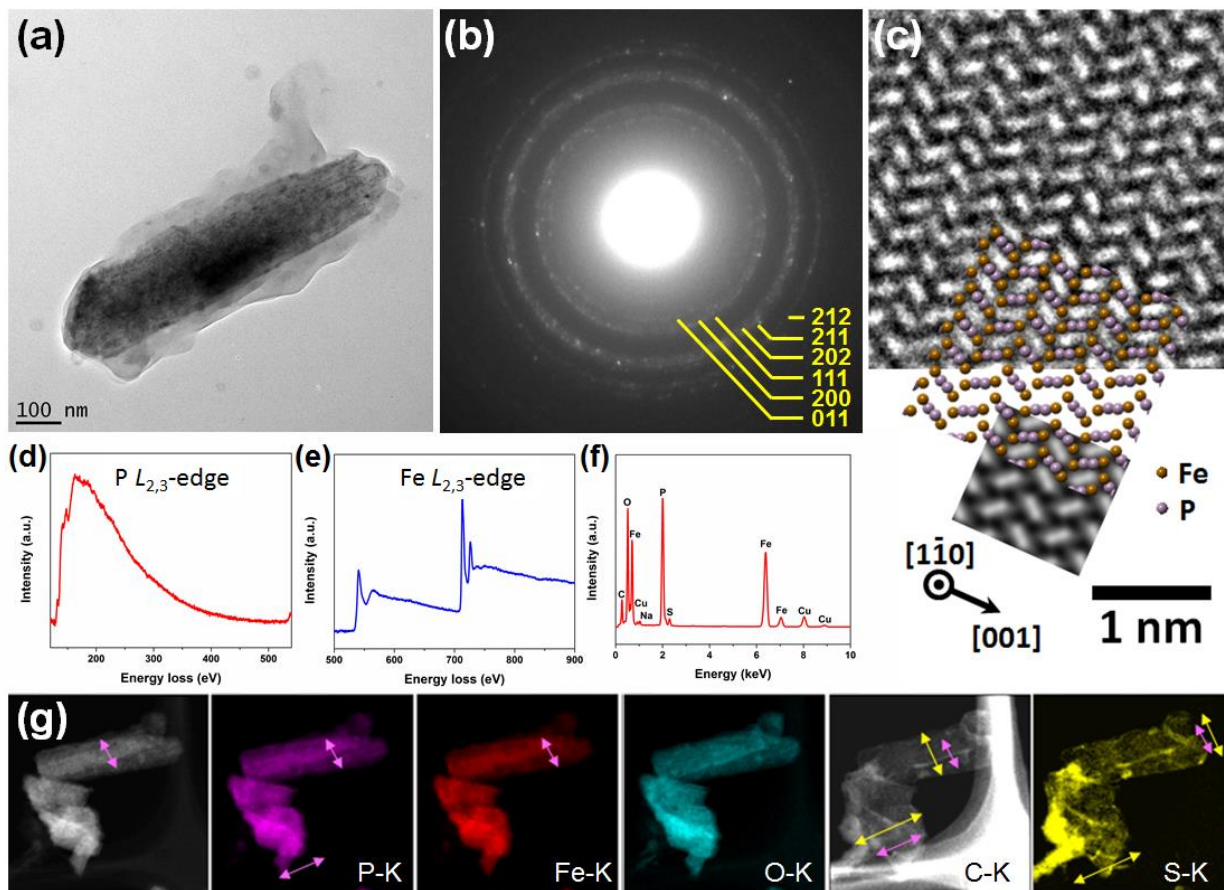


Figure 4.5. (a) TEM image, (b) SAED, and (c) HRTEM of FeP/PEDOT nanorod, (d,e) EELS spectrum and (f) EDS spectrum of FeP/PEDOT nanorods, (g) HAADF-STEM and corresponding EDS elemental mapping images of P, Fe, O, C and S, respectively.

The electrochemical performance of FeP nanorod arrays was first measured by cyclic voltammetry (CV) and galvanostatic charge/discharge methods in a 1 M Na_2SO_4 aqueous electrolyte in a conventional three-electrode configuration. The CV curves display quasi-rectangular shape, indicating the typical supercapacitance characteristic, as shown in Figure 4.6a. The galvanostatic charge/discharge curves of FeP/PEDOT are presenting in Figure 4.6b. All

curves display good symmetry in terms of charge and discharge time, demonstrating the ideal capacitive behavior as well.

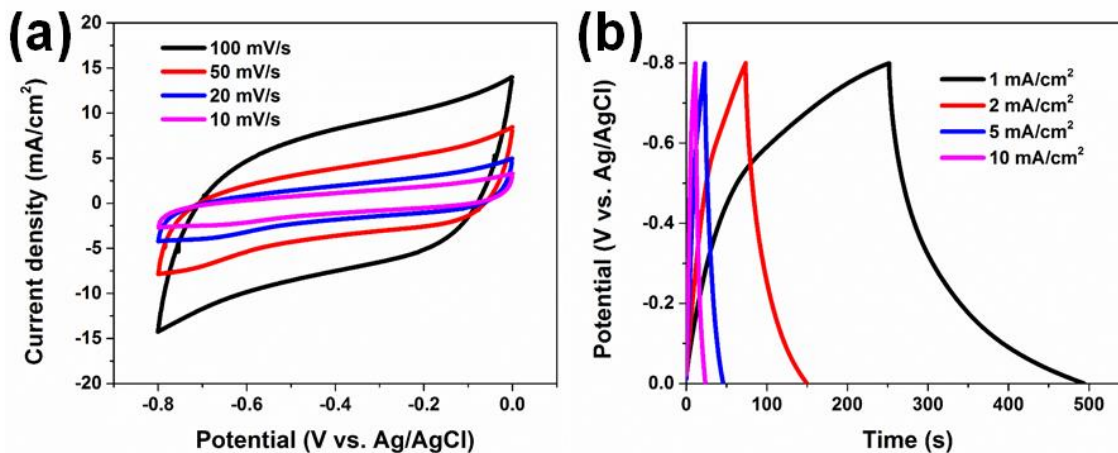


Figure 4.6. (a) CV curves of FeP electrode collected at scan rates from 10 to 100 mV/s. (b) Galvanostatic charge/discharge curves of FeP electrode at current densities from 1 to 10 mA/cm².

After PEDOT coating, the electrochemical performance was also measured using the same parameters. Figure 4.7a compares the CV curves of FeP and FeP/PEDOT collected at the scan rate of 100 mV/s. As expected, the FeP/PEDOT shows a considerably higher current density of FeP, indicating the higher capacitance of FeP/PEDOT. The CV curves were also collected by varying the scan rate. The symmetrical quasi-rectangular shape of the CV curves at different scan rates up to 100 mV/s reveals a good rate capacity for FeP/PEDOT electrode, as shown in Figure 4.7b. The galvanostatic charge/discharge curves of FeP/PEDOT are presenting in Figure 4.7c. The areal capacitance of FeP and FeP/PEDOT electrodes calculated based on discharge curves are presented in Figure 4.7d. After PEDOT coating, the areal capacitance can be further improved up to 790.59 mF/cm² at the current density of 1 mA/cm², which is almost twice as that of the FeP electrode (438.39 mF/cm²), and considerably higher than previously reported iron-based materials, such as Fe₂O₃ nanotubes (180.4 mF/cm² at 1 mA/cm²),¹⁹³ Fe₂O₃ nanoflakes (145.9 mF/cm² at 1

mA/cm²),²⁵⁵ tectorum-like α -Fe₂O₃/PPy nanoarrays (382.4 mF/cm² at 0.5 mA/cm²),²³⁵ α -Fe₂O₃@PANI nanowires (103 mF/cm² at 0.5 A/cm²),⁸⁶ oxygen-deficient Fe₂O₃ nanorods (382.7 mF/cm² at 0.5 mA/cm²),⁸⁵ and C@Fe₃O₄ nanosheets (127 mF/cm² at 1 mA/cm²).²⁵⁶ The enhancement of supercapacitance performance by PEDOT coating was further studied by electrochemical impedance spectroscopy (EIS). Figure 4.7e shows the Nyquist plots of FeP and FeP/PEDOT electrodes. The measured impedance spectra are fitted by an equivalent circuit (Figure 3.7c). As a result, FeP/PEDOT electrode shows lower R_S of 1.258 Ω and R_{CT} of 5.788 Ω compared to those of the pure FeP electrode (R_S = 4.065 Ω , R_{CT} = 7.007 Ω). The EIS data indicates that the coating of high conductive PEDOT layer would benefit the charge transfer in the electrode/electrolyte interface and improve the electrode conductivity, thus boost the supercapacitance performance.^{86,126,235} More importantly, PEDOT coating not only improves the electrochemical performance, but also the stability of FeP electrode. As shown in Figure 4.7f, the pure FeP electrode suffered from the unsatisfied stability of only 24.19% retention after 5000 cycles. After PEDOT coating, the stability can be greatly improved up to 82.12%.

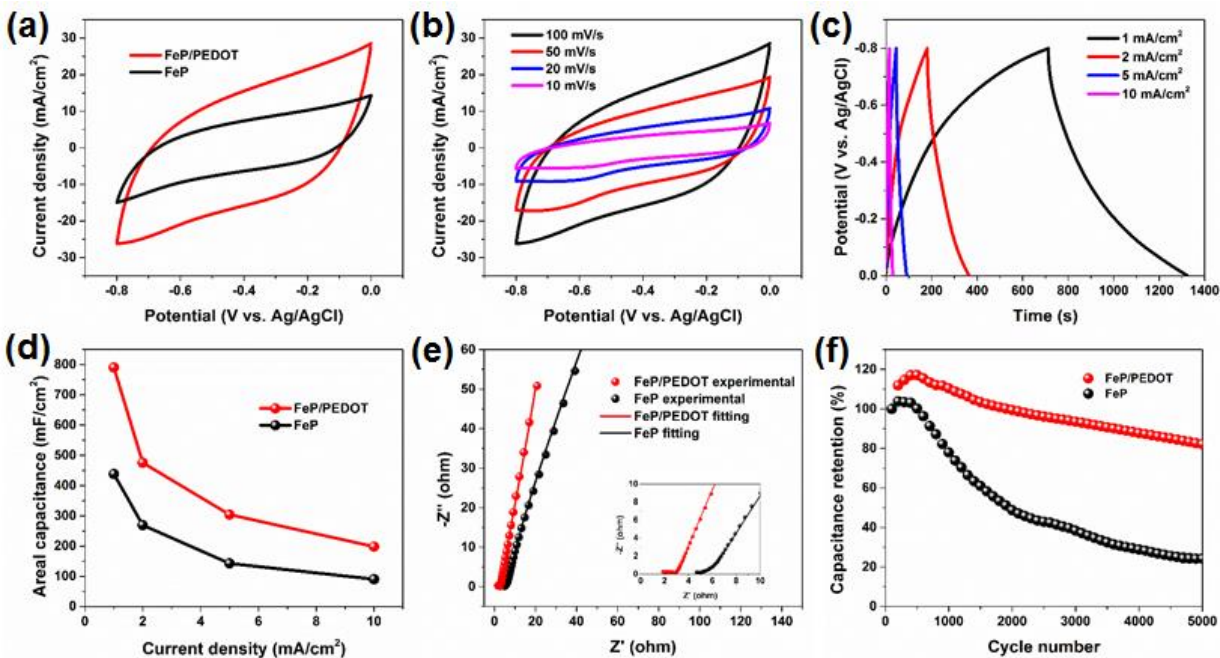


Figure 4.7. (a) CV curves of FeP and FeP/PEDOT electrodes at the scan rate of 100 mV/s. (b) CV curves of FeP/PEDOT electrode collected at scan rates from 10 to 100 mV/s. (c) Galvanostatic charge/discharge curves of FeP/PEDOT electrode at current densities from 1 to 10 mA/cm². (d) Comparison of the areal capacitance at different current densities of FeP and FeP/PEDOT electrodes. (e) Nyquist plots of FeP and FeP/PEDOT electrodes. The inset is the high-frequency part of the Nyquist plot. (f) Cycle stability of FeP and FeP/PEDOT electrodes.

It is believed that the structure deformation is the main reason which caused the instability of most iron-based materials.^{111,115} Therefore, we have conducted FESEM of FeP and FeP/PEDOT electrodes after cycling test to better understand the role of PEDOT coating in the improvement of the cycling stability. Figure 4.8a shows the FESEM of FeP electrode after 5000 CV cycles. Clearly, the original vertically aligned nanorod arrays structure has been demolished into mesh-like morphology. On the contrast, there is no obvious morphology change of the FeP/PEDOT electrode after the cycling test (Figure 4.8b). Obviously, the PEDOT coating can serve as a protection to prevent the FeP nanorod arrays from structure deformation.¹¹⁵ Therefore, the excellent supercapacitance performance of the FeP/PEDOT electrode can be ascribed into three main aspects: 1) the three-dimensional nanorod array structure provided larger surface area as well as short path for both ions and electrons, 2) the high electric conductivity of FeP facilitated the charge transfer during the charge/discharge process, 3) the subsequent PEDOT coating further improved the supercapacitance performance by reducing the series resistance and charge transfer resistance, 4) with the PEDOT serving as a protection layer, the mechanical durability and cycling stability of the FeP electrode were greatly enhanced.

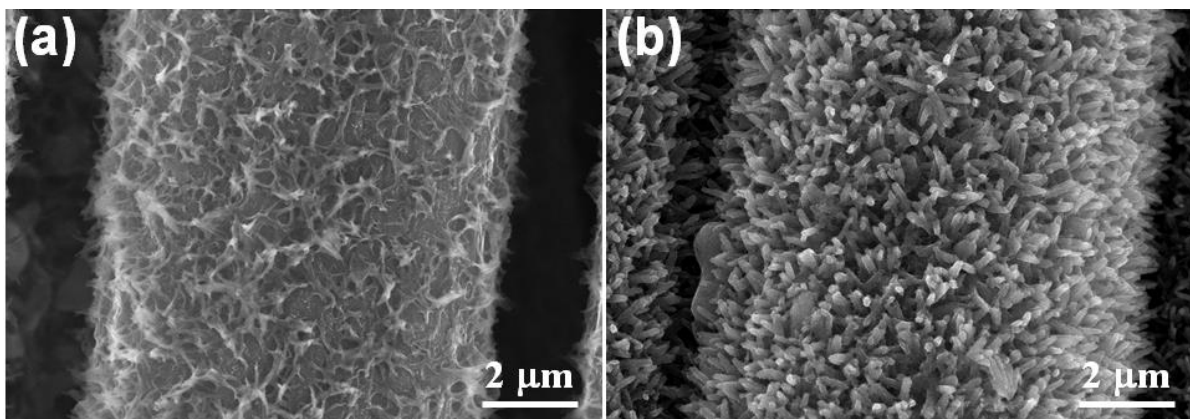


Figure 4.8. FESEM images of (a) FeP and (b) FeP/PEDOT nanorod arrays after cycling test.

To evaluate the practical application of FeP/PEDOT electrode, an aqueous asymmetric device was fabricated. MnO_2 was chosen as the positive electrode due to its high performance, facile synthesis method, and good stability. The MnO_2 thin film was synthesized on carbon cloth by electrodeposition method, as shown in the FESEM image of Figure 4.9a. The XRD pattern (Figure 4.9b), which can be indexed as $\delta\text{-MnO}_2$ (JCPDS No. 18-0802),²⁵⁷ confirmed the successful synthesis of MnO_2 .

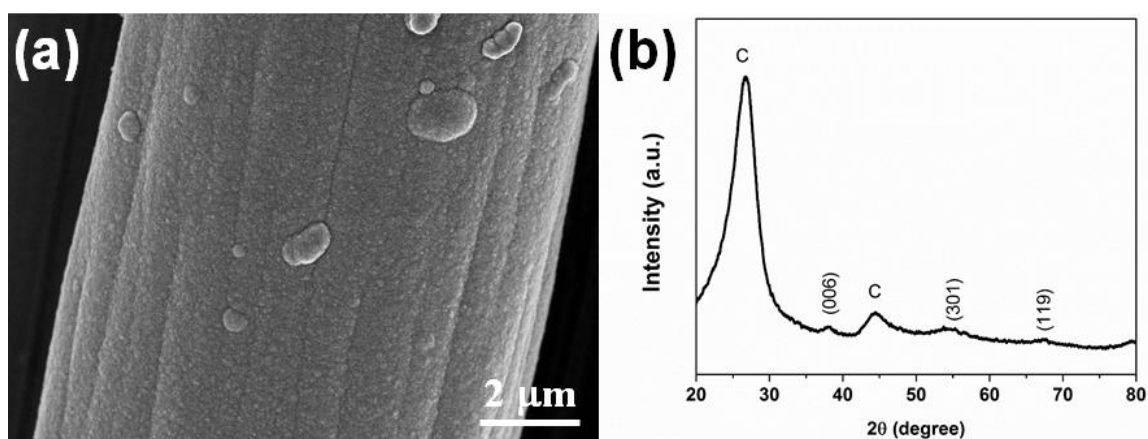


Figure 4.9. (a) FESEM image and (b) XRD patterns of MnO_2 electrode.

The electrochemical performance of MnO₂ electrode was also measured by in a 1 M Na₂SO₄ electrolyte (Figure 4.10). The MnO₂ electrode exhibits a good areal capacitance of 652.49 mF/cm² at 1 mA/cm².

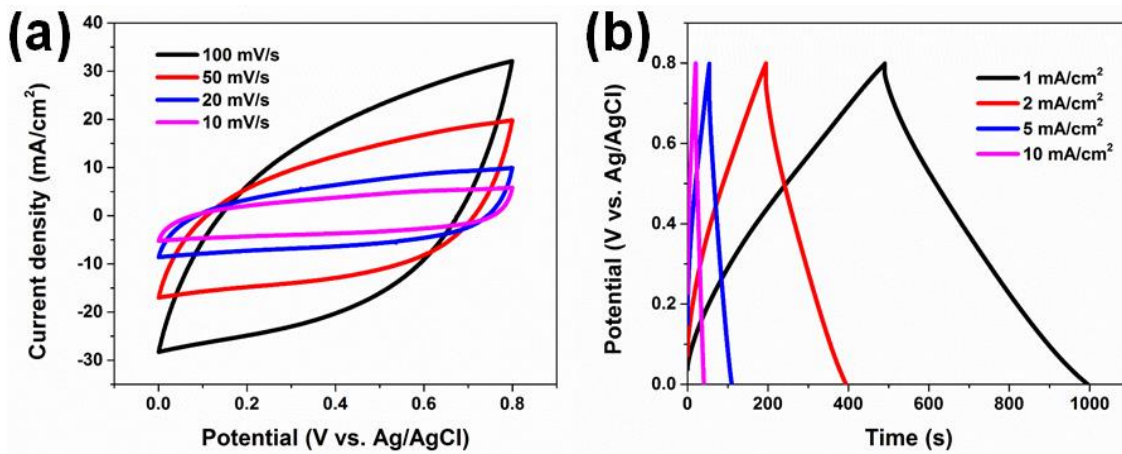


Figure 4.10. (a) CV curves of the MnO₂ electrode collected at scan rates from 10 to 100 mV/s. (b) Galvanostatic charge/discharge curves of the MnO₂ electrode at current densities from 1 to 10 mA/cm².

Based on the CV curves of FeP/PEDOT negative electrode and MnO₂ positive electrode as plotted in Figure 4.11a, the operation voltage of the ASC can be extended up to 1.6 V. The areal ratio of FeP/PEDOT negative electrode and MnO₂ positive electrode were calculated based on the areal capacitance to be 1:1.2. The ASC demonstrated a typical supercapacitor behavior, evident by the nearly rectangular shape of all CV curves at different scan rates, as shown in Figure 4.11b. In addition, the galvanostatic charge/discharge curves also show good symmetricity (Figure 4.11c), indicating the good reaction reversibility. The areal and volumetric capacitance of the ASC device was calculated based on the galvanostatic charge/discharge curves, and the results are shown in Figure 4.11d. The maximum areal and volumetric capacitance reach up to 362.53 mF/cm² and 4.53 F/cm³, respectively. Furthermore, the ASC shows a good stability of 81.17 % capacitance retention

after 5000 cycles, as shown in Figure 4.11e. The Ragone plots are shown in Figure 4.11f. The maximum energy density of the ASC is 1.61 mWh/cm^3 at a current density of 1 mA/cm^2 , which is higher than the recently reported values of ASCs, such as $\text{MnO}_2//\text{Fe}_2\text{O}_3$ (0.55 and 0.41 mWh/cm^3),^{85,193} $\text{MnO}_2//\text{Fe}_2\text{O}_3/\text{PPy}$ (0.22 mWh/cm^3),²³⁵ $\text{MnO}_2//\text{Ti-Fe}_2\text{O}_3@\text{PEDOT}$ (0.89 mWh/cm^3),¹²⁶ $\text{PANI}//\alpha\text{-Fe}_2\text{O}_3@\text{PANI}$ (0.35 mWh/cm^3),⁸⁶ $\text{MnO}_2//\text{CoSe}_2$ (0.588 mWh/cm^3),²¹⁹ $\text{Fe}_2\text{N}//\text{TiN}$ (0.61 mWh/cm^3),²⁵⁸ $\text{MnO}_2/\text{graphene}//\text{VOS}@C$ (0.87 mWh/cm^3),¹²⁷ and $\text{Co}_9\text{S}_8//\text{Co}_3\text{O}_4@\text{RuO}_2$ (1.44 mWh/cm^3).²⁵⁹

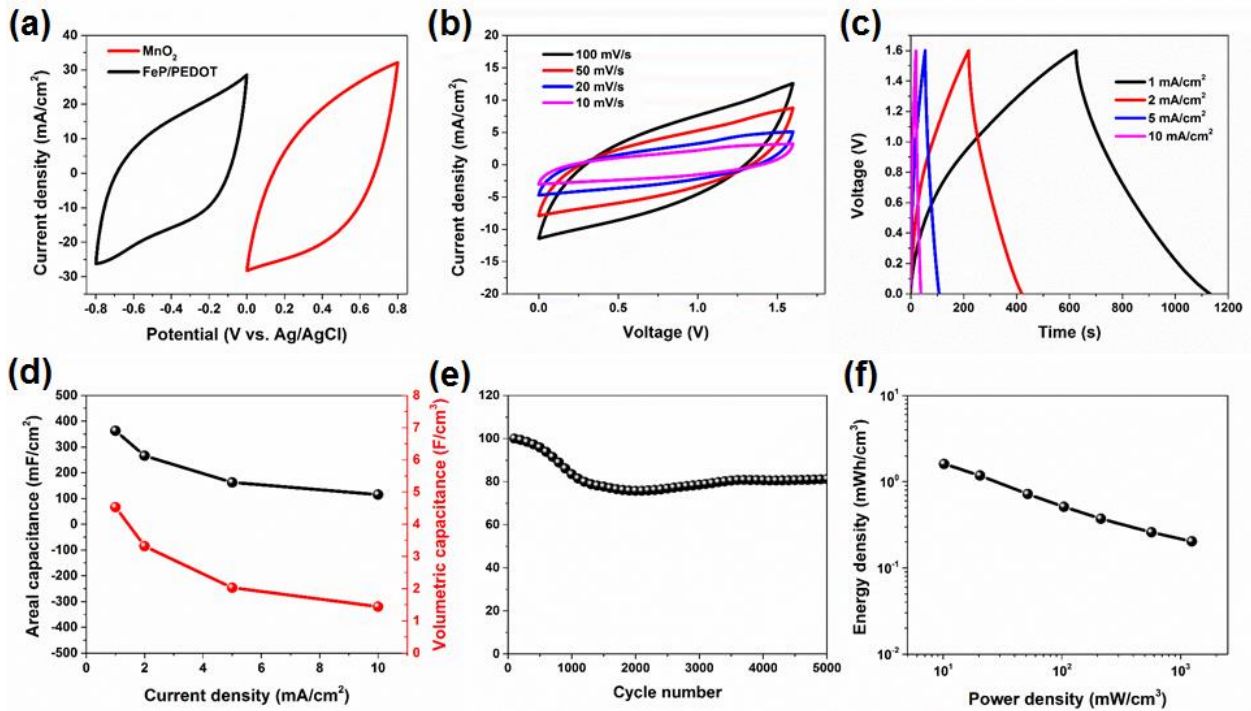


Figure 4.11. (a) CV curves of MnO_2 and FeP/PEDOT electrodes at the scan rate of 100 mV/s . (b) CV curves of the asymmetric device collected at scan rates from 10 to 100 mV/s . (c) Galvanostatic charge/discharge curves of the asymmetric device at current densities from 1 to 10 mA/cm^2 . (d) Areal and volumetric capacitance of the asymmetric device at different current densities. (e) Cycle stability of the asymmetric device. (f) Ragone plots of the asymmetric device.

4.4. Conclusion

In summary, FeP nanorod arrays have been synthesized on carbon cloth and demonstrated as a promising supercapacitor negative electrode material for the first time. The as-synthesized FeP nanorod arrays exhibit a high areal capacitance of 438.39 mF/cm^2 . A PEDOT coating has been adapted to further enhance the stability as well as capacitance performance. The FeP/PEDOT electrode represents an outstanding capacitance of 790.59 mF/cm^2 and a good stability of 82.12% retention after 5000 cycles. In addition, a $\text{MnO}_2//\text{FeP/PEDOT}$ ASC was fabricated with an excellent volumetric capacitance of 4.53 F/cm^3 and an energy density of 1.61 mWh/cm^3 . Our work shows that iron phosphide holds great promising as a new negative electrode material for supercapacitor applications.

Chapter 5 Conclusion and Perspective

The design and development of more reliable energy storage is the key to reach the goal of sustainability society. Supercapacitors have attracted significant interest in both academia and industry during the past several decades owing to their superior power density, fast charge/discharge rate and long cycle life. Nanomaterials have some intrinsic properties that can significantly enhance the supercapacitance performance, such as, large surface area, direct electron/ion diffusion path, etc, thus are widely applied in supercapacitors. Therefore, this dissertation puts main efforts into on the investigation of various nanostructured materials for supercapacitor applications, with a special emphasis on materials synthesis and structure analysis.

TiO₂ was first studied as an example of the metal oxide for supercapacitor electrode. A novel synthesis method has been developed to grow TiO₂ nanorod arrays on Ti substrate and the “dissolve and growth” mechanism was discussed. The as-synthesized TiO₂ nanorod arrays show good areal capacitance, great stability as well as good flexibility. It provides a simple and low-cost technique for high-performance flexible energy storage applications. On the other hand, two case studies have been done to successfully demonstrate metal phosphides as high-performance negative electrode materials for supercapacitor. Different nanostructured CoP and FeP have been synthesized and demonstrated high areal capacitance. However, it is observed that metal phosphides suffer from the low stability due to the irreversible electrochemical reaction or structural deformation. Nevertheless, we have successfully solved this issue by using gel electrolyte and PEDOT coating. In addition, both solid-state and aqueous asymmetric supercapacitor have been fabricated and shown great performance, which suggests that metal phosphides are promising negative electrode materials for high-performance supercapacitor applications.

Though great progress has been made in supercapacitors, lots of work still need to be done. Above all, the charge storage mechanism, especially for pseudocapacitance, must be deeply understood. Both advanced experimental and theoretical studies are necessary to provide a fundamental understanding of ion adsorption and charge storage on the nanoscale.

Reference

- (1) *Statistical Review of World Energy | Energy Economics | BP Global.*
- (2) Yang, Z.; Liu, J.; Baskaran, S.; Imhoff, C. H.; Holladay, J. D. Enabling Renewable Energy—and the Future Grid—with Advanced Electricity Storage. *JOM* **2010**, *62* (9), 14–23.
- (3) International Energy Outlook 2016 - Energy Information Administration
<https://www.eia.gov/outlooks/ieo/index.cfm> (accessed Mar 28, 2017).
- (4) Oreskes, N. BEYOND THE IVORY TOWER: The Scientific Consensus on Climate Change. *Science* **2004**, *306* (5702), 1686–1686.
- (5) Hansen, J.; Ruedy, R.; Sato, M.; Lo, K. GLOBAL SURFACE TEMPERATURE CHANGE. *Rev. Geophys.* **2010**, *48* (4), RG4004.
- (6) Sorrell, S.; Miller, R.; Bentley, R.; Speirs, J. Oil Futures: A Comparison of Global Supply Forecasts. *Energy Policy* **2010**, *38* (9), 4990–5003.
- (7) Miller, R. G.; Sorrell, S. R. The Future of Oil Supply. *Philos. Trans. R. Soc. A Math. Phys. Eng. Sci.* **2013**, *372* (2006), 20130179–20130179.
- (8) Yang, Z.; Zhang, J.; Kintner-Meyer, M. C. W.; Lu, X.; Choi, D.; Lemmon, J. P.; Liu, J. Electrochemical Energy Storage for Green Grid. *Chem. Rev.* **2011**, *111* (5), 3577–3613.
- (9) Chalamala, B. R. Portable Electronics and the Widening Energy Gap. *Proc. IEEE* **2007**, *95* (11), 2106–2107.
- (10) Chen, H.; Cong, T. N.; Yang, W.; Tan, C.; Li, Y.; Ding, Y. Progress in Electrical Energy Storage System: A Critical Review. *Prog. Nat. Sci.* **2009**, *19* (3), 291–312.
- (11) Amirante, R.; Cassone, E.; Distaso, E.; Tamburrano, P. Overview on Recent Developments in Energy Storage: Mechanical, Electrochemical and Hydrogen

- Technologies. *Energy Convers. Manag.* **2017**, *132*, 372–387.
- (12) Manthiram, A.; Fu, Y.; Su, Y.-S. In Charge of the World: Electrochemical Energy Storage. *J. Phys. Chem. Lett.* **2013**, *4* (8), 1295–1297.
- (13) Rolison, D. R.; Nazar, L. F. Electrochemical Energy Storage to Power the 21st Century. *MRS Bull.* **2011**, *36* (7), 486–493.
- (14) Dunn, B.; Kamath, H.; Tarascon, J.-M. Electrical Energy Storage for the Grid: A Battery of Choices. *Science* **2011**, *334* (6058), 928–935.
- (15) Winter, M.; Brodd, R. J. What Are Batteries, Fuel Cells, and Supercapacitors? *Chem. Rev.* **2004**, *104* (10), 4245–4270.
- (16) Miller, J. R.; Simon, P. Electrochemical Capacitors for Energy Management. *Science* **2008**, *321* (5889), 651–652.
- (17) Wang, Y.; Song, Y.; Xia, Y. Electrochemical Capacitors: Mechanism, Materials, Systems, Characterization and Applications. *Chem. Soc. Rev.* **2016**, *45* (21), 5925–5950.
- (18) Simon, P.; Gogotsi, Y. Materials for Electrochemical Capacitors. *Nat. Mater.* **2008**, *7* (11), 845–854.
- (19) Simon, P.; Gogotsi, Y.; Dunn, B. Where Do Batteries End and Supercapacitors Begin? *Science* **2014**, *343* (6176), 1210–1211.
- (20) Okubo, M.; Hosono, E.; Kim, J.; Enomoto, M.; Kojima, N.; Kudo, T.; Zhou, H.; Honma, I. Nanosize Effect on High-Rate Li-Ion Intercalation in LiCoO₂ Electrode. *J. Am. Chem. Soc.* **2007**, *129* (23), 7444–7452.
- (21) Boisset, A.; Athouël, L.; Jacquemin, J.; Porion, P.; Brousse, T.; Anouti, M. Comparative Performances of Birnessite and Cryptomelane MnO₂ as Electrode Material in Neutral Aqueous Lithium Salt for Supercapacitor Application. *J. Phys. Chem. C* **2013**, *117* (15),

- 7408–7422.
- (22) Shimizu, W.; Makino, S.; Takahashi, K.; Imanishi, N.; Sugimoto, W. Development of a 4.2 V Aqueous Hybrid Electrochemical Capacitor Based on MnO₂ Positive and Protected Li Negative Electrodes. *J. Power Sources* **2013**, *241*, 572–577.
- (23) Pilon, L.; Wang, H.; D'Entremont, A. Recent Advances in Continuum Modeling of Interfacial and Transport Phenomena in Electric Double Layer Capacitors. *J. Electrochem. Soc.* **2015**, *162* (5), A5158–A5178.
- (24) Zhan, C.; Lian, C.; Zhang, Y.; Thompson, M. W.; Xie, Y.; Wu, J.; Kent, P. R. C.; Cummings, P. T.; Jiang, D.; Wesolowski, D. J. Computational Insights into Materials and Interfaces for Capacitive Energy Storage. *Adv. Sci.* **2017**, *4* (7), 1700059.
- (25) Chapman, D. L. LI. A Contribution to the Theory of Electrocapillarity. *Philos. Mag. Ser. 6* **1913**, *25* (148), 475–481.
- (26) Grahame, D. C. The Electrical Double Layer and the Theory of Electrocapillarity. *Chem. Rev.* **1947**, *41* (3), 441–501.
- (27) Zhang, L. L.; Zhao, X. S. Carbon-Based Materials as Supercapacitor Electrodes. *Chem. Soc. Rev.* **2009**, *38* (9), 2520.
- (28) Burt, R.; Birkett, G.; Zhao, X. S.; Kim, Y.-H.; Bedrov, D.; Taberna, P. L.; Naguib, M.; Simon, P.; Barsoum, M. W.; Gogotsi, Y. A Review of Molecular Modelling of Electric Double Layer Capacitors. *Phys. Chem. Chem. Phys.* **2014**, *16* (14), 6519.
- (29) Huang, J.; Sumpter, B. G.; Meunier, V. A Universal Model for Nanoporous Carbon Supercapacitors Applicable to Diverse Pore Regimes, Carbon Materials, and Electrolytes. *Chem. - A Eur. J.* **2008**, *14* (22), 6614–6626.
- (30) Salanne, M.; Rotenberg, B.; Naoi, K.; Kaneko, K.; Taberna, P.-L.; Grey, C. P.; Dunn, B.;

- Simon, P. Efficient Storage Mechanisms for Building Better Supercapacitors. *Nat. Energy* **2016**, *1* (6), 16070.
- (31) Griffin, J. M.; Forse, A. C.; Wang, H.; Trease, N. M.; Taberna, P.-L.; Simon, P.; Grey, C. P.; Kanoh, H.; Gogotsi, Y.; Simon, P.; Kaneko, K. Ion Counting in Supercapacitor Electrodes Using NMR Spectroscopy. *Faraday Discuss.* **2014**, *176* (0), 49–68.
- (32) Forse, A. C.; Merlet, C.; Griffin, J. M.; Grey, C. P. New Perspectives on the Charging Mechanisms of Supercapacitors. *J. Am. Chem. Soc.* **2016**, *138* (18), 5731–5744.
- (33) Conway, B. E. *Electrochemical Supercapacitors: Scientific Fundamentals and Technological Applications*; Springer US: Boston, MA, 1999.
- (34) Augustyn, V.; Simon, P.; Dunn, B. Pseudocapacitive Oxide Materials for High-Rate Electrochemical Energy Storage. *Energy Environ. Sci.* **2014**, *7* (5), 1597.
- (35) Conway, B. E.; Pell, W. G. Double-Layer and Pseudocapacitance Types of Electrochemical Capacitors and Their Applications to the Development of Hybrid Devices. *J. Solid State Electrochem.* **2003**, *7* (9), 637–644.
- (36) Augustyn, V. Tuning the Interlayer of Transition Metal Oxides for Electrochemical Energy Storage. *J. Mater. Res.* **2017**, *32* (1), 2–15.
- (37) Conway, B. E. Two-Dimensional and Quasi-Two-Dimensional Isotherms for Li Intercalation and Upd Processes at Surfaces. *Electrochim. Acta* **1993**, *38* (9), 1249–1258.
- (38) Liu, T.-C.; Pell, W. G.; Conway, B. E.; Roberson, S. L. Behavior of Molybdenum Nitrides as Materials for Electrochemical Capacitors. *J. Electrochem. Soc.* **1998**, *145* (6), 1882.
- (39) Ardizzone, S.; Fregonara, G.; Trasatti, S. “Inner” and “outer” Active Surface of RuO₂ Electrodes. *Electrochim. Acta* **1990**, *35* (1), 263–267.
- (40) Brousse, T.; Belanger, D.; Long, J. W. To Be or Not To Be Pseudocapacitive? *J.*

- Electrochem. Soc.* **2015**, *162* (5), A5185–A5189.
- (41) Conway, B. E.; Birss, V.; Wojtowicz, J. The Role and Utilization of Pseudocapacitance for Energy Storage by Supercapacitors. *J. Power Sources* **1997**, *66* (1–2), 1–14.
- (42) Costentin, C.; Porter, T. R.; Savéant, J.-M. How Do Pseudocapacitors Store Energy? Theoretical Analysis and Experimental Illustration. *ACS Appl. Mater. Interfaces* **2017**, *9* (10), 8649–8658.
- (43) Pandolfo, A. G.; Hollenkamp, A. F. Carbon Properties and Their Role in Supercapacitors. *J. Power Sources* **2006**, *157* (1), 11–27.
- (44) Zhang, S. W.; Chen, G. Z. Manganese Oxide Based Materials for Supercapacitors. *Energy Mater.* **2008**, *3* (3), 186–200.
- (45) Chen, G. Z. Supercapacitor and Supercapattery as Emerging Electrochemical Energy Stores. *Int. Mater. Rev.* **2017**, *62* (4), 173–202.
- (46) Abru?a, H. D.; Kiya, Y.; Henderson, J. C. Batteries and Electrochemical Capacitors. *Phys. Today* **2008**, *61* (12), 43–47.
- (47) Wang, G.; Zhang, L.; Zhang, J. A Review of Electrode Materials for Electrochemical Supercapacitors. *Chem. Soc. Rev.* **2012**, *41* (2), 797–828.
- (48) Choudhary, N.; Li, C.; Moore, J.; Nagaiah, N.; Zhai, L.; Jung, Y.; Thomas, J. Asymmetric Supercapacitor Electrodes and Devices. *Adv. Mater.* **2017**, *29* (21), 1605336.
- (49) Long, J. W.; Bélanger, D.; Brousse, T.; Sugimoto, W.; Sassin, M. B.; Crosnier, O. Asymmetric Electrochemical capacitors—Stretching the Limits of Aqueous Electrolytes. *MRS Bull.* **2011**, *36* (7), 513–522.
- (50) Wang, F.; Xiao, S.; Hou, Y.; Hu, C.; Liu, L.; Wu, Y. Electrode Materials for Aqueous Asymmetric Supercapacitors. *RSC Adv.* **2013**, *3* (32), 13059–13084.

- (51) Yu, M.; Wang, Z.; Han, Y.; Tong, Y.; Lu, X.; Yang, S. Recent Progress in the Development of Anodes for Asymmetric Supercapacitors. *J. Mater. Chem. A* **2016**, *4* (13), 4634–4658.
- (52) Sun, J.; Wu, C.; Sun, X.; Hu, H.; Zhi, C.; Hou, L.; Yuan, C. Recent Progresses in High-Energy-Density All Pseudocapacitive-Electrode-Materials-Based Asymmetric Supercapacitors. *J. Mater. Chem. A* **2017**, *5* (20), 9443–9464.
- (53) Akinwolemiwa, B.; Wei, C.; Chen, G. Z. Mechanisms and Designs of Asymmetrical Electrochemical Capacitors. *Electrochim. Acta* **2017**, *247*, 344–357.
- (54) Zhang, J.; Zhao, X. S. On the Configuration of Supercapacitors for Maximizing Electrochemical Performance. *ChemSusChem* **2012**, *5* (5), 818–841.
- (55) Dai, Z.; Peng, C.; Chae, J. H.; Ng, K. C.; Chen, G. Z. Cell Voltage versus Electrode Potential Range in Aqueous Supercapacitors. *Sci. Rep.* **2015**, *5* (1), 9854.
- (56) Peng, C.; Zhang, S.; Zhou, X.; Chen, G. Z.; Fray, D. J.; Chen, G. Z.; Roncali, J. Unequalisation of Electrode Capacitances for Enhanced Energy Capacity in Asymmetrical Supercapacitors. *Energy Environ. Sci.* **2010**, *3* (10), 1499.
- (57) Zuo, W.; Li, R.; Zhou, C.; Li, Y.; Xia, J.; Liu, J. Battery-Supercapacitor Hybrid Devices: Recent Progress and Future Prospects. *Adv. Sci.* **2017**, *4* (7), 1600539–n/a.
- (58) Naoi, K.; Naoi, W.; Aoyagi, S.; Miyamoto, J.-I.; Kamino, T. New Generation “nanohybrid Supercapacitor”. *Acc. Chem. Res.* **2013**, *46* (5), 1075–1083.
- (59) Choi, H. S.; Park, C. R. Theoretical Guidelines to Designing High Performance Energy Storage Device Based on Hybridization of Lithium-Ion Battery and Supercapacitor. *J. Power Sources* **2014**, *259*, 1–14.
- (60) Presser, V.; Dennison, C. R.; Campos, J.; Knehr, K. W.; Kumbur, E. C.; Gogotsi, Y. The

- Electrochemical Flow Capacitor: A New Concept for Rapid Energy Storage and Recovery. *Adv. Energy Mater.* **2012**, 2 (7), 895–902.
- (61) Dennison, C. R.; Beidaghi, M.; Hatzell, K. B.; Campos, J. W.; Gogotsi, Y.; Kumbur, E. C. Effects of Flow Cell Design on Charge Percolation and Storage in the Carbon Slurry Electrodes of Electrochemical Flow Capacitors. *J. Power Sources* **2014**, 247, 489–496.
- (62) El-Kady, M. F.; Kaner, R. B. Scalable Fabrication of High-Power Graphene Micro-Supercapacitors for Flexible and on-Chip Energy Storage. *Nat. Commun.* **2013**, 4, 1475.
- (63) Liu, L.; Niu, Z.; Chen, J. Unconventional Supercapacitors from Nanocarbon-Based Electrode Materials to Device Configurations. *Chem. Soc. Rev.* **2016**, 45 (15), 4340–4363.
- (64) Qi, D.; Liu, Y.; Liu, Z.; Zhang, L.; Chen, X. Design of Architectures and Materials in In-Plane Micro-Supercapacitors: Current Status and Future Challenges. *Adv. Mater.* **2017**, 29 (5), 1602802.
- (65) Dong, L.; Xu, C.; Li, Y.; Huang, Z.-H.; Kang, F.; Yang, Q.-H.; Zhao, X. Flexible Electrodes and Supercapacitors for Wearable Energy Storage: A Review by Category. *J. Mater. Chem. A* **2016**, 4 (13), 4659–4685.
- (66) Yu, D.; Qian, Q.; Wei, L.; Jiang, W.; Goh, K.; Wei, J.; Zhang, J.; Chen, Y.; Luo, Y.; Peng, H.; Gong, L.; Yen, W.-C.; Mai, W.; Chen, J.; Huo, K.; Chueh, Y. L.; Wang, Z. L.; Zhou, J. Emergence of Fiber Supercapacitors. *Chem. Soc. Rev.* **2015**, 44 (3), 647–662.
- (67) Luo, B.; Ye, D.; Wang, L. Recent Progress on Integrated Energy Conversion and Storage Systems. *Adv. Sci.* **2017**, 1700104.
- (68) Zhang, Y.; Feng, H.; Wu, X.; Wang, L.; Zhang, A.; Xia, T.; Dong, H.; Li, X.; Zhang, L. Progress of Electrochemical Capacitor Electrode Materials: A Review. *Int. J. Hydrogen Energy* **2009**, 34 (11), 4889–4899.

- (69) Borenstein, A.; Hanna, O.; Attias, R.; Luski, S.; Brousse, T.; Aurbach, D. Carbon-Based Composite Materials for Supercapacitor Electrodes: A Review. *J. Mater. Chem. A* **2017**, *5* (25), 12653–12672.
- (70) Simon, P.; Gogotsi, Y. Capacitive Energy Storage in Nanostructured Carbon–Electrolyte Systems. *Acc. Chem. Res.* **2013**, *46* (5), 1094–1103.
- (71) Chen, T.; Dai, L. Carbon Nanomaterials for High-Performance Supercapacitors. *Mater. Today* **2013**, *16* (7–8), 272–280.
- (72) Liu, J. Charging Graphene for Energy. *Nat. Nanotechnol.* **2014**, *9* (10), 739–741.
- (73) Frackowiak, E. Carbon Materials for Supercapacitor Application. *Phys. Chem. Chem. Phys.* **2007**, *9* (15), 1774.
- (74) Largeot, C.; Portet, C.; Chmiola, J.; Taberna, P.-L.; Gogotsi, Y.; Simon, P. Relation between the Ion Size and Pore Size for an Electric Double-Layer Capacitor. *J. Am. Chem. Soc.* **2008**, *130* (9), 2730–2731.
- (75) Liu, T.; Zhang, F.; Song, Y.; Li, Y.; Liu, X.; Iijima, S.; Kaneko, K.; Gogotsi, Y.; Kleitz, F.; Taberna, P. L.; Chaudret, B.; Gogotsi, Y.; Simon, P.; Lin, Y.; Hu, L. Revitalizing Carbon Supercapacitor Electrodes with Hierarchical Porous Structures. *J. Mater. Chem. A* **2017**, *2*, 10882–10888.
- (76) Frackowiak, E.; Abbas, Q.; Béguin, F. Carbon/carbon Supercapacitors. *J. Energy Chem.* **2013**, *22* (2), 226–240.
- (77) Zhao, X.; Sánchez, B. M.; Dobson, P. J.; Grant, P. S. The Role of Nanomaterials in Redox-Based Supercapacitors for next Generation Energy Storage Devices. *Nanoscale* **2011**, *3* (3), 839.
- (78) Trasatti, S.; Buzzanca, G. Ruthenium Dioxide: A New Interesting Electrode Material.

- Solid State Structure and Electrochemical Behaviour. *J. Electroanal. Chem. Interfacial Electrochem.* **1971**, *29* (2), A1–A5.
- (79) Li, W.; Liu, Q.; Sun, Y.; Sun, J.; Zou, R.; Li, G.; Hu, X.; Song, G.; Ma, G.; Yang, J.; Chen, Z.; Hu, J. MnO₂ Ultralong Nanowires with Better Electrical Conductivity and Enhanced Supercapacitor Performances. *J. Mater. Chem.* **2012**, *22* (30), 14864.
- (80) Yu, Z.; Duong, B.; Abbitt, D.; Thomas, J. Highly Ordered MnO₂ Nanopillars for Enhanced Supercapacitor Performance. *Adv. Mater.* **2013**, *25* (24), 3302–3306.
- (81) Ma, Z.; Shao, G.; Fan, Y.; Wang, G.; Song, J.; Shen, D. Construction of Hierarchical α -MnO₂ Nanowires@Ultrathin δ -MnO₂ Nanosheets Core–Shell Nanostructure with Excellent Cycling Stability for High-Power Asymmetric Supercapacitor Electrodes. *ACS Appl. Mater. Interfaces* **2016**, *8* (14), 9050–9058.
- (82) Xia, X.; Tu, J.; Zhang, Y.; Mai, Y.; Wang, X.; Gu, C.; Zhao, X. Freestanding Co₃O₄ Nanowire Array for High Performance Supercapacitors. *RSC Adv.* **2012**, *2* (5), 1835–1841.
- (83) Zhai, T.; Wan, L.; Sun, S.; Chen, Q.; Sun, J.; Xia, Q.; Xia, H. Phosphate Ion Functionalized Co₃O₄ Ultrathin Nanosheets with Greatly Improved Surface Reactivity for High Performance Pseudocapacitors. *Adv. Mater.* **2016**, *29* (7), 1604167.
- (84) Cheng, G.; Kou, T.; Zhang, J.; Si, C.; Gao, H.; Zhang, Z. O₂-/O- Functionalized Oxygen-Deficient Co₃O₄ Nanorods as High Performance Supercapacitor Electrodes and Electrocatalysts towards Water Splitting. *Nano Energy* **2017**, *38*, 155–166.
- (85) Lu, X.; Zeng, Y.; Yu, M.; Zhai, T.; Liang, C.; Xie, S.; Balogun, M.-S.; Tong, Y. Oxygen-Deficient Hematite Nanorods as High-Performance and Novel Negative Electrodes for Flexible Asymmetric Supercapacitors. *Adv. Mater.* **2014**, *26* (19), 3148–3155.

- (86) Lu, X.-F.; Chen, X.-Y.; Zhou, W.; Tong, Y.-X.; Li, G.-R. α -Fe₂O₃@PANI Core–Shell Nanowire Arrays as Negative Electrodes for Asymmetric Supercapacitors. *ACS Appl. Mater. Interfaces* **2015**, *7* (27), 14843–14850.
- (87) Xia, H.; Hong, C.; Li, B.; Zhao, B.; Lin, Z.; Zheng, M.; Savirov, S. V.; Aldoshin, S. M. Facile Synthesis of Hematite Quantum-Dot/Functionalized Graphene-Sheet Composites as Advanced Anode Materials for Asymmetric Supercapacitors. *Adv. Funct. Mater.* **2015**, *25* (4), 627–635.
- (88) Mak, W. F.; Wee, G.; Aravindan, V.; Gupta, N.; Mhaisalkar, S. G.; Madhavi, S. High-Energy Density Asymmetric Supercapacitor Based on Electrospun Vanadium Pentoxide and Polyaniline Nanofibers in Aqueous Electrolyte. *J. Electrochem. Soc.* **2012**, *159* (9), A1481–A1488.
- (89) Qu, Q.; Zhu, Y.; Gao, X.; Wu, Y. Core–Shell Structure of Polypyrrole Grown on V₂O₅ Nanoribbon as High Performance Anode Material for Supercapacitors. *Adv. Energy Mater.* **2012**, *2* (8), 950–955.
- (90) Pang, H.; Lu, Q.; Zhang, Y.; Li, Y.; Gao, F. Selective Synthesis of Nickel Oxide Nanowires and Length Effect on Their Electrochemical Properties. *Nanoscale* **2010**, *2* (6), 920.
- (91) Lu, Z.; Chang, Z.; Liu, J.; Sun, X. Stable Ultrahigh Specific Capacitance of NiO Nanorod Arrays. *Nano Res.* **2011**, *4* (7), 658–665.
- (92) Li, Z.; Shao, M.; Zhou, L.; Zhang, R.; Zhang, C.; Han, J.; Wei, M.; Evans, D. G.; Duan, X. A Flexible All-Solid-State Micro-Supercapacitor Based on Hierarchical CuO@layered Double Hydroxide Core–shell Nanoarrays. *Nano Energy* **2016**, *20*, 294–304.
- (93) Zhang, X.; Shi, W.; Zhu, J.; Kharistal, D. J.; Zhao, W.; Lalia, B. S.; Hng, H. H.; Yan, Q.

- High-Power and High-Energy-Density Flexible Pseudocapacitor Electrodes Made from Porous CuO Nanobelts and Single-Walled Carbon Nanotubes. *ACS Nano* **2011**, 5 (3), 2013–2019.
- (94) Tang, W.; Liu, L.; Tian, S.; Li, L.; Yue, Y.; Wu, Y.; Zhu, K. Aqueous Supercapacitors of High Energy Density Based on MoO₃ Nanoplates as Anode Material. *Chem. Commun.* **2011**, 47 (36), 10058–10060.
- (95) Peng, H.; Ma, G.; Mu, J.; Sun, K.; Lei, Z. Low-Cost and High Energy Density Asymmetric Supercapacitors Based on Polyaniline Nanotubes and MoO₃ Nanobelts. *J. Mater. Chem. A* **2014**, 2 (27), 10384–10388.
- (96) Barzegar, F.; Bello, A.; Momodu, D. Y.; Dangbegnon, J. K.; Taghizadeh, F.; Madito, M. J.; Masikhwa, T. M.; Manyala, N. Asymmetric Supercapacitor Based on an α -MoO₃ Cathode and Porous Activated Carbon Anode Materials. *RSC Adv.* **2015**, 5 (47), 37462–37468.
- (97) Wang, X.; Li, G.; Chen, Z.; Augustyn, V.; Ma, X.; Wang, G.; Dunn, B.; Lu, Y. High-Performance Supercapacitors Based on Nanocomposites of Nb₂O₅ Nanocrystals and Carbon Nanotubes. *Adv. Energy Mater.* **2011**, 1 (6), 1089–1093.
- (98) Pusawale, S. N.; Deshmukh, P. R.; Lokhande, C. D. Chemical Synthesis of Nanocrystalline SnO₂ Thin Films for Supercapacitor Application. *Appl. Surf. Sci.* **2011**, 257 (22), 9498–9502.
- (99) Lu, X.; Wang, G.; Zhai, T.; Yu, M.; Gan, J.; Tong, Y.; Li, Y. Hydrogenated TiO₂ Nanotube Arrays for Supercapacitors. *Nano Lett.* **2012**, 12 (3), 1690–1696.
- (100) Zheng, H.; Zhai, T.; Yu, M.; Xie, S.; Liang, C.; Zhao, W.; Wang, S. C. I.; Zhang, Z.; Lu, X. TiO₂@C Core-Shell Nanowires for High-Performance and Flexible Solid-State

- Supercapacitors. *J. Mater. Chem. C* **2013**, *1* (2), 225–229.
- (101) Zhou, H.; Zhang, Y. Electrochemically Self-Doped TiO₂ Nanotube Arrays for Supercapacitors. *J. Phys. Chem. C* **2014**, *118* (11), 5626–5636.
- (102) Chang, K.-H.; Hu, C.-C.; Huang, C.-M.; Liu, Y.-L.; Chang, C.-I. Microwave-Assisted Hydrothermal Synthesis of Crystalline WO₃–WO₃·0.5H₂O Mixtures for Pseudocapacitors of the Asymmetric Type. *J. Power Sources* **2011**, *196* (4), 2387–2392.
- (103) Wang, F.; Zhan, X.; Cheng, Z.; Wang, Z.; Wang, Q.; Xu, K.; Safdar, M.; He, J. Tungsten Oxide@Polypyrrole Core-Shell Nanowire Arrays as Novel Negative Electrodes for Asymmetric Supercapacitors. *Small* **2015**, *11* (6), 749–755.
- (104) Wang, J.; Dong, S.; Ding, B.; Wang, Y.; Hao, X.; Dou, H.; Xia, Y.; Zhang, X. Pseudocapacitive Materials for Electrochemical Capacitors: From Rational Synthesis to Capacitance Optimization. *Natl. Sci. Rev.* **2017**, *4* (1), 71–90.
- (105) Fu, R.; Ma, Z.; Zheng, J. P. Proton NMR and Dynamic Studies of Hydrrous Ruthenium Oxide. *J. Phys. Chem. B* **2002**, *106* (14), 3592–3596.
- (106) Hu, C.-C.; Chen, W.-C.; Chang, K.-H. How to Achieve Maximum Utilization of Hydrrous Ruthenium Oxide for Supercapacitors. *J. Electrochem. Soc.* **2004**, *151* (2), A281.
- (107) Wei, W.; Cui, X.; Chen, W.; Ivey, D. G.; Choi, W. C.; Li, Z.; Shi, J. L.; Greenbaum, S. G.; Carter, R. Manganese Oxide-Based Materials as Electrochemical Supercapacitor Electrodes. *Chem. Soc. Rev.* **2011**, *40* (3), 1697–1721.
- (108) Toupin, M.; Brousse, T.; Bélanger, D. Charge Storage Mechanism of MnO₂ Electrode Used in Aqueous Electrochemical Capacitor. *Chem. Mater.* **2004**, *16* (16), 3184–3190.
- (109) Yan, W.; Kim, J. Y.; Xing, W.; Donovan, K. C.; Ayvazian, T.; Penner, R. M. Lithographically Patterned Gold/Manganese Dioxide Core/Shell Nanowires for High

- Capacity, High Rate, and High Cyclability Hybrid Electrical Energy Storage. *Chem. Mater.* **2012**, *24* (12), 2382–2390.
- (110) Rakhi, R. B.; Chen, W.; Cha, D.; Alshareef, H. N. Substrate Dependent Self-Organization of Mesoporous Cobalt Oxide Nanowires with Remarkable Pseudocapacitance. *Nano Lett.* **2012**, *12* (5), 2559–2567.
- (111) Zeng, Y.; Yu, M.; Meng, Y.; Fang, P.; Lu, X.; Tong, Y. Iron-Based Supercapacitor Electrodes: Advances and Challenges. *Adv. Energy Mater.* **2016**, *6* (24), 1601053.
- (112) Nithya, V. D.; Arul, N. S. Review on α -Fe₂O₃ Based Negative Electrode for High Performance Supercapacitors. *J. Power Sources* **2016**, *327*, 297–318.
- (113) Xia, Q.; Xu, M.; Xia, H.; Xie, J. Nanostructured Iron Oxide/Hydroxide-Based Electrode Materials for Supercapacitors. *ChemNanoMat* **2016**, *2* (7), 588–600.
- (114) Guan, C.; Liu, J.; Wang, Y.; Mao, L.; Fan, Z.; Shen, Z.; Zhang, H.; Wang, J. Iron Oxide-Decorated Carbon for Supercapacitor Anodes with Ultrahigh Energy Density and Outstanding Cycling Stability. *ACS Nano* **2015**, *9* (5), 5198–5207.
- (115) Li, R.; Wang, Y.; Zhou, C.; Wang, C.; Ba, X.; Li, Y.; Huang, X.; Liu, J. Carbon-Stabilized High-Capacity Ferroferric Oxide Nanorod Array for Flexible Solid-State Alkaline Battery-Supercapacitor Hybrid Device with High Environmental Suitability. *Adv. Funct. Mater.* **2015**, *25* (33), 5384–5394.
- (116) Zúkalová, M.; Kalbáč, M.; Kavan, L.; Exnar, I.; Graetzel, M. Pseudocapacitive Lithium Storage in TiO₂ (B). *Chem. Mater.* **2005**, *17* (5), 1248–1255.
- (117) Dylla, A. G.; Henkelman, G.; Stevenson, K. J. Lithium Insertion in Nanostructured TiO₂ (B) Architectures. *Acc. Chem. Res.* **2013**, *46* (5), 1104–1112.
- (118) Wang, Y.; Hong, Z.; Wei, M.; Xia, Y. Layered H₂Ti₆O₁₃-Nanowires: A New

- Promising Pseudocapacitive Material in Non-Aqueous Electrolyte. *Adv. Funct. Mater.* **2012**, *22* (24), 5185–5193.
- (119) Augustyn, V.; Come, J.; Lowe, M. A.; Kim, J. W.; Taberna, P.-L.; Tolbert, S. H.; Abruña, H. D.; Simon, P.; Dunn, B. High-Rate Electrochemical Energy Storage through Li⁺ Intercalation Pseudocapacitance. *Nat. Mater.* **2013**, *12* (6), 518–522.
- (120) Lu, X.; Wang, G.; Zhai, T.; Yu, M.; Gan, J.; Tong, Y.; Li, Y. Hydrogenated TiO₂ Nanotube Arrays for Supercapacitors. *Nano Lett.* **2012**, *12* (3), 1690–1696.
- (121) Zhai, T.; Xie, S.; Yu, M.; Fang, P.; Liang, C.; Lu, X.; Tong, Y. Oxygen Vacancies Enhancing Capacitive Properties of MnO₂ Nanorods for Wearable Asymmetric Supercapacitors. *Nano Energy* **2014**, *8*, 255–263.
- (122) Xiao, X.; Peng, Z.; Chen, C.; Zhang, C.; Beidaghi, M.; Yang, Z.; Wu, N.; Huang, Y.; Miao, L.; Gogotsi, Y.; Zhou, J. Freestanding MoO_{3-x} Nanobelt/carbon Nanotube Films for Li-Ion Intercalation Pseudocapacitors. *Nano Energy* **2014**, *9*, 355–363.
- (123) Wang, Y.; Zhou, T.; Jiang, K.; Da, P.; Peng, Z.; Tang, J.; Kong, B.; Cai, W.-B.; Yang, Z.; Zheng, G. Reduced Mesoporous Co₃O₄ Nanowires as Efficient Water Oxidation Electrocatalysts and Supercapacitor Electrodes. *Adv. Energy Mater.* **2014**, *4* (16), 1400696.
- (124) Kou, T.; Yao, B.; Liu, T.; Li, Y. Recent Advances in Chemical Methods for Activating Carbon and Metal Oxide Based Electrodes for Supercapacitors. *J. Mater. Chem. A* **2017**, *5* (33), 17151–17173.
- (125) Kang, J.; Hirata, A.; Kang, L.; Zhang, X.; Hou, Y.; Chen, L.; Li, C.; Fujita, T.; Akagi, K.; Chen, M. Enhanced Supercapacitor Performance of MnO₂ by Atomic Doping. *Angew. Chemie Int. Ed.* **2013**, *52* (6), 1664–1667.

- (126) Zeng, Y.; Han, Y.; Zhao, Y.; Zeng, Y.; Yu, M.; Liu, Y.; Tang, H.; Tong, Y.; Lu, X. Advanced Ti-Doped Fe₂O₃@PEDOT Core/Shell Anode for High-Energy Asymmetric Supercapacitors. *Adv. Energy Mater.* **2015**, *5* (12), 1402176.
- (127) Zhai, T.; Lu, X.; Ling, Y.; Yu, M.; Wang, G.; Liu, T.; Liang, C.; Tong, Y.; Li, Y. A New Benchmark Capacitance for Supercapacitor Anodes by Mixed-Valence Sulfur-Doped V₆O₁₃-X. *Adv. Mater.* **2014**, *26* (33), 5869–5875.
- (128) Chi, H. Z.; Li, Y.; Xin, Y.; Qin, H.; Santos-Peñac, J.; Ma, L.; Wang, J.; Yang, S.; Akagi, K.; Chen, M. Boron-Doped Manganese Dioxide for Supercapacitors. *Chem. Commun.* **2014**, *50* (87), 13349–13352.
- (129) Zhu, T.; Xia, B.; Zhou, L.; Wen (David) Lou, X. Arrays of Ultrafine CuS Nanoneedles Supported on a CNT Backbone for Application in Supercapacitors. *J. Mater. Chem.* **2012**, *22* (16), 7851.
- (130) Shi, J.; Li, X.; He, G.; Zhang, L.; Li, M. Electrodeposition of High-Capacitance 3D CoS/graphene Nanosheets on Nickel Foam for High-Performance Aqueous Asymmetric Supercapacitors. *J. Mater. Chem. A* **2015**, *3* (41), 20619–20626.
- (131) Yang, J.; Duan, X.; Guo, W.; Li, D.; Zhang, H.; Zheng, W. Electrochemical Performances Investigation of NiS/rGO Composite as Electrode Material for Supercapacitors. *Nano Energy* **2014**, *5*, 74–81.
- (132) Rui, X.; Tan, H.; Yan, Q. Nanostructured Metal Sulfides for Energy Storage. *Nanoscale* **2014**, *6* (17), 9889.
- (133) Xia, C.; Li, P.; Gandi, A. N.; Schwingenschlögl, U.; Alshareef, H. N. Is NiCo₂S₄ Really a Semiconductor? *Chem. Mater.* **2015**, *27* (19), 6482–6485.
- (134) Gao, Y.-P.; Huang, K.-J. NiCo₂S₄ Materials for Supercapacitor Applications. *Chem.* -

- An Asian J.* **2017**, *12* (16), 1969–1984.
- (135) Chhowalla, M.; Shin, H. S.; Eda, G.; Li, L.-J.; Loh, K. P.; Zhang, H. The Chemistry of Two-Dimensional Layered Transition Metal Dichalcogenide Nanosheets. *Nat. Chem.* **2013**, *5* (4), 263–275.
- (136) Manzeli, S.; Ovchinnikov, D.; Pasquier, D.; Yazyev, O. V; Kis, A. 2D Transition Metal Dichalcogenides. *Nat. Rev. Mater.* **2017**, *2* (8), 17033.
- (137) Mendoza-Sánchez, B.; Gogotsi, Y. Synthesis of Two-Dimensional Materials for Capacitive Energy Storage. *Adv. Mater.* **2016**, *28* (29), 6104–6135.
- (138) Acerce, M.; Voiry, D.; Chhowalla, M. Metallic 1T Phase MoS₂ Nanosheets as Supercapacitor Electrode Materials. *Nat. Nanotechnol.* **2015**, *10* (4), 313–318.
- (139) Balogun, M.-S.; Qiu, W.; Wang, W.; Fang, P.; Lu, X.; Tong, Y. Recent Advances in Metal Nitrides as High-Performance Electrode Materials for Energy Storage Devices. *J. Mater. Chem. A* **2015**, *3* (4), 1364–1387.
- (140) Balogun, M.-S.; Huang, Y.; Qiu, W.; Yang, H.; Ji, H.; Tong, Y. Updates on the Development of Nanostructured Transition Metal Nitrides for Electrochemical Energy Storage and Water Splitting. *Mater. Today* **2017**.
- (141) Choi, D.; Blomgren, G. E.; Kumta, P. N. Fast and Reversible Surface Redox Reaction in Nanocrystalline Vanadium Nitride Supercapacitors. *Adv. Mater.* **2006**, *18* (9), 1178–1182.
- (142) Li, X.; Elshahawy, A. M.; Guan, C.; Wang, J. Metal Phosphides and Phosphates-Based Electrodes for Electrochemical Supercapacitors. *Small* **2017**, 1701530.
- (143) An, C.; Wang, Y.; Wang, Y.; Liu, G.; Li, L.; Qiu, F.; Xu, Y.; Jiao, L.; Yuan, H. Facile Synthesis and Superior Supercapacitor Performances of Ni₂P/rGO Nanoparticles. *RSC Adv.* **2013**, *3* (14), 4628–4633.

- (144) Lu, Y.; Liu, J.; Liu, X.; Huang, S.; Wang, T.; Wang, X.; Gu, C.; Tu, J.; Mao, S. X. Facile Synthesis of Ni-Coated Ni₂P for Supercapacitor Applications. *CrystEngComm* **2013**, *15* (35), 7071–7079.
- (145) Duan, S.; Wang, R. Au/Ni₁₂P₅ Core/shell Nanocrystals from Bimetallic Heterostructures: In Situ Synthesis, Evolution and Supercapacitor Properties. *NPG Asia Mater* **2014**, *6* (9), e122.
- (146) Wan, H.; Li, L.; Chen, Y.; Gong, J.; Duan, M.; Liu, C.; Zhang, J.; Wang, H. One Pot Synthesis of Ni₁₂P₅ Hollow Nanocapsules as Efficient Electrode Materials for Oxygen Evolution Reactions and Supercapacitor Applications. *Electrochim. Acta* **2017**, *229*, 380–386.
- (147) Du, W.; Kang, R.; Geng, P.; Xiong, X.; Li, D.; Tian, Q.; Pang, H. New Asymmetric and Symmetric Supercapacitor Cells Based on Nickel Phosphide Nanoparticles. *Mater. Chem. Phys.* **2015**, *165*, 207–214.
- (148) Zhou, K.; Zhou, W.; Yang, L.; Lu, J.; Cheng, S.; Mai, W.; Tang, Z.; Li, L.; Chen, S. Ultrahigh-Performance Pseudocapacitor Electrodes Based on Transition Metal Phosphide Nanosheets Array via Phosphorization: A General and Effective Approach. *Adv. Funct. Mater.* **2015**, *25* (48), 7530–7538.
- (149) Du, W.; Wei, S.; Zhou, K.; Guo, J.; Pang, H.; Qian, X. One-Step Synthesis and Graphene-Modification to Achieve Nickel Phosphide Nanoparticles with Electrochemical Properties Suitable for Supercapacitors. *Mater. Res. Bull.* **2015**, *61*, 333–339.
- (150) Liu, S.; Sankar, K. V.; Kundu, A.; Ma, M.; Kwon, J.-Y.; Jun, S. C. Honeycomb-Like Interconnected Network of Nickel Phosphide Heteronanoparticles with Superior Electrochemical Performance for Supercapacitors. *ACS Appl. Mater. Interfaces* **2017**,

acsami.7b05384.

- (151) Hu, Y.; Liu, M.; Yang, Q.; Kong, L.; Kang, L. Facile Synthesis of High Electrical Conductive CoP via Solid-State Synthetic Routes for Supercapacitors. *J. Energy Chem.* **2017**, *26* (1), 49–55.
- (152) Elshahawy, A. M.; Guan, C.; Li, X.; Zhang, H.; Hu, Y.; Wu, H.; Pennycook, S. J.; Wang, J. Sulfur-Doped Cobalt Phosphide Nanotube Arrays for Highly Stable Hybrid Supercapacitor. *Nano Energy* **2017**, *39*, 162–171.
- (153) Zhang, G.; Fang, J.; Sun, L.; Li, S.; Xu, K. Cobalt Phosphide Nanowire Arrays Grown on Carbon Cloth as Novel Electrode Material for Supercapacitors. *Mater. Sci. Semicond. Process.* **2017**, *66*, 140–143.
- (154) Chen, Y.-C.; Chen, Z.-B.; Lin, Y.-G.; Hsu, Y.-K. Synthesis of Copper Phosphide Nanotube Arrays as Electrodes for Asymmetric Supercapacitors. *ACS Sustain. Chem. Eng.* **2017**, *5* (5), 3863–3870.
- (155) Liang, H.; Xia, C.; Jiang, Q.; Gandi, A. N.; Schwingenschlögl, U.; Alshareef, H. N. Low Temperature Synthesis of Ternary Metal Phosphides Using Plasma for Asymmetric Supercapacitors. *Nano Energy* **2017**, *35*, 331–340.
- (156) Kong, M.; Wang, Z.; Wang, W.; Ma, M.; Liu, D.; Hao, S.; Kong, R.; Du, G.; Asiri, A. M.; Yao, Y.; Sun, X. NiCoP Nanoarray: A Superior Pseudocapacitor Electrode with High Areal Capacitance. *Chem. - A Eur. J.* **2017**, *23* (18), 4435–4441.
- (157) Ding, R.; Li, X.; Shi, W.; Xu, Q.; Liu, E. One-Pot Solvothermal Synthesis of Ternary Ni-Co-P Micro/nano-Structured Materials for High Performance Aqueous Asymmetric Supercapacitors. *Chem. Eng. J.* **2017**, *320*, 376–388.
- (158) Shirakawa, H.; Louis, E. J.; MacDiarmid, A. G.; Chiang, C. K.; Heeger, A. J. Synthesis of

- Electrically Conducting Organic Polymers: Halogen Derivatives of Polyacetylene, (CH)
X. *J. Chem. Soc. Chem. Commun.* **1977**, No. 16, 578.
- (159) Snook, G. A.; Kao, P.; Best, A. S. Conducting-Polymer-Based Supercapacitor Devices and Electrodes. *J. Power Sources* **2011**, *196* (1), 1–12.
- (160) Bryan, A. M.; Santino, L. M.; Lu, Y.; Acharya, S.; D'Arcy, J. M. Conducting Polymers for Pseudocapacitive Energy Storage. *Chem. Mater.* **2016**, *28* (17), 5989–5998.
- (161) Shown, I.; Ganguly, A.; Chen, L.-C.; Chen, K.-H. Conducting Polymer-Based Flexible Supercapacitor. *Energy Sci. Eng.* **2015**, *3* (1), 2–26.
- (162) Song, Y.; Liu, T.-Y.; Xu, X.-X.; Feng, D.-Y.; Li, Y.; Liu, X.-X. Pushing the Cycling Stability Limit of Polypyrrole for Supercapacitors. *Adv. Funct. Mater.* **2015**, *25* (29), 4626–4632.
- (163) Aricò, A. S.; Bruce, P.; Scrosati, B.; Tarascon, J.-M.; van Schalkwijk, W. Nanostructured Materials for Advanced Energy Conversion and Storage Devices. *Nat. Mater.* **2005**, *4* (5), 366–377.
- (164) Chen, X.; Mao, S. S. Titanium Dioxide Nanomaterials: Synthesis, Properties, Modifications, and Applications. *Chem. Rev.* **2007**, *107* (7), 2891–2959.
- (165) FUJISHIMA, A.; HONDA, K. Electrochemical Photolysis of Water at a Semiconductor Electrode. *Nature* **1972**, *238* (5358), 37–38.
- (166) Zhang, Y.; Jiang, Z.; Huang, J.; Lim, L. Y.; Li, W.; Deng, J.; Gong, D.; Tang, Y.; Lai, Y.; Chen, Z. Titanate and Titania Nanostructured Materials for Environmental and Energy Applications: A Review. *RSC Adv.* **2015**, *5* (97), 79479–79510.
- (167) Salari, M.; Aboutalebi, S. H.; Konstantinov, K.; Liu, H. K.; Shankar, K.; Grimes, C. A.; Yang, Y.; Li, X.; Zhang, L.; Schmuki, P. A Highly Ordered Titania Nanotube Array as a

- Supercapacitor Electrode. *Phys. Chem. Chem. Phys.* **2011**, *13* (11), 5038.
- (168) Zhu, K.; Neale, N. R.; Miedaner, A.; Frank, A. J. Enhanced Charge-Collection Efficiencies and Light Scattering in Dye-Sensitized Solar Cells Using Oriented TiO₂ Nanotubes Arrays. *Nano Lett.* **2007**, *7* (1), 69–74.
- (169) Kang, T.-S.; Smith, A. P.; Taylor, B. E.; Durstock, M. F. Fabrication of Highly-Ordered TiO₂ Nanotube Arrays and Their Use in Dye-Sensitized Solar Cells. *Nano Lett.* **2009**, *9* (2), 601–606.
- (170) Mor, G. K.; Shankar, K.; Paulose, M.; Varghese, O. K.; Grimes, C. A. Use of Highly-Ordered TiO₂ Nanotube Arrays in Dye-Sensitized Solar Cells. *Nano Lett.* **2006**, *6* (2), 215–218.
- (171) Lee, J.-C.; Kim, T. G.; Choi, H.-J.; Sung, Y.-M. Enhanced Photochemical Response of TiO₂/CdSe Heterostructured Nanowires. *Cryst. Growth Des.* **2007**, *7* (12), 2588–2593.
- (172) Feng, X.; Shankar, K.; Varghese, O. K.; Paulose, M.; Latempa, T. J.; Grimes, C. A. Vertically Aligned Single Crystal TiO₂ Nanowire Arrays Grown Directly on Transparent Conducting Oxide Coated Glass: Synthesis Details and Applications. *Nano Lett.* **2008**, *8* (11), 3781–3786.
- (173) Liu, B.; Aydil, E. S. Growth of Oriented Single-Crystalline Rutile TiO₂ Nanorods on Transparent Conducting Substrates for Dye-Sensitized Solar Cells. *J. Am. Chem. Soc.* **2009**, *131* (11), 3985–3990.
- (174) Hernández-Rodríguez, E.; Márquez-Herrera, A.; Zaleta-Alejandre, E.; Meléndez-Lira, M.; Cruz, W. de la; Zapata-Torres, M. Effect of Electrode Type in the Resistive Switching Behaviour of TiO₂ Thin Films. *J. Phys. D. Appl. Phys.* **2013**, *46* (4), 45103.
- (175) Li, X. Z. PCED2.0—A Computer Program for the Simulation of Polycrystalline Electron

- Diffraction Pattern. *Ultramicroscopy* **2010**, *110* (4), 297–304.
- (176) Guo, W.; Xu, C.; Wang, X.; Wang, S.; Pan, C.; Lin, C.; Wang, Z. L. Rectangular Bunched Rutile TiO₂ Nanorod Arrays Grown on Carbon Fiber for Dye-Sensitized Solar Cells. *J. Am. Chem. Soc.* **2012**, *134* (9), 4437–4441.
- (177) Hosono, E.; Fujihara, S.; Kakiuchi, K.; Imai, H. Growth of Submicrometer-Scale Rectangular Parallelepiped Rutile TiO₂ Films in Aqueous TiCl₃ Solutions under Hydrothermal Conditions. *J. Am. Chem. Soc.* **2004**, *126* (25), 7790–7791.
- (178) Vayssieres, L.; Keis, K.; Lindquist, S.-E.; Hagfeldt, A. Purpose-Built Anisotropic Metal Oxide Material: 3D Highly Oriented Microrod Array of ZnO. *J. Phys. Chem. B* **2001**, *105* (17), 3350–3352.
- (179) Kumar, A.; Madaria, A. R.; Zhou, C. Growth of Aligned Single-Crystalline Rutile TiO₂ Nanowires on Arbitrary Substrates and Their Application in Dye-Sensitized Solar Cells. *J. Phys. Chem. C* **2010**, *114* (17), 7787–7792.
- (180) Zhu, D.; Wang, Y.; Yuan, G.; Xia, H. High-Performance Supercapacitor Electrodes Based on Hierarchical Ti@MnO₂ Nanowire Arrays. *Chem. Commun.* **2014**, *50* (22), 2876–2878.
- (181) Zhao, G.; Zhang, D.; Zhang, L.; Sun, K. Ti@ δ -MnO₂ Core-Shell Nanowire Arrays as Self-Supported Electrodes of Supercapacitors and Li Ion Batteries. *Electrochim. Acta* **2016**, *202*, 8–13.
- (182) Shan, Z.; Clayton, D.; Pan, S.; Archana, P. S.; Gupta, A. Visible Light Driven Photoelectrochemical Properties of Ti@TiO₂ Nanowire Electrodes Sensitized with Core-Shell Ag@Ag₂S Nanoparticles. *J. Phys. Chem. B* **2014**, *118* (49), 14037–14046.
- (183) Xu, C.; Geng, H.; Bennett, R.; Clayton, D. A.; Pan, S. Ti@TiO₂ Nanowire Electrode with

- Polydisperse Gold Nanoparticles for Electrogenerated Chemiluminescence and Surface Enhanced Raman Spectroelectrochemistry. *J. Phys. Chem. C* **2013**, *117* (4), 1849–1856.
- (184) Guo, C.; Huo, H.; Han, X.; Xu, C.; Li, H. Ni/CdS Bifunctional Ti@TiO₂ Core–Shell Nanowire Electrode for High-Performance Nonenzymatic Glucose Sensing. *Anal. Chem.* **2014**, *86* (1), 876–883.
- (185) Ramadoss, A.; Kim, S. J. Vertically Aligned TiO₂ Nanorod Arrays for Electrochemical Supercapacitor. *J. Alloys Compd.* **2013**, *561*, 262–267.
- (186) Salari, M.; Konstantinov, K.; Liu, H. K.; Mohandas, E.; Berec, V.; Dohčević-Mitrović, Z.; Popović, Z.; Sham, T. K.; Cheng, H. M. Enhancement of the Capacitance in TiO₂ Nanotubes through Controlled Introduction of Oxygen Vacancies. *J. Mater. Chem.* **2011**, *21* (13), 5128.
- (187) Fan, Z.; Yan, J.; Wei, T.; Zhi, L.; Ning, G.; Li, T.; Wei, F. Asymmetric Supercapacitors Based on Graphene/MnO₂ and Activated Carbon Nanofiber Electrodes with High Power and Energy Density. *Adv. Funct. Mater.* **2011**, *21* (12), 2366–2375.
- (188) Cheng, Y.; Lu, S.; Zhang, H.; Varanasi, C. V.; Liu, J. Synergistic Effects from Graphene and Carbon Nanotubes Enable Flexible and Robust Electrodes for High-Performance Supercapacitors. *Nano Lett.* **2012**, *12* (8), 4206–4211.
- (189) Fabregat-Santiago, F.; Garcia-Belmonte, G.; Bisquert, J.; Zaban, A.; Salvador, P. Decoupling of Transport, Charge Storage, and Interfacial Charge Transfer in the Nanocrystalline TiO₂/Electrolyte System by Impedance Methods. *J. Phys. Chem. B* **2002**, *106* (2), 334–339.
- (190) Zheng, Z.; Chen, J.; Yoshida, R.; Gao, X.; Tarr, K.; Ikuhara, Y. H.; Zhou, W. One-Step Synthesis of TiO₂ Nanorod Arrays on Ti Foil for Supercapacitor Application.

- Nanotechnology* **2014**, 25 (43), 435406.
- (191) Tang, Q.; Wang, W.; Wang, G. The Perfect Matching between the Low-Cost Fe₂O₃ Nanowire Anode and the NiO Nanoflake Cathode Significantly Enhances the Energy Density of Asymmetric Supercapacitors. *J. Mater. Chem. A* **2015**, 3 (12), 6662–6670.
- (192) Qu, Q.; Yang, S.; Feng, X. 2D Sandwich-like Sheets of Iron Oxide Grown on Graphene as High Energy Anode Material for Supercapacitors. *Adv. Mater.* **2011**, 23 (46), 5574–5580.
- (193) Yang, P.; Ding, Y.; Lin, Z.; Chen, Z.; Li, Y.; Qiang, P.; Ebrahimi, M.; Mai, W.; Wong, C. P.; Wang, Z. L. Low-Cost High-Performance Solid-State Asymmetric Supercapacitors Based on MnO₂ Nanowires and Fe₂O₃ Nanotubes. *Nano Lett.* **2014**, 14 (2), 731–736.
- (194) Xiao, X.; Ding, T.; Yuan, L.; Shen, Y.; Zhong, Q.; Zhang, X.; Cao, Y.; Hu, B.; Zhai, T.; Gong, L.; Chen, J.; Tong, Y.; Zhou, J.; Wang, Z. L. WO_{3-x}/MoO_{3-x} Core/Shell Nanowires on Carbon Fabric as an Anode for All-Solid-State Asymmetric Supercapacitors. *Adv. Energy Mater.* **2012**, 2 (11), 1328–1332.
- (195) Chang, J.; Jin, M.; Yao, F.; Kim, T. H.; Le, V. T.; Yue, H.; Gunes, F.; Li, B.; Ghosh, A.; Xie, S.; Lee, Y. H. Asymmetric Supercapacitors Based on Graphene/MnO₂ Nanospheres and Graphene/MoO₃ Nanosheets with High Energy Density. *Adv. Funct. Mater.* **2013**, 23 (40), 5074–5083.
- (196) Yuan, C.; Li, J.; Hou, L.; Zhang, X.; Shen, L.; Lou, X. W. D. Ultrathin Mesoporous NiCo₂O₄ Nanosheets Supported on Ni Foam as Advanced Electrodes for Supercapacitors. *Adv. Funct. Mater.* **2012**, 22 (21), 4592–4597.
- (197) Jiang, J.; Li, Y.; Liu, J.; Huang, X.; Yuan, C.; Lou, X. W. D. Recent Advances in Metal Oxide-Based Electrode Architecture Design for Electrochemical Energy Storage. *Adv. Mater.* **2012**, 24 (38), 5166–5180.

- (198) Yang, D.; Zhu, J.; Rui, X.; Tan, H.; Cai, R.; Hoster, H. E.; Yu, D. Y. W.; Hng, H. H.; Yan, Q. Synthesis of Cobalt Phosphides and Their Application as Anodes for Lithium Ion Batteries. *ACS Appl. Mater. Interfaces* **2013**, *5* (3), 1093–1099.
- (199) Tang, C.; Zhang, R.; Lu, W.; He, L.; Jiang, X.; Asiri, A. M.; Sun, X. Fe-Doped CoP Nanoarray: A Monolithic Multifunctional Catalyst for Highly Efficient Hydrogen Generation. *Adv. Mater.* **2016**, *29* (2), 1602441.
- (200) Tang, C.; Gan, L.; Zhang, R.; Lu, W.; Jiang, X.; Asiri, A. M.; Sun, X.; Wang, J.; Chen, L. Ternary $\text{Fe}_x\text{Co}_{1-x}\text{P}$ Nanowire Array as a Robust Hydrogen Evolution Reaction Electrocatalyst with Pt-like Activity: Experimental and Theoretical Insight. *Nano Lett.* **2016**, *16* (10), 6617–6621.
- (201) Pu, Z.; Liu, Q.; Jiang, P.; Asiri, A. M.; Obaid, A. Y.; Sun, X. CoP Nanosheet Arrays Supported on a Ti Plate: An Efficient Cathode for Electrochemical Hydrogen Evolution. *Chem. Mater.* **2014**, *26* (15), 4326–4329.
- (202) Liu, T.; Ma, X.; Liu, D.; Hao, S.; Du, G.; Ma, Y.; Asiri, A. M.; Sun, X.; Chen, L. Mn Doping of CoP Nanosheets Array: An Efficient Electrocatalyst for Hydrogen Evolution Reaction with Enhanced Activity at All pH Values. *ACS Catal.* **2017**, *7* (1), 98–102.
- (203) Tian, J.; Cheng, N.; Liu, Q.; Xing, W.; Sun, X. Cobalt Phosphide Nanowires: Efficient Nanostructures for Fluorescence Sensing of Biomolecules and Photocatalytic Evolution of Dihydrogen from Water under Visible Light. *Angew. Chemie Int. Ed.* **2015**, *54* (18), 5493–5497.
- (204) Wang, D.; Kong, L.-B.; Liu, M.-C.; Zhang, W.-B.; Luo, Y.-C.; Kang, L. Amorphous Ni–P Materials for High Performance Pseudocapacitors. *J. Power Sources* **2015**, *274*, 1107–1113.

- (205) Chen, X.; Cheng, M.; Chen, D.; Wang, R. Shape-Controlled Synthesis of Co₂P Nanostructures and Their Application in Supercapacitors. *ACS Appl. Mater. Interfaces* **2016**, *8* (6), 3892–3900.
- (206) Yu, Z.; Tetard, L.; Zhai, L.; Thomas, J. Supercapacitor Electrode Materials: Nanostructures from 0 to 3 Dimensions. *Energy Environ. Sci.* **2015**, *8* (3), 702–730.
- (207) Yu, M.; Qiu, W.; Wang, F.; Zhai, T.; Fang, P.; Lu, X.; Tong, Y. Three Dimensional Architectures: Design, Assembly and Application in Electrochemical Capacitors. *J. Mater. Chem. A* **2015**, *3* (31), 15792–15823.
- (208) Tian, J.; Liu, Q.; Asiri, A. M.; Sun, X. Self-Supported Nanoporous Cobalt Phosphide Nanowire Arrays: An Efficient 3D Hydrogen-Evolving Cathode over the Wide Range of pH 0–14. *J. Am. Chem. Soc.* **2014**, *136* (21), 7587–7590.
- (209) Jiang, J.; Liu, J. P.; Huang, X. T.; Li, Y. Y.; Ding, R. M.; Ji, X. X.; Hu, Y. Y.; Chi, Q. B.; Zhu, Z. H. General Synthesis of Large-Scale Arrays of One-Dimensional Nanostructured Co₃O₄ Directly on Heterogeneous Substrates. *Cryst. Growth Des.* **2010**, *10* (1), 70–75.
- (210) Pramanik, M.; Tominaka, S.; Wang, Z.-L.; Takei, T.; Yamauchi, Y. Mesoporous Semimetallic Conductors: Structural and Electronic Properties of Cobalt Phosphide Systems. *Angew. Chemie Int. Ed.* **2017**.
- (211) Liu, W.; Xu, L.; Jiang, D.; Qian, J.; Liu, Q.; Yang, X.; Wang, K. Reactable Ionic Liquid Assisted Preparation of Porous Co₃O₄ Nanostructures with Enhanced Supercapacitive Performance. *CrystEngComm* **2014**, *16* (12), 2395.
- (212) Rui, X.; Tan, H.; Sim, D.; Liu, W.; Xu, C.; Hng, H. H.; Yazami, R.; Lim, T. M.; Yan, Q. Template-Free Synthesis of Urchin-like Co₃O₄ Hollow Spheres with Good Lithium Storage Properties. *J. Power Sources* **2013**, *222*, 97–102.

- (213) Li, L.; Seng, K. H.; Chen, Z.; Guo, Z.; Liu, H. K. Self-Assembly of Hierarchical Star-like Co₃O₄ Micro/nanostructures and Their Application in Lithium Ion Batteries. *Nanoscale* **2013**, *5* (5), 1922–1928.
- (214) Hagelin-Weaver, H. A. E.; Hoflund, G. B.; Minahan, D. M.; Salaita, G. N. Electron Energy Loss Spectroscopic Investigation of Co Metal, CoO, and Co₃O₄ before and after Ar⁺ Bombardment. *Appl. Surf. Sci.* **2004**, *235* (4), 420–448.
- (215) Wang, P.; Song, F.; Amal, R.; Ng, Y. H.; Hu, X. Efficient Water Splitting Catalyzed by Cobalt Phosphide-Based Nanoneedle Arrays Supported on Carbon Cloth. *ChemSusChem* **2016**, *9* (5), 472–477.
- (216) Grosvenor, A. P.; Wik, S. D.; Cavell, R. G.; Mar, A. Examination of the Bonding in Binary Transition-Metal Monophosphides MP (M = Cr, Mn, Fe, Co) by X-Ray Photoelectron Spectroscopy. *Inorg. Chem.* **2005**, *44* (24), 8988–8998.
- (217) Gogotsi, Y.; Simon, P. True Performance Metrics in Electrochemical Energy Storage. *Science* **2011**, *334* (6058), 917–918.
- (218) Qu, Q.; Zhang, P.; Wang, B.; Chen, Y.; Tian, S.; Wu, Y.; Holze, R. Electrochemical Performance of MnO₂ Nanorods in Neutral Aqueous Electrolytes as a Cathode for Asymmetric Supercapacitors. *J. Phys. Chem. C* **2009**, *113* (31), 14020–14027.
- (219) Yu, N.; Zhu, M.-Q.; Chen, D. Flexible All-Solid-State Asymmetric Supercapacitors with Three-Dimensional CoSe₂/carbon Cloth Electrodes. *J. Mater. Chem. A* **2015**, *3* (15), 7910–7918.
- (220) Feng, J.-X.; Ye, S.-H.; Lu, X.-F.; Tong, Y.-X.; Li, G.-R. Asymmetric Paper Supercapacitor Based on Amorphous Porous Mn₃O₄ Negative Electrode and Ni(OH)₂ Positive Electrode: A Novel and High-Performance Flexible Electrochemical Energy

- Storage Device. *ACS Appl. Mater. Interfaces* **2015**, 7 (21), 11444–11451.
- (221) Chang, J.; Xiao, Y.; Xiao, M.; Ge, J.; Liu, C.; Xing, W. Surface Oxidized Cobalt-Phosphide Nanorods As an Advanced Oxygen Evolution Catalyst in Alkaline Solution. *ACS Catal.* **2015**, 5 (11), 6874–6878.
- (222) Saadi, F. H.; Carim, A. I.; Verlage, E.; Hemminger, J. C.; Lewis, N. S.; Soriaga, M. P. CoP as an Acid-Stable Active Electrocatalyst for the Hydrogen-Evolution Reaction: Electrochemical Synthesis, Interfacial Characterization and Performance Evaluation. *J. Phys. Chem. C* **2014**, 118 (50), 29294–29300.
- (223) Goubert-Renaudin, S. N. S.; Zhu, X. Carbon-Supported Cobalt Oxide Nanoparticles Cobalt Porphyrin for Oxygen Reduction in Acids: Insights on Reactivity. *J. Electrochem. Soc.* **2012**, 159 (4), B426.
- (224) Patil, U. M.; Nam, M. S.; Sohn, J. S.; Kulkarni, S. B.; Shin, R.; Kang, S.; Lee, S.; Kim, J. H.; Jun, S. C. Controlled Electrochemical Growth of Co(OH)₂ Flakes on 3D Multilayered Graphene Foam for High Performance Supercapacitors. *J. Mater. Chem. A* **2014**, 2 (44), 19075–19083.
- (225) Lu, X.; Liu, T.; Zhai, T.; Wang, G.; Yu, M.; Xie, S.; Ling, Y.; Liang, C.; Tong, Y.; Li, Y. Improving the Cycling Stability of Metal-Nitride Supercapacitor Electrodes with a Thin Carbon Shell. *Adv. Energy Mater.* **2014**, 4 (4), 1300994.
- (226) Lu, X.; Yu, M.; Zhai, T.; Wang, G.; Xie, S.; Liu, T.; Liang, C.; Tong, Y.; Li, Y. High Energy Density Asymmetric Quasi-Solid-State Supercapacitor Based on Porous Vanadium Nitride Nanowire Anode. *Nano Lett.* **2013**, 13 (6), 2628–2633.
- (227) Lu, X.; Wang, G.; Zhai, T.; Yu, M.; Xie, S.; Ling, Y.; Liang, C.; Tong, Y.; Li, Y. Stabilized TiN Nanowire Arrays for High-Performance and Flexible Supercapacitors.

- Nano Lett.* **2012**, *12* (10), 5376–5381.
- (228) Wang, G.; Lu, X.; Ling, Y.; Zhai, T.; Wang, H.; Tong, Y.; Li, Y. LiCl/PVA Gel Electrolyte Stabilizes Vanadium Oxide Nanowire Electrodes for Pseudocapacitors. *ACS Nano* **2012**, *6* (11), 10296–10302.
- (229) Holdren, J. P. Energy and Sustainability. *Science* **2007**, *315* (5813), 737–737.
- (230) Luo, J.; Zhu, H. T.; Fan, H. M.; Liang, J. K.; Shi, H. L.; Rao, G. H.; Li, J. B.; Du, Z. M.; Shen, Z. X. Synthesis of Single-Crystal Tetragonal α -MnO₂ Nanotubes. *J. Phys. Chem. C* **2008**, *112* (33), 12594–12598.
- (231) Zilong, W.; Zhu, Z.; Qiu, J.; Yang, S. High Performance Flexible Solid-State Asymmetric Supercapacitors from MnO₂/ZnO Core-Shell Nanorods//specially Reduced Graphene Oxide. *J. Mater. Chem. C* **2014**, *2* (7), 1331–1336.
- (232) Lu, X.; Yu, M.; Wang, G.; Zhai, T.; Xie, S.; Ling, Y.; Tong, Y.; Li, Y. H-TiO₂@MnO₂//H-TiO₂@C Core-Shell Nanowires for High Performance and Flexible Asymmetric Supercapacitors. *Adv. Mater.* **2013**, *25* (2), 267–272.
- (233) Zhang, Y. Q. Q.; Li, L.; Shi, S. J. J.; Xiong, Q. Q. Q.; Zhao, X. Y. Y.; Wang, X. L. L.; Gu, C. D. D.; Tu, J. P. P. Synthesis of Porous Co₃O₄ Nanoflake Array and Its Temperature Behavior as Pseudo-Capacitor Electrode. *J. Power Sources* **2014**, *256*, 200–205.
- (234) Tsai, J.-C.; Hon, M.-H.; Leu, I.-C. Preparation of CoS₂ Nanoflake Arrays through Ion Exchange Reaction of Co(OH)₂ and Their Application as Counter Electrodes for Dye-Sensitized Solar Cells. *RSC Adv.* **2015**, *5* (6), 4328–4333.
- (235) Wang, L.; Yang, H.; Liu, X.; Zeng, R.; Li, M.; Huang, Y.; Hu, X. Constructing Hierarchical Tectorum-like α -Fe₂O₃/PPy Nanoarrays on Carbon Cloth for Solid-State Asymmetric Supercapacitors. *Angew. Chemie Int. Ed.* **2016**, *56* (4), 1105–1110.

- (236) Fan, H.; Niu, R.; Duan, J.; Liu, W.; Shen, W. Fe₃O₄@Carbon Nanosheets for All-Solid-State Supercapacitor Electrodes. *ACS Appl. Mater. Interfaces* **2016**, *8* (30), 19475–19483.
- (237) Liu, J.; Zheng, M.; Shi, X.; Zeng, H.; Xia, H. Amorphous FeOOH Quantum Dots Assembled Mesoporous Film Anchored on Graphene Nanosheets with Superior Electrochemical Performance for Supercapacitors. *Adv. Funct. Mater.* **2016**, *26* (6), 919–930.
- (238) Nithya, V. D.; Sabari Arul, N. Progress and Development of Fe₃O₄ Electrodes for Supercapacitors. *J. Mater. Chem. A* **2016**, *4* (28), 10767–10778.
- (239) Zhang, W.-B.; Ma, X.-J.; Loh, A.; Li, X.; Walsh, F. C.; Kong, L.-B. High Volumetric Energy Density Capacitors Based on New Electrode Material Lanthanum Nitride. *ACS Energy Lett.* **2017**, *2* (2), 336–341.
- (240) Pradhan, B.; Kumar, G. S.; Dalui, A.; Khan, A. H.; Satpati, B.; Ji, Q.; Shrestha, L. K.; Ariga, K.; Acharya, S.; Ariga, K.; Fontecave, M.; Artero, V. Shape-Controlled Cobalt Phosphide Nanoparticles as Volatile Organic Solvent Sensor. *J. Mater. Chem. C* **2016**, *4* (22), 4967–4977.
- (241) Han, J.; Dou, Y.; Zhao, J.; Wei, M.; Evans, D. G.; Duan, X. Flexible CoAl LDH@PEDOT Core/Shell Nanoplatelet Array for High-Performance Energy Storage. *Small* **2013**, *9* (1), 98–106.
- (242) Liang, Y.; Liu, Q.; Asiri, A. M.; Sun, X.; Luo, Y. Self-Supported FeP Nanorod Arrays: A Cost-Effective 3D Hydrogen Evolution Cathode with High Catalytic Activity. *ACS Catal.* **2014**, *4* (11), 4065–4069.
- (243) Jiang, P.; Liu, Q.; Liang, Y.; Tian, J.; Asiri, A. M.; Sun, X. A Cost-Effective 3D

- Hydrogen Evolution Cathode with High Catalytic Activity: FeP Nanowire Array as the Active Phase. *Angew. Chemie Int. Ed.* **2014**, *53* (47), 12855–12859.
- (244) Kou, J.; Varma, R. S. Expeditious Organic-Free Assembly: Morphologically Controlled Synthesis of Iron Oxides Using Microwaves. *Nanoscale* **2013**, *5* (18), 8675.
- (245) Fan, X.; Luo, C.; Lamb, J.; Zhu, Y.; Xu, K.; Wang, C. PEDOT Encapsulated FeOF Nanorod Cathodes for High Energy Lithium-Ion Batteries. *Nano Lett.* **2015**, *15* (11), 7650–7656.
- (246) Yan, M.; Zhang, Y.; Li, Y.; Huo, Y.; Yu, Y.; Wang, C.; Jin, J.; Chen, L.; Hasan, T.; Wang, B.; Su, B.-L. Manganese Dioxide Nanosheet Functionalized sulfur@PEDOT Core-shell Nanospheres for Advanced Lithium-sulfur Batteries. *J. Mater. Chem. A* **2016**, *4* (24), 9403–9412.
- (247) Wang, G.; Wang, H.; Lu, X.; Ling, Y.; Yu, M.; Zhai, T.; Tong, Y.; Li, Y. Solid-State Supercapacitor Based on Activated Carbon Cloths Exhibits Excellent Rate Capability. *Adv. Mater.* **2014**, *26* (17), 2676–2682.
- (248) Han, F.; Zhang, C.; Yang, J.; Ma, G.; He, K.; Li, X. Well-Dispersed and Porous FeP@C Nanoplates with Stable and Ultrafast Lithium Storage Performance through Conversion Reaction Mechanism. *J. Mater. Chem. A* **2016**, *4* (33), 12781–12789.
- (249) Jiang, J.; Wang, C.; Liang, J.; Zuo, J.; Yang, Q. Synthesis of Nanorod-FeP@C Composites with Hysteretic Lithiation in Lithium-Ion Batteries. *Dalt. Trans.* **2015**, *44* (22), 10297–10303.
- (250) Garreau, S.; Louarn, G.; Buisson, J. P.; Froyer, G.; Lefrant, S. In Situ Spectroelectrochemical Raman Studies of Poly(3,4-Ethylenedioxythiophene) (PEDT). *Macromolecules* **1999**, *32* (20), 6807–6812.

- (251) Österholm, A.; Lindfors, T.; Kauppila, J.; Damlin, P.; Kvarnström, C. Electrochemical Incorporation of Graphene Oxide into Conducting Polymer Films. *Electrochim. Acta* **2012**, *83*, 463–470.
- (252) Lindfors, T.; Boeva, Z. A.; Latonen, R.-M.; Beljonne, D.; Lazzaroni, R.; Bredas, J. L.; Dekany, I.; Jeong, H. K.; Kim, J. M.; Choi, J. Y.; Lee, Y. H. Electrochemical Synthesis of poly(3,4-Ethylenedioxythiophene) in Aqueous Dispersion of High Porosity Reduced Graphene Oxide. *RSC Adv.* **2014**, *4* (48), 25279–25286.
- (253) Zubair, N. A.; Rahman, N. A.; Lim, H. N.; Zawawi, R. M.; Sulaiman, Y.; Li, J.; Dhesi, S. S.; Marchetto, H. Electrochemical Properties of PVA–GO/PEDOT Nanofibers Prepared Using Electrospinning and Electropolymerization Techniques. *RSC Adv.* **2016**, *6* (21), 17720–17727.
- (254) Bazzaoui, E. A.; Aeiyaeh, S.; Lacaze, P. C. Electropolymerization of Bithiophene on Pt and Fe Electrodes in an Aqueous Sodium Dodecylsulfate (SDS) Micellar Medium. *Synth. Met.* **1996**, *83* (2), 159–165.
- (255) Liu, T.; Ling, Y.; Yang, Y.; Finn, L.; Collazo, E.; Zhai, T.; Tong, Y.; Li, Y. Investigation of Hematite Nanorod–nanoflake Morphological Transformation and the Application of Ultrathin Nanoflakes for Electrochemical Devices. *Nano Energy* **2015**, *12*, 169–177.
- (256) Sun, J.; Huang, Y.; Fu, C.; Huang, Y.; Zhu, M.; Tao, X.; Zhi, C.; Hu, H. A High Performance Fiber-Shaped PEDOT@MnO₂/C@Fe₃O₄ Asymmetric Supercapacitor for Wearable Electronics. *J. Mater. Chem. A* **2016**, *4* (38), 14877–14883.
- (257) Cheng, Z.; Tan, G.; Qiu, Y.; Guo, B.; Cheng, F.; Fan, H. High Performance Electrochemical Capacitors Based on MnO₂/activated-Carbon-Paper. *J. Mater. Chem. C* **2015**, *3* (24), 6166–6171.

- (258) Zhu, C.; Yang, P.; Chao, D.; Wang, X.; Zhang, X.; Chen, S.; Tay, B. K.; Huang, H.; Zhang, H.; Mai, W.; Fan, H. J. All Metal Nitrides Solid-State Asymmetric Supercapacitors. *Adv. Mater.* **2015**, 27 (31), 4566–4571.
- (259) Xu, J.; Wang, Q.; Wang, X.; Xiang, Q.; Liang, B.; Chen, D.; Shen, G. Flexible Asymmetric Supercapacitors Based upon Co₉S₈ nanorod//Co₃O₄@RuO₂ Nanosheet Arrays on Carbon Cloth. *ACS Nano* **2013**, 7 (6), 5453–5462.

Appendix: Copyright Permissions

CAMBRIDGE UNIVERSITY PRESS LICENSE TERMS AND CONDITIONS

Oct 03, 2017

This Agreement between Zhi Zheng ("You") and Cambridge University Press ("Cambridge University Press") consists of your license details and the terms and conditions provided by Cambridge University Press and Copyright Clearance Center.

License Number	4104261120197
License date	May 08, 2017
Licensed Content Publisher	Cambridge University Press
Licensed Content Publication	MRS Bulletin
Licensed Content Title	Electrochemical energy storage to power the 21st century
Licensed Content Author	Debra R. Rolison, Linda F. Nazar
Licensed Content Date	Apr 29, 2010
Licensed Content Volume	36
Licensed Content Issue	7
Start page	486
End page	493
Type of Use	Dissertation/Thesis
Requestor type	Author
Portion	Full article
Author of this Cambridge University Press article	No
Author / editor of the new work	Yes
Order reference number	
Territory for reuse	North America Only
Title of your thesis / dissertation	Three-dimensional Nano Material for Supercapacitor Application: From Metal Oxide to Metal Phosphide
Expected completion date	Aug 2017
Estimated size(pages)	100
Requestor Location	Zhi Zheng 2000 Lakeshore Dr NEW ORLEANS, LA 70148 United States Attn: Zhi Zheng
Publisher Tax ID	GB823847609
Billing Type	Invoice
Billing Address	Zhi Zheng 2000 Lakeshore Dr NEW ORLEANS, LA 70148

GRANT FOR DISSERTATION USE - RE: Request for Permission to Reprint

Elizabeth Sandler <esandler@aaas.org>

Wed 6/28/2017 8:36 AM

To: Zhi Zheng <zzheng1@my.uno.edu>;

Dear Zhi Zheng:

Thank you very much for your request and for your interest in our content.

Please feel free to include the figure/s in your thesis or dissertation subject to the guidelines listed on our website. I've copied them below:

<http://www.sciencemag.org/help/reprints-and-permissions>

Under: Using AAAS material in a thesis or dissertation

Reproducing AAAS Material in your Thesis or Dissertation

AAAS permits the use of content published in its journals *Science*, *Science Translational Medicine*, and *Science Signaling*, but only provided the following criteria are met.

- . If you are using figure(s)/table(s), permission is granted for use in print and electronic versions of your dissertation or thesis.
- . A full text article may be used only in print versions of a dissertation or thesis. AAAS does not permit the reproduction of full text articles in electronic versions of theses or dissertations.
- . The following credit line must be printed along with the AAAS material: "From [Full Reference Citation]. Reprinted with permission from AAAS."
- . All required credit lines and notices must be visible any time a user accesses any part of the AAAS material and must appear on any printed copies that an authorized user might make.
- . The AAAS material may not be modified or altered except that figures and tables may be modified with permission from the author. Author permission for any such changes must be secured prior to your use.
- . AAAS must publish the full paper prior to your use of any of its text or figures.
- . If the AAAS material covered by this permission was published in *Science* during the years 1974–1994, you must also obtain permission from the author, who may grant or withhold permission, and who may or may not charge a fee if permission is granted. See original article for author's address. This condition does not apply to news articles.

Permission covers the distribution of your dissertation or thesis on demand by a third party distributor (e.g. ProQuest / UMI), provided the AAAS material covered by this permission remains in situ and is not distributed by that third party outside of the context of your Thesis/Dissertation.

Permission does not apply to figures/photos/artwork or any other content or materials included in your work that are credited to non-AAAS sources.

If the requested material is sourced to or references non-AAAS sources, you must obtain authorization from that source as well before using that material. **PLEASE NOTE:** The figure was adapted from KRISTY JOST/DREXEL. You will need her permission as well and will also need to provide her credit as well as cite the Science paper. I located her contact information here:

<http://drexel.edu/materials/about/profiles/kristy-jost/>

ROYAL SOCIETY OF CHEMISTRY LICENSE TERMS AND CONDITIONS

Oct 03, 2017

This Agreement between Zhi Zheng ("You") and Royal Society of Chemistry ("Royal Society of Chemistry") consists of your license details and the terms and conditions provided by Royal Society of Chemistry and Copyright Clearance Center.

License Number	4201580918650
License date	Oct 03, 2017
Licensed Content Publisher	Royal Society of Chemistry
Licensed Content Publication	Chemical Society Reviews
Licensed Content Title	Carbon-based materials as supercapacitor electrodes
Licensed Content Author	Li Li Zhang,X. S. Zhao
Licensed Content Date	Jun 12, 2009
Licensed Content Volume	38
Licensed Content Issue	9
Type of Use	Thesis/Dissertation
Requestor type	academic/educational
Portion	figures/tables/images
Number of figures/tables/images	3
Format	print and electronic
Distribution quantity	1
Will you be translating?	no
Order reference number	
Title of the thesis/dissertation	Three-dimensional Nano Material for Supercapacitor Application: From Metal Oxide to Metal Phosphide
Expected completion date	Aug 2017
Estimated size	100
Requestor Location	Zhi Zheng 2000 Lakeshore Dr NEW ORLEANS, LA 70148 United States Attn: Zhi Zheng
Billing Type	Invoice
Billing Address	Zhi Zheng 2000 Lakeshore Dr NEW ORLEANS, LA 70148 United States Attn: Zhi Zheng
Total	0.00 USD

Terms and Conditions

This License Agreement is between {Requestor Name} ("You") and The Royal Society of Chemistry ("RSC") provided by the Copyright Clearance Center ("CCC"). The license consists of your order details, the terms and conditions provided by the Royal Society of Chemistry, and the payment terms and conditions.
RSC / TERMS AND CONDITIONS

**JOHN WILEY AND SONS LICENSE
TERMS AND CONDITIONS**

Oct 03, 2017

This Agreement between Zhi Zheng ("You") and John Wiley and Sons ("John Wiley and Sons") consists of your license details and the terms and conditions provided by John Wiley and Sons and Copyright Clearance Center.

License Number	4201581164945
License date	Oct 03, 2017
Licensed Content Publisher	John Wiley and Sons
Licensed Content Publication	Chemistry - A European Journal
Licensed Content Title	A Universal Model for Nanoporous Carbon Supercapacitors Applicable to Diverse Pore Regimes, Carbon Materials, and Electrolytes
Licensed Content Author	Jingsong Huang,Bobby G. Sumpter,Vincent Meunier
Licensed Content Date	Jun 24, 2008
Licensed Content Pages	13
Type of use	Dissertation/Thesis
Requestor type	University/Academic
Format	Print and electronic
Portion	Figure/table
Number of figures/tables	3
Original Wiley figure/table number(s)	Figure 1,2,3
Will you be translating?	No
Title of your thesis / dissertation	Three-dimensional Nano Material for Supercapacitor Application: From Metal Oxide to Metal Phosphide
Expected completion date	Aug 2017
Expected size (number of pages)	100
Requestor Location	Zhi Zheng 2000 Lakeshore Dr NEW ORLEANS, LA 70148 United States Attn: Zhi Zheng
Publisher Tax ID	EU826007151
Billing Type	Invoice
Billing Address	Zhi Zheng 2000 Lakeshore Dr NEW ORLEANS, LA 70148 United States Attn: Zhi Zheng
Total	0.00 USD

ROYAL SOCIETY OF CHEMISTRY LICENSE TERMS AND CONDITIONS

Oct 03, 2017

This Agreement between Zhi Zheng ("You") and Royal Society of Chemistry ("Royal Society of Chemistry") consists of your license details and the terms and conditions provided by Royal Society of Chemistry and Copyright Clearance Center.

License Number	4151551035569
License date	Jul 17, 2017
Licensed Content Publisher	Royal Society of Chemistry
Licensed Content Publication	Faraday Discussions
Licensed Content Title	Ion counting in supercapacitor electrodes using NMR spectroscopy
Licensed Content Author	John M. Griffin,Alexander C. Forse,Hao Wang,Nicole M. Trease,Pierre-Louis Taberna,Patrice Simon,Clare P. Grey
Licensed Content Date	Aug 5, 2014
Licensed Content Volume	176
Licensed Content Issue	0
Type of Use	Thesis/Dissertation
Requestor type	academic/educational
Portion	figures/tables/images
Number of figures/tables/images	3
Format	print and electronic
Distribution quantity	1
Will you be translating?	no
Order reference number	
Title of the thesis/dissertation	Three-dimensional Nano Material for Supercapacitor Application: From Metal Oxide to Metal Phosphide
Expected completion date	Aug 2017
Estimated size	100
Requestor Location	Zhi Zheng 2000 Lakeshore Dr NEW ORLEANS, LA 70148 United States Attn: Zhi Zheng
Billing Type	Invoice
Billing Address	Zhi Zheng 2000 Lakeshore Dr NEW ORLEANS, LA 70148 United States Attn: Zhi Zheng
Total	0.00 USD
Terms and Conditions	

This License Agreement is between {Requestor Name} ("You") and The Royal Society of Chemistry ("RSC") provided by the Copyright Clearance Center ("CCC"). The license consists of your order details, the terms and conditions provided by the Royal Society of Chemistry, and the payment terms and conditions.

**ROYAL SOCIETY OF CHEMISTRY LICENSE
TERMS AND CONDITIONS**

Oct 03, 2017

This Agreement between Zhi Zheng ("You") and Royal Society of Chemistry ("Royal Society of Chemistry") consists of your license details and the terms and conditions provided by Royal Society of Chemistry and Copyright Clearance Center.

License Number	4201581362378
License date	Oct 03, 2017
Licensed Content Publisher	Royal Society of Chemistry
Licensed Content Publication	Energy & Environmental Science
Licensed Content Title	Pseudocapacitive oxide materials for high-rate electrochemical energy storage
Licensed Content Author	Veronica Augustyn,Patrice Simon,Bruce Dunn
Licensed Content Date	Mar 13, 2014
Licensed Content Volume	7
Licensed Content Issue	5
Type of Use	Thesis/Dissertation
Requestor type	academic/educational
Portion	figures/tables/images
Number of figures/tables/images	3
Format	print and electronic
Distribution quantity	1
Will you be translating?	no
Order reference number	
Title of the thesis/dissertation	Three-dimensional Nano Material for Supercapacitor Application: From Metal Oxide to Metal Phosphide
Expected completion date	Aug 2017
Estimated size	100
Requestor Location	Zhi Zheng 2000 Lakeshore Dr NEW ORLEANS, LA 70148 United States Attn: Zhi Zheng
Billing Type	Invoice
Billing Address	Zhi Zheng 2000 Lakeshore Dr NEW ORLEANS, LA 70148 United States Attn: Zhi Zheng
Total	0.00 USD

NATURE PUBLISHING GROUP LICENSE TERMS AND CONDITIONS

Oct 03, 2017

This Agreement between Zhi Zheng ("You") and Nature Publishing Group ("Nature Publishing Group") consists of your license details and the terms and conditions provided by Nature Publishing Group and Copyright Clearance Center.

License Number	4152100424580
License date	Jul 18, 2017
Licensed Content Publisher	Nature Publishing Group
Licensed Content Publication	Nature Materials
Licensed Content Title	Materials for electrochemical capacitors
Licensed Content Author	Patrice SimonandYury Gogotsi
Licensed Content Date	Nov 1, 2008
Licensed Content Volume	7
Licensed Content Issue	11
Type of Use	reuse in a dissertation / thesis
Requestor type	academic/educational
Format	print and electronic
Portion	figures/tables/illustrations
Number of figures/tables/illustrations	3
High-res required	no
Figures	Figures 1,3,7
Author of this NPG article	no
Your reference number	
Title of your thesis / dissertation	Three-dimensional Nano Material for Supercapacitor Application: From Metal Oxide to Metal Phosphide
Expected completion date	Aug 2017
Estimated size (number of pages)	100
Requestor Location	Zhi Zheng 2000 Lakeshore Dr NEW ORLEANS, LA 70148 United States Attn: Zhi Zheng
Billing Type	Invoice
Billing Address	Zhi Zheng 2000 Lakeshore Dr NEW ORLEANS, LA 70148 United States Attn: Zhi Zheng
Total	0.00 USD
Terms and Conditions	Terms and Conditions for Permissions

RE: Request for Permission to Reprint

AIPRights Permissions <Rights@aip.org>

Fri 7/7/2017 8:54 AM

To: Zhi Zheng <zzheng1@my.uno.edu>;

Dear Dr. Zheng:

Thank you for requesting permission to reproduce material from AIP publications.

Material to be reproduced:

Figure 5 from:

Batteries and electrochemical capacitors. Héctor D. Abruña, Yasuyuki Kiya, and Jay C. Henderson, *Physics Today* 61, 12, 43 (2008); doi: 10.1063/1.3047681

For use in the following manner:

Reproduced in your dissertation titled, "Three-dimensional Nano Material for Supercapacitor Application: From Metal Oxide to Metal Phosphide".

Permission is granted subject to these conditions:

1. AIP grants you non-exclusive world rights in all languages and media. This permission extends to all subsequent and future editions of the new work.
2. The following notice must appear with the material (please fill in the information indicated by capital letters):

"Reproduced from [FULL CITATION], with the permission of the American Institute of Physics."

When reusing a full article, the notice must be printed on the first page of the reprinted article or book chapter. When reusing figures, photographs, covers, or tables, the notice may appear in the caption, in a footnote, or in the reference list.

In cases where the new publication is licensed under a Creative Commons license, the full notice as stated above must appear with the reproduced material.

3. If the material is published in electronic format, we ask that a link be created pointing back to the abstract of the article on the journal website. This can be accomplished through the use of the article's DOI.

4. This permission does not apply to any materials credited to another source.

Please let us know if you have any questions.

Sincerely,

Susann Brailey

Manager, Rights & Permissions

AIP Publishing

[1305 Walt Whitman Road | Suite 300 | Melville NY 11747-4300 | USA](http://www.aip.org)

**ROYAL SOCIETY OF CHEMISTRY LICENSE
TERMS AND CONDITIONS**

Oct 03, 2017

This Agreement between Zhi Zheng ("You") and Royal Society of Chemistry ("Royal Society of Chemistry") consists of your license details and the terms and conditions provided by Royal Society of Chemistry and Copyright Clearance Center.

License Number	4201590574983
License date	Oct 03, 2017
Licensed Content Publisher	Royal Society of Chemistry
Licensed Content Publication	Journal of Materials Chemistry A
Licensed Content Title	Recent progresses in high-energy-density all pseudocapacitive-electrode-materials-based asymmetric supercapacitors
Licensed Content Author	Jinfeng Sun,Chen Wu,Xiaofei Sun,Hong Hu,Chunyi Zhi,Linrui Hou,Changzhou Yuan
Licensed Content Date	Mar 7, 2017
Licensed Content Volume	5
Licensed Content Issue	20
Type of Use	Thesis/Dissertation
Requestor type	academic/educational
Portion	figures/tables/images
Number of figures/tables/images	3
Format	print and electronic
Distribution quantity	1
Will you be translating?	no
Order reference number	
Title of the thesis/dissertation	Three-dimensional Nano Material for Supercapacitor Application: From Metal Oxide to Metal Phosphide
Expected completion date	Aug 2017
Estimated size	100
Requestor Location	Zhi Zheng 2000 Lakeshore Dr NEW ORLEANS, LA 70148 United States Attn: Zhi Zheng
Billing Type	Invoice
Billing Address	Zhi Zheng 2000 Lakeshore Dr NEW ORLEANS, LA 70148 United States Attn: Zhi Zheng



RightsLink®

Home

Account
Info

Help



Title: New Generation "Nanohybrid Supercapacitor"
Author: Katsuhiko Naoi, Wako Naoi, Shintaro Aoyagi, et al
Publication: Accounts of Chemical Research
Publisher: American Chemical Society
Date: May 1, 2013

Logged in as:
Zhi Zheng
Account #:
3001133881

LOGOUT

Copyright © 2013, American Chemical Society

PERMISSION/LICENSE IS GRANTED FOR YOUR ORDER AT NO CHARGE

This type of permission/license, instead of the standard Terms & Conditions, is sent to you because no fee is being charged for your order. Please note the following:

- Permission is granted for your request in both print and electronic formats, and translations.
- If figures and/or tables were requested, they may be adapted or used in part.
- Please print this page for your records and send a copy of it to your publisher/graduate school.
- Appropriate credit for the requested material should be given as follows: "Reprinted (adapted) with permission from (COMPLETE REFERENCE CITATION). Copyright (YEAR) American Chemical Society." Insert appropriate information in place of the capitalized words.
- One-time permission is granted only for the use specified in your request. No additional uses are granted (such as derivative works or other editions). For any other uses, please submit a new request.

If credit is given to another source for the material you requested, permission must be obtained from that source.

BACK

CLOSE WINDOW

Copyright © 2017 Copyright Clearance Center, Inc. All Rights Reserved. [Privacy statement](#). [Terms and Conditions](#).
Comments? We would like to hear from you. E-mail us at customer@copyright.com

**JOHN WILEY AND SONS LICENSE
TERMS AND CONDITIONS**

Oct 03, 2017

This Agreement between Zhi Zheng ("You") and John Wiley and Sons ("John Wiley and Sons") consists of your license details and the terms and conditions provided by John Wiley and Sons and Copyright Clearance Center.

License Number	4201590787240
License date	Oct 03, 2017
Licensed Content Publisher	John Wiley and Sons
Licensed Content Publication	Advanced Energy Materials
Licensed Content Title	The Electrochemical Flow Capacitor: A New Concept for Rapid Energy Storage and Recovery
Licensed Content Author	Volker Presser,Christopher R. Dennison,Jonathan Campos,Kevin W. Knehr,Emin C. Kumbur,Yury Gogotsi
Licensed Content Date	May 23, 2012
Licensed Content Pages	8
Type of use	Dissertation/Thesis
Requestor type	University/Academic
Format	Print and electronic
Portion	Figure/table
Number of figures/tables	3
Original Wiley figure/table number(s)	Figure 1, 2, 3
Will you be translating?	No
Title of your thesis / dissertation	Three-dimensional Nano Material for Supercapacitor Application: From Metal Oxide to Metal Phosphide
Expected completion date	Aug 2017
Expected size (number of pages)	100
Requestor Location	Zhi Zheng 2000 Lakeshore Dr NEW ORLEANS, LA 70148 United States Attn: Zhi Zheng
Publisher Tax ID	EU826007151
Billing Type	Invoice
Billing Address	Zhi Zheng 2000 Lakeshore Dr NEW ORLEANS, LA 70148 United States Attn: Zhi Zheng
Total	0.00 USD



RightsLink®

Home

Account
Info

Help



ACS Publications
Most Trusted. Most Cited. Most Read.

Title: Conducting Polymers for Pseudocapacitive Energy Storage
Author: Aimee M. Bryan, Luciano M. Santino, Yang Lu, et al
Publication: Chemistry of Materials
Publisher: American Chemical Society
Date: Sep 1, 2016
Copyright © 2016, American Chemical Society

Logged in as:

Zhi Zheng

Account #:
3001133881

LOGOUT

PERMISSION/LICENSE IS GRANTED FOR YOUR ORDER AT NO CHARGE

This type of permission/license, instead of the standard Terms & Conditions, is sent to you because no fee is being charged for your order. Please note the following:

- Permission is granted for your request in both print and electronic formats, and translations.
- If figures and/or tables were requested, they may be adapted or used in part.
- Please print this page for your records and send a copy of it to your publisher/graduate school.
- Appropriate credit for the requested material should be given as follows: "Reprinted (adapted) with permission from (COMPLETE REFERENCE CITATION). Copyright (YEAR) American Chemical Society." Insert appropriate information in place of the capitalized words.
- One-time permission is granted only for the use specified in your request. No additional uses are granted (such as derivative works or other editions). For any other uses, please submit a new request.

If credit is given to another source for the material you requested, permission must be obtained from that source.

BACK

CLOSE WINDOW

Copyright © 2017 [Copyright Clearance Center, Inc.](#) All Rights Reserved. [Privacy statement.](#) [Terms and Conditions.](#)
Comments? We would like to hear from you. E-mail us at customer@copyright.com



RightsLink®

Home

Account
Info

Help



Title:

Three-Dimensional Cobalt
Phosphide Nanowire Arrays as
Negative Electrode Material for
Flexible Solid-State Asymmetric
Supercapacitors

Logged in as:

Zhi Zheng

Account #:

3001133881

LOGOUT

Author:

Zhi Zheng, Michael Retana,
Xiaobing Hu, et al

Publication: Applied Materials

Publisher: American Chemical Society

Date: May 1, 2017

Copyright © 2017, American Chemical Society

PERMISSION/LICENSE IS GRANTED FOR YOUR ORDER AT NO CHARGE

This type of permission/license, instead of the standard Terms & Conditions, is sent to you because no fee is being charged for your order. Please note the following:

- Permission is granted for your request in both print and electronic formats, and translations.
- If figures and/or tables were requested, they may be adapted or used in part.
- Please print this page for your records and send a copy of it to your publisher/graduate school.
- Appropriate credit for the requested material should be given as follows: "Reprinted (adapted) with permission from (COMPLETE REFERENCE CITATION). Copyright (YEAR) American Chemical Society." Insert appropriate information in place of the capitalized words.
- One-time permission is granted only for the use specified in your request. No additional uses are granted (such as derivative works or other editions). For any other uses, please submit a new request.

BACK

CLOSE WINDOW

Copyright © 2017 [Copyright Clearance Center, Inc.](#) All Rights Reserved. [Privacy statement.](#) [Terms and Conditions.](#)
Comments? We would like to hear from you. E-mail us at customer care@copyright.com

VITA

Zhi Zheng was born in Fengjie, Chongqing, China. In 2004, he attended University of Electronic Science and Technology of China in Chengdu, China, where he received his Bachelor's and Master's degree in Applied Physics and Condensed Matter Physics in 2008 and 2011, respectively. He joined the Ph. D program of Engineering and Applied Sciences Program in Advanced Materials Research Institute, University of New Orleans, in 2011. During his Ph. D program, he worked on applications of nanostructured materials for gas sensors, piezotronics, and most importantly, supercapacitors.